

Multiscale Modeling of Fracture Processes in Cementitious Materials

Multiscale Modeling of Fracture Processes in Cementitious Materials

Proefschrift

ter verkrijging van de graad van doctor
aan de Technische Universiteit Delft,
op gezag van de Rector Magnificus prof.ir. K.C.A.M. Luyben,
voorzitter van het College voor Promoties,
in het openbaar te verdedigen
op dinsdag 25 september 2012 om 10.00 uur

door

Zhiwei QIAN
civiel ingenieur
geboren te Shangrao, Jiangxi Province, China

Dit proefschrift is goedgekeurd door de promotoren:

Prof.dr.ir. K. van Breugel

Prof.dr.ir. E. Schlangen

Samenstelling promotiecommissie:

Rector Magnificus	voorzitter
Prof.dr.ir. K. van Breugel	Technische Universiteit Delft, promotor
Prof.dr.ir. E. Schlangen	Technische Universiteit Delft, promotor
Prof. C. Miao	Southeast University, China
Prof.dr. A. Metrikine	Technische Universiteit Delft
Dr. G. Ye	Technische Universiteit Delft
Dr. E.J. Garboczi	Nat. Inst. of Standards and Technology, US
Dr. J. Sanchez Dolado	Tecnalia Research & Innovation, Spain
Prof.dr.ir. L.J. Sluys	Technische Universiteit Delft, reservelid

The work reported in this thesis is part of the research project CODICE (COmputationally Driven design of Innovative CEment-based materials, <http://www.codice-project.eu>) in the 7th Framework Program FP7, which is sponsored by the European Union, under the project grant agreement number 214030.

ISBN 978-94-6186-054-5 (Book)

ISBN 978-94-6186-055-2 (CD-Rom)

Keywords: Lattice fracture model, Anm material model, Parameter-passing up-scaling, Cement paste, Mortar, Concrete

© 2012 by Zhiwei Qian.

All rights reserved. This copy of the thesis has been supplied on condition that anyone who consults it is understood to recognize that its copyright rests with its author and that no quotation from the thesis and no information derived from it may be published without the author's prior consent.

The production of this PhD thesis conforms to the recommendations in the international standard ISO 7144:1986.

Typeset in L^AT_EX 2_ε.

Printed by Haveka B.V. in the Netherlands.

To my beloved mother and father

Summary

Concrete is a composite construction material, which is composed primarily of coarse aggregates, sands and cement paste. The fracture processes in concrete are complicated, because of the multiscale and multiphase nature of the material. In the past decades, comprehensive effort has been put to study the cracks evolution in concrete, both experimentally and numerically.

Among all the computational models dealing with concrete fracture, the lattice fracture model wins at several aspects, such as being able to capture detailed crack information, high computational efficiency and stability. The lattice fracture model also enables to investigate how the fracture properties of concrete depend on its material structure. This can be achieved by projecting the lattice network on top of the original material structure of concrete. In this thesis a parallel computing code is described, which is implemented for the lattice fracture model, in order to reduce the computational time and to enable the analysis on even larger lattice system.

The fracture properties of cement paste, mortar and concrete are highly related in nature. In this thesis the lattice fracture model is coupled with the parameter-passing multiscale modeling scheme to study the relationship of the fracture processes in cement paste, mortar and concrete. A multiscale fracture modeling procedure is proposed and demonstrated. Three levels are defined, including micrometer scale for cement paste, millimeter scale for mortar and centimeter scale for concrete. The lattice fracture model is applied at each scale respectively. The inputs required at a certain scale are obtained by

the simulation at a lower scale. At the lowest scale in question, the micrometer scale for cement paste, inputs are determined by laboratory experiments and/or nanoscale modeling from literature.

Besides the multiscale lattice fracture model, another highlight in this thesis is the development of the Anm material model, which can simulate a material structure of concrete with realistic shape aggregates. Compared with classic concrete material models, the shape of aggregates is changed from spheres to irregular ones, which is closer to reality. The aggregate particle shape is represented by spherical harmonic expansion, where a set of spherical harmonic coefficients is used to describe the irregular shape. The take-and-place parking method is employed to put multiple particles together within a pre-defined empty container, which can be interpreted as the material structure of concrete. The key element in this parking algorithm is to check whether two particles overlap, as no overlap is allowed in the resulting simulated material structure.

The multiscale lattice fracture model and the Anm material model, proposed and established in this thesis, can be used by researchers in concrete community, to study the various factors which influence the mechanical performance of cementitious materials. They can also be adapted with other computational models to form a complete fully multiscale modeling framework, from nanoscale to macroscale.

Samenvatting

Beton is een composiet constructiemateriaal dat is samengesteld uit grind, zand en cementsteen. Breukprocessen in beton zijn gecompliceerd omdat het materiaal van nature verschillende schalen en componenten bevat. In de laatste decennia was er veel aandacht voor het besturen van scheurgroei in beton, zowel op experimenteel vlak als ook numeriek.

Kijkend naar al de numerieke modellen voor scheurvorming in beton kan gesteld worden dat het lattice fracture model op enkele aspecten duidelijk als winnaar uit de bus komt. Deze zijn het vermogen om gedetailleerde scheurinformatie te produceren en de hoge numerieke efficiëntie en stabiliteit. Het lattice fracture model maakt het ook mogelijk om breukeigenschappen van beton te onderzoeken als functie van de materiaalstructuur. Hiervoor kan het lattice netwerk worden geprojecteerd bovenop de materiaalstructuur van beton. In dit proefschrift is een parallelle computer code beschreven, die is geïmplementeerd in het lattice fracture model, om de benodigde rekentijd te reduceren en het berekenen van grotere lattice systemen mogelijk te maken.

De breukeigenschappen van cementsteen, mortel en beton zijn sterk aan elkaar gerelateerd. In dit proefschrift is het lattice fracture model gekoppeld met het parameter-passing multi-schaal modelleer schema om de relatie te besturen tussen de breuk processen in cementsteen, mortel en beton. Een multi-schaal scheurmodelleer procedure is uitgewerkt en gedemonstreerd. Drie niveaus zijn gedefinieerd: de micrometerschaal voor cementsteen, de millimeterschaal voor mortel en de centimeterschaal voor beton. Het lattice fracture model is

toegepast op elke afzonderlijke schaal. De benodigde invoerparameters voor een bepaalde schaal volgen uit de simulatie van een lagere schaal. Bij de laagste schaal, de micrometerschaal voor cementsteen, zijn de invoerparameters bepaald op basis van laboratoriumexperimenten en/of nanoschaal modellering uit de literatuur.

Een ander belangrijk onderwerp in dit proefschrift, naast het ontwikkelen van het multi-schaal lattice fracture model, is de ontwikkeling van het Anm materiaal model. Dit model kan een materiaalstructuur van beton simuleren, waarbij de toeslagkorrels realistische vormen hebben. Vergeleken met klassieke materiaalmodellen voor beton kunnen in het Anm model naast bolvormige ook onregelmatige vormen worden gebruikt voor de toeslagkorrels, hetgeen realistischer is. De vorm van de toeslagkorrels wordt weergegeven met spherical harmonic expansion, waarbij een set van spherical harmonic coëfficiënten wordt gebruikt om de onregelmatige vorm te beschrijven. De take-and-place parkeer methode is toegepast om korrels in een gedefinieerde container te positioneren. Het resultaat levert vervolgens de materiaalstructuur van beton op. Het belangrijkste element in dit parkeer-algoritme is om te controleren of twee korrels elkaar niet overlappen. Overlappende korrels zijn niet toegestaan in de gesimuleerde materiaalstructuur.

Het multi-schaal lattice fracture model en het Anm materiaal model die beide zijn voorgesteld en uitgewerkt in dit proefschrift kunnen worden gebruikt door onderzoekers in de betonwereld. Met de modellen kunnen de verschillende factoren worden bestudeerd die het mechanisch gedrag van cementgebonden materialen beïnvloeden. Ze kunnen ook worden verweven met andere numerieke modellen om zo een compleet multi-schaal modelleer kader te vormen van nano- naar macroschaal.

Acknowledgements

The research work reported in this thesis was carried out primarily at the Delft University of Technology (TU Delft), the Netherlands and partly at the National Institute of Standards and Technology (NIST), United States. It is part of the research project CODICE (COmputationally Driven design of Innovative CEment-based materials, <http://www.codice-project.eu>) in the 7th Framework Program FP7, which is sponsored by the European Union. These organizations and CODICE project partners are appreciated for their academic, technical and financial support.

It would not have been possible to complete this PhD research work and to write this thesis without the help and support of the kind people around me, to only some of whom it is possible to give particular mention hereby.

I would like to express my gratitude to the promoters Prof.dr.ir. Klaas van Breugel and Prof.dr.ir. Erik Schlangen at TU Delft. Their kind guidance, valuable comments and fruitful discussions made my research work smooth. Dr. Guang Ye is appreciated for his unique thoughts about microstructure-based mechanical performance evaluation on cement paste, and for his suggestions on my career development.

I would like to thank Dr. Edward Garboczi at NIST, for his interesting ideas, kind supervision and collaboration to develop the innovative Anm material model, and his care when I worked at NIST as a guest researcher.

My gratitude also goes to all my current and former colleagues at TU Delft and NIST, as well as to all my friends. Among them, my

special thanks go to Jian Zhou for his advice on lattice fracture model applications, Qi Zhang for his help in using LaTeX to write this thesis, Quantao Liu for his suggestions on administrative aspects of thesis publishing and defense, Kar Tean Tan and Zhouhui Lian for their daily carpool ride to work when I stayed in Gaithersburg, MD, United States, and Yufei Yuan for the friendship and support of years.

Last but not least, I would like to thank my mother and father for their encouragement, unequivocal support and great patience at all times.

Zhiwei Qian

Delft, the Netherlands

May 2012

Contents

List of Figures	15
List of Tables	21
Symbols	23
1 Introduction	25
1.1 Background	25
1.2 State of the art	26
1.3 Objectives and methodology of this research	27
1.4 Outline of the thesis	27
2 Three-dimensional Lattice Fracture Model	31
2.1 Background	31
2.2 Modeling procedures	33
2.2.1 Lattice network construction	34
2.2.2 Test setup	44
2.2.3 Fracture processes simulation	48
2.2.4 Load-displacement response and cracks propagation	66
2.3 Summary	67
3 Cement Paste at Microscale	69
3.1 Micromechanical modeling of cement paste	70
3.1.1 Simulated microstructures of cement paste	71
3.1.2 Mechanical performance evaluation of the microstructures	74

CONTENTS

3.1.3	CT-scanned microstructures and its micromechanical properties	83
3.2	Influences of various factors	86
3.2.1	Degree of hydration	88
3.2.2	Cement fineness	93
3.2.3	Water/cement ratio	96
3.2.4	Mineral composition of cement	98
3.3	Summary	105
4	Mortar and Concrete at Mesoscale	109
4.1	Anm material model	110
4.1.1	Irregular shape description	111
4.1.2	Individual particle properties and operations	115
4.1.3	Parking procedures and algorithms	116
4.1.4	Periodic and non-periodic material boundaries	122
4.2	Material mesostructures for mortar and concrete	123
4.2.1	Mortar mesostructure	123
4.2.2	Concrete mesostructure	124
4.3	Summary	126
5	Multiscale Modeling	129
5.1	Parameter-passing scheme and size effect of cement paste	129
5.2	Bridging scales among cement paste, mortar and concrete	134
5.2.1	Connecting cement paste to mortar	135
5.2.2	Upscaling mortar to concrete	137
5.3	Summary	140
6	Conclusions and Outlook	143
6.1	Conclusions	143
6.2	Outlook	145
	References	147

List of Figures

1.1	Layout of the thesis main body	27
2.1	An overview of the lattice fracture analysis	34
2.2	Lattice network construction for general material and scale	35
2.3	Prism of the size 40 mm × 40 mm × 60 mm subject to uniaxial tensile load	36
2.4	Linear-brittle constitutive law of lattice elements	37
2.5	Microcracks pattern of perfect homogeneous material subject to uniaxial tension	40
2.6	Simulated global mechanical properties reduction against randomness	41
2.7	Lattice element type determination and its constitutive relation	42
2.8	Microstructure of cement paste simulated by the HYMOSTRUC3D model	43
2.9	3D contact particles, lattice element and network	43
2.10	Determination of particle modulus (first step averaging)	45
2.11	Determination of lattice element modulus (second step averaging)	46
2.12	Uniaxial tensile test setup	47
2.13	Flowchart of lattice fracture analysis kernel solver	49
2.14	3D lattice beam element in local domain	50
2.15	Local and global domains	63
2.16	Multi-linear constitutive law of lattice elements	66
3.1	Combined application of the HYMOSTRUC3D model and the 3D lattice fracture model	70

LIST OF FIGURES

3.2	Hydration of a single cement particle	72
3.3	Contact of hydrating cement particles	72
3.4	Microstructures of cement paste at different degrees of hydration with the specification in Table 3.1	73
3.5	Simulated degree of hydration diagram against hydration time . .	74
3.6	Voxel-based image of the microstructure of cement paste in Fig- ure 3.4(b) ($100\ \mu\text{m} \times 100\ \mu\text{m} \times 100\ \mu\text{m}$)	75
3.7	Individual phases of the microstructure of cement paste in Figure 3.6	76
3.8	Uniaxial tensile test on lattice system of cement paste at microscale	78
3.9	Simulated stress-strain diagram of cement paste at microscale . .	80
3.10	3D microcracks propagation of cement paste due to tension at mi- croscale, corresponding with Figure 3.9	80
3.11	Deformed specimen due to vertical tension in the final failure state, corresponding with Figure 3.9	81
3.12	Simulated stress-strain diagrams of cement paste at microscale, loaded horizontally along x -direction or y -direction, and vertically along z -direction	82
3.13	Cracks patterns in the final failure state, loaded horizontally along x -direction or y -direction, and vertically along z -direction	82
3.14	Simulated stress-strain diagrams of cement paste with regular lat- tice mesh, and irregular lattice mesh at the randomness of 0.5 . .	83
3.15	Pre-peak and post-peak microcracks for the regular meshed lattice system, and the irregular meshed lattice system at the randomness of 0.5	84
3.16	Microstructure of cement paste of size $75\ \mu\text{m} \times 75\ \mu\text{m} \times 75\ \mu\text{m}$ at the curing age 28 days with water/cement ratio 0.5 from CT scan (provided by UIUC)	85
3.17	Phase segmentation of the microstructure of cement paste in Fig- ure 3.16	86
3.18	Simulated stress-strain diagram of the experimental cement paste at microscale	87
3.19	Simulated cracks pattern in the final failure state for the experi- mental cement paste at microscale, corresponding with Figure 3.18	88

LIST OF FIGURES

3.20	Porosity of the hydrating cement paste system against degree of hydration	89
3.21	Development of the Young's modulus and the tensile strength against the degree of hydration	90
3.22	Trendlines of the Young's modulus and the tensile strength against the porosity of the cement paste system	91
3.23	Relationship between the strain at peak load and the degree of hydration	91
3.24	Relationship between the fracture energy and the degree of hydration	92
3.25	Relationship between the fracture energy and the porosity	93
3.26	Influences of degree of hydration on the tensile stress-strain response	94
3.27	Influences of degree of hydration on the cracks pattern in the final failure state, corresponding with Figure 3.26	94
3.28	Influences of cement fineness on the cracks pattern in the final failure state, compared at the same curing age of 28 days, corresponding with Table 3.12	95
3.29	Influences of cement fineness on the tensile stress-strain response, compared at the same degree of hydration 69%	96
3.30	Influences of cement fineness on the cracks pattern in the final failure state, compared at the same degree of hydration 69%, corresponding with Figure 3.29	97
3.31	Influences of water/cement ratio on the cracks pattern in the final failure state, compared at the same curing age of 28 days, corresponding with Table 3.13	98
3.32	Influences of water/cement ratio on the tensile stress-strain response, compared at the same degree of hydration 69%, corresponding with Table 3.14	99
3.33	Influences of water/cement ratio on the cracks pattern in the final failure state, compared at the same degree of hydration 69%, corresponding with Figure 3.32	100
3.34	Particle size distribution of the special cements	101
3.35	Initial microstructure of the special cement paste (porosity=56%)	101
3.36	Degree of hydration diagrams for the special cement pastes	103

LIST OF FIGURES

3.37	Microstructures of the special cement pastes at the curing age of 28 days	104
3.38	Stress-strain response diagrams for the special cement pastes at the curing age of 28 days	105
3.39	Cracks patterns in the final failure state for the special cement pastes at the curing age of 28 days, corresponding with Figure 3.38	106
4.1	Cement paste, mortar and concrete	109
4.2	Particles embedded matrix material model	110
4.3	Spheres, ellipsoids and multi-faceted polyhedrons [http://wikipedia.org]	111
4.4	Spherical coordinate system [http://wikipedia.org]	112
4.5	Spherical harmonic coefficients data structure	114
4.6	An irregular shape particle described by spherical harmonics	114
4.7	Flowchart of parking procedures	118
4.8	Two particles overlap	119
4.9	Newton-Raphson iteration scheme	121
4.10	Periodic and non-periodic material boundaries	123
4.11	Particle size distribution for the sands in mortar	125
4.12	The mesostructure of the mortar specimen with irregular shape sand particles	125
4.13	Particle size distribution for the coarse aggregates in concrete	126
4.14	The mesostructure of the concrete specimen with irregular shape crushed stones	127
5.1	Parameter-passing multiscale modeling scheme	130
5.2	Approximation of non-linear stress-strain response by multi-linear curve	131
5.3	Simulated stress-strain response for the 7 mm × 7 mm × 7 mm specimen of cement paste at mesoscale	132
5.4	Simulated stress crack opening diagram for the 7 mm × 7 mm × 7 mm specimen of cement paste at mesoscale	133
5.5	Affected lattice elements during the fracture processes in the cement paste specimen of the size 7 mm × 7 mm × 7 mm at mesoscale	134

LIST OF FIGURES

5.6	Lattice mesh for the 10 mm × 10 mm × 10 mm mortar at mesoscale	136
5.7	Simulated Young's modulus and tensile strength of every block in the 10 mm × 10 mm × 10 mm mortar at mesoscale	137
5.8	40 mm × 40 mm × 40 mm out of 150 mm × 150 mm × 150 mm concrete specimen	138
5.9	Lattice mesh for the 40 mm × 40 mm × 40 mm concrete at mesoscale	139
5.10	Simulated stress-strain response for the 40 mm × 40 mm × 40 mm concrete at mesoscale	140
5.11	Simulated stress crack opening diagram for the 40 mm × 40 mm × 40 mm concrete at mesoscale	141

LIST OF FIGURES

List of Tables

2.1	System size of the prism in Figure 2.3	37
2.2	Local mechanical properties of lattice elements in Figure 2.4 . . .	37
2.3	Simulation configurations with regard to lattice network construction	38
2.4	Influence of randomness on the simulated global Young's modulus E , tensile strength f_t and fracture energy G_F	39
2.5	Influence of boundary settings on the simulated global Young's modulus E , tensile strength f_t and fracture energy G_F	48
3.1	Specification of the cement mix used in the simulation	73
3.2	Assumed local mechanical properties of solid phases of cement paste	76
3.3	Classification of lattice element types	77
3.4	Local mechanical properties of lattice elements	77
3.5	Simulated mechanical properties of cement paste at microscale, corresponding with Figure 3.9	79
3.6	Simulated mechanical properties of cement paste at microscale, loaded horizontally along x -direction or y -direction, and vertically along z -direction	81
3.7	Simulated mechanical properties of cement paste with regular lat- tice mesh at the randomness of 0, and with irregular lattice mesh at the randomness of 0.5	84
3.8	Local mechanical properties of solid phases of experimental cement paste	86
3.9	Local mechanical properties of lattice elements for experimental cement paste	87

LIST OF TABLES

3.10	Simulated mechanical properties of the experimental cement paste at microscale, corresponding with Figure 3.18	87
3.11	Influences of degree of hydration on the tensile mechanical properties of cement paste at microscale	89
3.12	Influences of cement fineness, compared at the same curing age of 28 days, all values are resulted from simulations	95
3.13	Influences of water/cement ratio, compared at the same curing age of 28 days	97
3.14	Influences of water/cement ratio, compared at the same degree of hydration 69%	99
3.15	Mineral compositions of the special cements	100
3.16	Degree of hydration and phase segmentation for the special cement pastes at the curing age of 28 days, corresponding with Figure 3.37	102
3.17	Global mechanical properties of the special cement pastes at the curing age of 28 days, corresponding with Figure 3.38	107
4.1	A normal concrete mix	124
4.2	Particle size sieve ranges for the sands in mortar	124
5.1	Mechanical properties of the cement paste specimen of the size $100\ \mu\text{m} \times 100\ \mu\text{m} \times 100\ \mu\text{m}$, corresponding with Figure 5.2	132
5.2	Simulated mechanical properties for cement paste at microscale and mesoscale respectively	133
5.3	Scale division and specifications of the specimens	135
5.4	Local mechanical properties of sand, cement paste and interface elements in mortar at mesoscale	136
5.5	Local mechanical properties of stone, mortar and interface elements in concrete at mesoscale	139
5.6	Simulated mechanical properties of concrete at mesoscale, corresponding with Figure 5.10	140

Symbols

α_M	bending influence factor
α_N	normal force influence factor
ϵ	strain
κ	shear correction factor
ν	Poisson's ratio
σ	stress
A	cross-sectional area of lattice element
a_{nm}	spherical harmonic coefficients which are complex numbers
E	Young's modulus
f_t	tensile strength
G	shear modulus
G_F	fracture energy
I	moment of inertia
J	polar moment of inertia
l	length of lattice element
M	bending moment
N	normal force
$P_n^m(\cos \theta)$	associated Legendre polynomials

SYMBOLS

R	radius of particle
r	radius of lattice element cross-section
$r(\theta, \phi)$	a function defined in spherical coordinate system which represents the shape of a particle
W	cross-sectional factor for bending resistance
$Y_n^m(\theta, \phi)$	spherical harmonic functions

Chapter 1

Introduction

1.1 Background

Cement-based materials, such as cement paste, mortar and concrete, have a multiphase heterogeneous structure at microscale/mesoscale. In cement paste the size of cement grain particles is in the range of $0.5 \sim 50 \mu\text{m}$, the sands in mortar have the sizes of $0.1 \sim 4 \text{ mm}$, and the coarse aggregates in concrete are sized $4 \sim 32 \text{ mm}$. Cement paste is classified as heterogeneous material at microscale, but it can be homogenized at a higher scale. This principle also applies to mortar and concrete, which are deemed as heterogeneous materials at mesoscale and can be regarded as homogeneous materials at macroscale.

The global mechanical performance of materials is determined by the material structures and the local properties of constituents. The constituents also have their own material structures at a lower scale, which determine their mechanical properties. Take cement-based materials as an example. Concrete is a composite material consisting of coarse aggregates and mortar. The global mechanical behavior of concrete is determined by the material structure of concrete and the mechanical properties of coarse aggregates and mortar. At a lower scale mortar is made up with sands in cement paste. The properties of mortar are related to the material structure of mortar, as well as the local properties of sands and cement paste.

The fracture processes in concrete, mortar and cement paste must be relevant from a multiscale study point of view. The research about multiscale failure

1. INTRODUCTION

modeling has received comprehensive investment during the last decades, as researchers keep looking for the origin of the load bearing capacity of materials. The macroscopic mechanical properties of concrete, such as Young's modulus and compressive strength, are often of interest to the structural engineers. But to answer the question why concrete has these properties, it is necessary to turn attention to what is happening at a lower scale during the failure of concrete. The research work in this area helps to explain the damage mechanisms, to improve the mechanical properties and to design better cement-based materials.

1.2 State of the art

Homogenization method [1] and concurrent method [2] are usually employed to address the failure modeling problem of heterogeneous materials. The homogenization method applies when the scales can be ideally divided and separated, while the concurrent method is used when the scales are somehow coupled. Generally speaking the homogenization method consumes less computational resources, and the concurrent method provides more accurate simulation results.

Suppose that there is a piece of heterogeneous material, and it is meshed into a network of blocks. The homogenization method requires that each block of heterogeneous material is taken out and isolated to evaluate its mechanical properties, and then these properties are used as the homogenized properties of the blocks and are put back to the network to simulate the global performance of the original piece of material. The concurrent method demands that the connection between neighboring blocks is preserved and the boundaries of blocks remain compatible with each other during the simulation, the stress and strain fields also remain the same as if the domain was not decomposed.

In this thesis the concept of homogenization is adapted and combined with 3D lattice fracture analysis [3] to develop a parameter-passing multiscale modeling scheme. In addition the HYMOSTRUC3D model [4] is used to simulate the cement hydration and microstructure formation process at microscale, and the Anm material model (see Chapter 4 for details) is proposed and implemented to simulate the material structures of mortar and concrete with irregular shape particles at mesoscale.

1.3 Objectives and methodology of this research

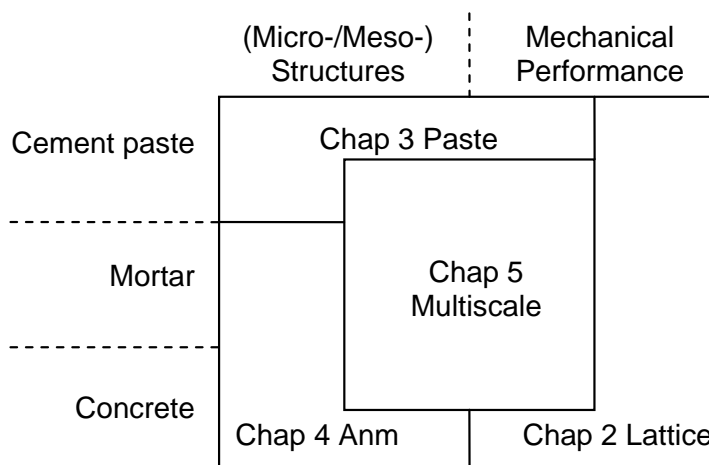


Figure 1.1: Layout of the thesis main body

1.3 Objectives and methodology of this research

The work in this research aims at developing a set of algorithms and procedures, which enable the multiscale modeling of fracture processes in cementitious materials, such as cement paste, mortar and concrete.

In this thesis there are two types of models serving as the fundamental tools, which include a material model to simulate the material structures, and a mechanical model to evaluate the mechanical performance of material structures. These two types of models can be combined to study the fracture processes at a single scale, while the multiscale modeling scheme makes it possible that the data exchange between different scales can be done by passing parameters. Examples are given to illustrate how these models can be used in a coupled way to solve practical problems.

1.4 Outline of the thesis

The thesis discusses the multiscale modeling of fracture processes in cementitious materials. It is divided into six chapters, including an introduction (Chapter 1) and conclusions (Chapter 6). The layout of the main body is given in Figure 1.1.

1. INTRODUCTION

Chapter 1 introduces the multiscale problems to be addressed in this thesis. Cement paste, mortar and concrete are studied numerically for their mechanical performance. The relations between these three cementitious materials are emphasized in the parameter-passing multiscale modeling scheme developed in this thesis.

Chapter 2 deals with the 3D lattice fracture model. The mechanical performance of cement paste, mortar and concrete can be evaluated by the 3D lattice fracture analysis. Quadrangular lattice mesh, uniaxial tensile test setup, fracture processes simulation, stress-strain response, microcracks propagation and cracks pattern in final failure state are discussed in detail.

Chapter 3 focuses on the cement paste at microscale. The microstructures of cement paste can be obtained through the computer modeling program HY-MOSTRUC3D model, as well as the experimental method of micro computed tomography. The lattice fracture model is employed to predict the uniaxial tensile properties based on the microstructures. Various factors are examined to evaluate their influences on the mechanical performance of cement paste, including the degree of hydration, cement fineness, water/cement ratio and mineral composition of cement.

Chapter 4 proposes an innovative model to simulate the material mesostructures of mortar and concrete: the Anm material model. From modeling point of view the material structures of mortar and concrete can be represented by particles embedded in matrix. The particle shapes are irregular in reality and the spherical harmonics provides a good mathematical representation of irregular shapes. The Anm material model parks multiple irregular shape particles together into an empty container to stand for the mesostructures of mortar and concrete. The parking algorithm is illustrated in detail, and examples are given to show how the mesostructures of mortar and concrete can be simulated respectively.

Chapter 5 makes use of all the tools discussed in previous chapters to address two types of multiscale modeling problems: for cement paste only but at different sizes, and for the integrated system of cement paste, mortar and concrete at microscale/mesoscale. The scale division and parameter-passing scheme are

discussed, and the domain decomposition modeling technique is also employed to solve the length scale overlap.

Chapter 6 summarizes the work and achievements in this thesis and presents all the findings in a brief way. An outlook is also given for the further development and potential future use of the algorithms and numerical models proposed in this thesis.

1. INTRODUCTION

Chapter 2

Three-dimensional Lattice Fracture Model

2.1 Background

Numerical modeling of fracture processes in brittle materials, such as cement paste, mortar, concrete and rocks, started in the late 1960s with the landmark papers of Ngo and Scordelis [5] and Rashid [6], in which the discrete and smeared crack models were introduced. Especially the latter approach gained much popularity, and in the 1970s comprehensive efforts were invested in developing constitutive models in a smeared setting which could reproduce the experimentally observed stress-strain characteristics of concrete. However, neither of them could tell the fracture processes in detail. In the 1990s, Schlangen and van Mier proposed another model to compensate the drawbacks of discrete and smeared crack models, which is called lattice fracture model [7].

The concept of lattice was proposed by Hrennikoff in the 1940s to solve elasticity problems using the framework method [8]. In the 1970s and 1980s the lattice model was introduced in theoretical physics to study the fracture behavior of disordered media [9, 10]. In the field of material sciences, a model was proposed by Burt and Dougill to simulate uniaxial extension tests, which consists of a plane pin-jointed random network structure of linear elastic brittle members having a range of different strengths and stiffnesses [11].

2. THREE-DIMENSIONAL LATTICE FRACTURE MODEL

In the last two decades, plenty of efforts have been made to develop the lattice fracture model in a variety of different settings: regular/irregular network, triangular/quadrangular mesh, truss/beam element, the way to implement heterogeneity (random distribution of local properties/microstructure mapping) and whether to introduce the softening at the element level. A lattice system of truss elements was constructed based on a random particle model to study the fracture of aggregate or fiber composites by Bazant et al. [12]. The tension softening response of the matrix phase was implemented in the lattice fracture analysis for concrete by Arslan et al. [13]. The fracture of particle composites due to large deformation was investigated by Karihaloo et al. using lattice fracture model [14]. Vervuurt made use of lattice fracture analysis to study the interface fracture in concrete [15], and van Vliet investigated the size effect in tensile fracture of concrete and rock [16]. The size effect on strength in numerical concrete was also studied by Man, where the influences of aggregate density and shape were discussed [17]. An irregular lattice model was proposed by Bolander and Sukumar for simulating quasistatic fracture in softening materials, in which accurate modeling of heterogeneity is enabled by constructing the lattice geometry on the basis of a Voronoi discretization of the material domain [18]. Lattice modeling of uniaxial compression was studied and applied to normal concrete, high strength concrete and foamed cement by Caduff and van Mier [19]. Grassl and Davies modeled corrosion induced cracking and bond in reinforced concrete using lattice approach [20]. Fracture laws for simulating compressive fracture in lattice-type models were explored and discussed by van Mier [21]. The possibility of modeling self-healing of cementitious materials using lattice approach was investigated by Joseph [22].

In the lattice fracture model, the continuum is replaced by a lattice of beam elements. Subsequently, the microstructure of the material can be mapped onto these beam elements by assigning them different properties, depending on whether the beam element represents a grain or matrix. Detailed modeling procedures are given in Section 2.2. Various conventional laboratory experiments like uniaxial tensile test, compressive test, shear test, bending test and torsional test can be simulated by the lattice fracture model and the model can be applied towards

a wide range of multiphase materials, such as concrete [3], cement paste [23], graphite and fiber reinforced concrete [24].

The lattice fracture model can solve both 2D and 3D problems as the principles are the same. The differences mainly exist in the computational resources requirements in terms of computer memory and computing time. Hence comprehensive efforts were made to reduce the memory demand by employing a matrix free linear algebraic equation solver [25]. The pre-conditioned conjugate gradient algorithm is also applied to guarantee the convergence of solutions to linear equations resulting from very large size lattice structure. Parallel computing for lattice fracture analysis is a good solution to save computational time and be able to analyze even larger lattice structure [26]. A parallel computer implementation of lattice fracture model for shared memory architecture computers was developed by Qian et al. in 2009, in which OpenMP API (Application Program Interface) was used in combination with the host programming language C++.

2.2 Modeling procedures

The lattice fracture model can simulate the stress-strain response, cracks pattern and microcracks propagation, based on the microstructure or mesostructure of the material in question. Three stages are defined to make the modeling procedures clear: pre-processing, fracture processes simulation and post-processing. In the pre-processing stage, a lattice network is constructed and the local mechanical properties are assigned to every lattice element, and then appropriate boundary conditions are imposed, depending on the type of the test to be simulated (e.g. uniaxial tensile test, bending test, shear test). The fracture processes are simulated by removing the critical element from the system one after one, representing the microcrack occurrence. The critical lattice element is the element with the highest stress/strength ratio. In the post-processing stage, the stress-strain response diagram and the cracks pattern can be obtained, and the microcracks propagation can be animated as well. An overview of the lattice fracture analysis is given in Figure 2.1.

2. THREE-DIMENSIONAL LATTICE FRACTURE MODEL

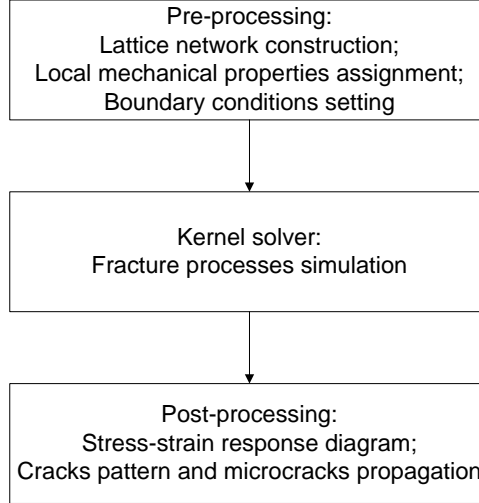


Figure 2.1: An overview of the lattice fracture analysis

2.2.1 Lattice network construction

A lattice network can be constructed based on the microstructure of materials. Two construction methods are presented in this subsection, which are `ImgLat` (Image to Lattice) and `HymLat` (Hymostruc3D to Lattice). The first method, `ImgLat`, is good for any microstructure in terms of voxels, and the second one, `HymLat`, can only be applied to a spherical particles embedded microstructure. The construction method `ImgLat` is more general and has a wider range of applications, as a spherical particles embedded microstructure can always be converted into a voxel-based digital image. However, the lattice network resulting from the second construction method `HymLat` usually has less nodes and elements, and thus costs less computational resources for the fracture processes simulation. During the lattice network construction, the following parameters need to be determined: location of lattice node, and length, radius, Young's modulus, shear modulus and tensile strength of lattice element (the cross-section is assumed to be circular for simplicity).

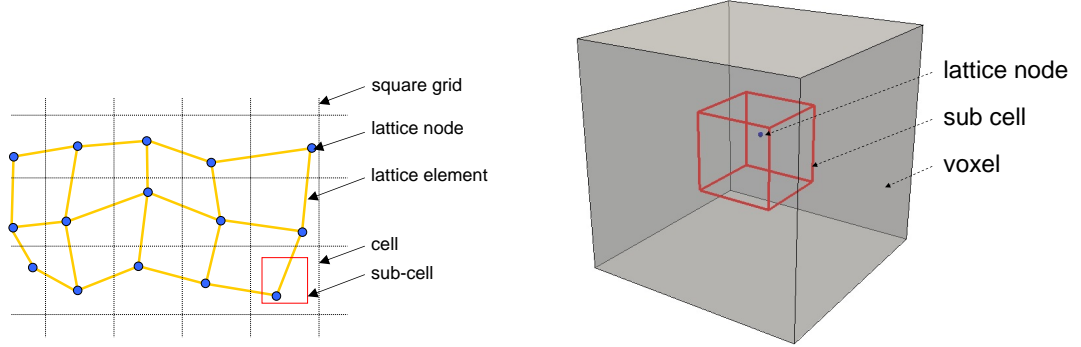


Figure 2.2: Lattice network construction for general material and scale

General construction method ImgLat: applicable to voxel-based digital image

The lattice network construction is illustrated in Figure 2.2. The sketch at left side is shown in 2D for a more clear illustration, and the mesh method also works for 3D case. A digital image consisting of multiple phases can be taken as the basis for the lattice mesh. A network of cells is generated first, and a sub-cell can be defined within each cell. A lattice node is randomly chosen within each sub-cell which represents solid phase. The pore phase cells do not generate any lattice node. Then the lattice nodes in the neighboring cells are connected by lattice beam elements, which eventually form a lattice network system. The lattice system is able to carry loads and thus replaces the original continuum materials in terms of mechanical performance. The lattice network shown in Figure 2.2 is quadrangular. Alternatively it can also be meshed to a triangular system. If a perfect regular lattice network is generated, then the quadrangular option leads to the Poisson's ratio 0, while the triangular one not. The above construction method implements the heterogeneity of the materials through the network geometry irregularities. It is also possible to achieve this by assigning random local mechanical properties to different lattice beam elements. See [3, 25, 27, 28] for more information about the construction of random lattice network.

The length ratio of the sub-cell to the cell is defined as the randomness of the lattice system, which represents the disorder of the materials. The value of the randomness is in the range of $[0, 1]$. When it takes 0, the lattice node is always

2. THREE-DIMENSIONAL LATTICE FRACTURE MODEL

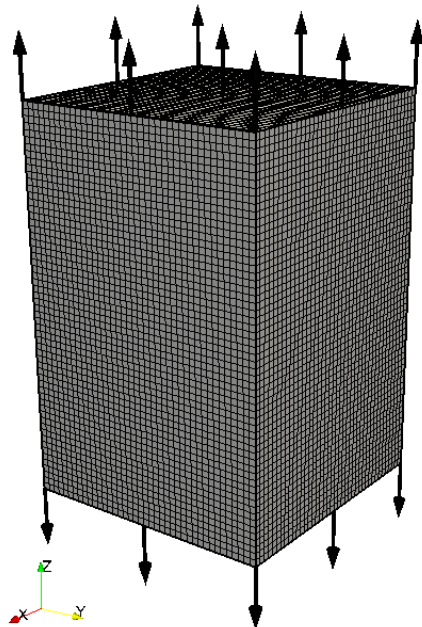


Figure 2.3: Prism of the size $40 \text{ mm} \times 40 \text{ mm} \times 60 \text{ mm}$ subject to uniaxial tensile load

located at the center of the cell, and a perfect quadrangular lattice system is generated, but the Poisson's ratio of the materials represented is restricted to 0. When the randomness is equal to 1, the sub-cell becomes identical to the cell, and the materials have the maximum degree of disorder. The choice of randomness affects the simulated fracture behavior of the materials, and the following numerical experiment is carried out to show the influence of randomness on the simulated mechanical properties of single phase perfect homogeneous materials.

A specimen in the shape of a prism at the size $40 \text{ mm} \times 40 \text{ mm} \times 60 \text{ mm}$ is analyzed for its global mechanical properties through a uniaxial tensile test by lattice fracture model. It is modeled as a single phase homogeneous material and represented in terms of voxels at the resolution 1 mm/voxel , as shown in Figure 2.3.

A lattice network is constructed based on the voxel image. In each voxel, a sub-cell is created, and the length ratio of the sub-cell to the voxel is the randomness. A lattice node is positioned randomly within the sub-cell, and then the neighboring lattice nodes are connected to form lattice elements as shown in

Table 2.1: System size of the prism in Figure 2.3

Number of voxels:	$40 \times 40 \times 60 = 96000$
Number of lattice nodes:	96000
Number of lattice elements:	$39 \times 40 \times 60 \times 2 + 59 \times 40 \times 40 = 281600$

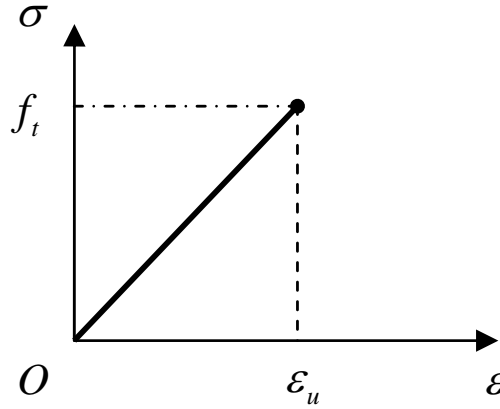


Figure 2.4: Linear-brittle constitutive law of lattice elements

Figure 2.2. The system size of the resulting lattice network is listed in Table 2.1. The lattice elements follow linear-brittle constitutive law as shown in Figure 2.4 and the corresponding local mechanical properties are given in Table 2.2.

During the lattice network construction, the randomness is varied at 0, 0.25, 0.5, 0.75 and 1 respectively in the computational model to study its influence on the simulated global mechanical properties. At each randomness, three instances are taken using different random seed 1, 2 and 3 respectively. The random seed controls the pseudo random number sequence in the C++ programming language, thus the resulting lattice networks would be different using different random seeds,

Table 2.2: Local mechanical properties of lattice elements in Figure 2.4

Young's modulus E (GPa)	Shear modulus G (GPa)	Poisson's ratio ν	Tensile strength f_t (MPa)
35	14	0.25	3.5

2. THREE-DIMENSIONAL LATTICE FRACTURE MODEL

Table 2.3: Simulation configurations with regard to lattice network construction

Randomness	0	0.25	0.5	0.75	1
Random seed	1/2/3	1/2/3	1/2/3	1/2/3	1/2/3

even though at the same randomness, but the global properties should be more or less the same. The simulation configurations with regard to lattice network construction are summarized in Table 2.3, and in total 15 simulations are executed.

The specimen is loaded in vertical direction as shown in Figure 2.3. The external surface load is imposed on the top and the bottom surface is fixed. All the other four side surfaces are free to expand/shrink. The lattice elements on the top and bottom boundaries are not allowed to be broken during the fracture processes as the external load requires a path into the specimen.

The fracture processes of the prisms are simulated using lattice fracture model, and the simulated global Young's modulus E , tensile strength f_t and fracture energy G_F are presented in Table 2.4.

From the Table 2.4 it is concluded that the influences of using different random seeds to generate the pseudo random number sequences can be neglected, but the choice of randomness really matters the simulation results. When the randomness is taken as 0, the simulated global Young's modulus and tensile strength are the same as the local mechanical properties inputs, and all the microcracks are located on one plane as shown in Figure 2.5, which is due to the fact that a piece of perfect homogeneous material is modeled. The increase of the randomness results in a decrease of the simulated global Young's modulus and tensile strength, as artificial disorder of the materials is introduced gradually by increasing the randomness in the model. The change of fracture energy is somehow more complicated, as it decreases first and then increases again. The decrease of the fracture energy is because of the decrease of the strength, and the increase is due to the fact that more microcracks are generated with more heterogeneous materials. These two forces push the change of fracture energy in opposite directions, and the decrease of strength wins when the randomness is still small, but the more microcracks become dominant when the randomness is

2.2 Modeling procedures

Table 2.4: Influence of randomness on the simulated global Young's modulus E , tensile strength f_t and fracture energy G_F

Randomness	Random seed	Young's modulus E (GPa)	Tensile strength f_t (MPa)	Fracture energy G_F (J/m ²)
0	1	35.0	3.50	0.753
	2	35.0	3.50	0.753
	3	35.0	3.50	0.753
	Average properties:	35.0	3.50	0.753
0.25	1	33.8	3.08	0.589
	2	33.8	3.03	0.661
	3	33.8	3.06	0.591
	Average properties:	33.8	3.06	0.614
0.5	1	30.8	2.64	0.644
	2	30.8	2.66	0.637
	3	30.8	2.66	0.644
	Average properties:	30.8	2.65	0.642
0.75	1	26.8	2.28	0.717
	2	26.8	2.22	0.722
	3	26.8	2.29	0.698
	Average properties:	26.8	2.26	0.712
1	1	22.8	1.95	0.981
	2	22.8	1.94	1.009
	3	22.8	1.91	0.911
	Average properties:	22.8	1.93	0.967

2. THREE-DIMENSIONAL LATTICE FRACTURE MODEL

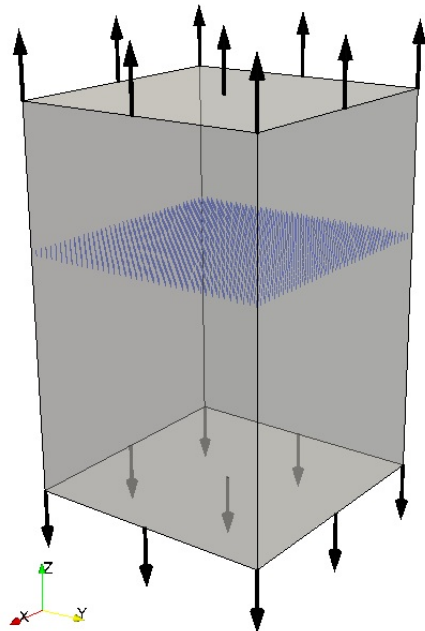


Figure 2.5: Microcracks pattern of perfect homogeneous material subject to uniaxial tension

large enough. The diagram of simulated global mechanical properties reduction against the randomness is shown in Figure 2.6.

The randomness defined in the lattice mesh represents the heterogeneity of the materials in reality. The following procedures may be employed to determine the value of randomness. The first step is to obtain the material structure of the specimen through CT scan (see Subsection 3.1.3 for more information), and then construct a lattice network based on the material structure with different values of randomness. Afterwards the lattice systems with different randomness values are evaluated by the lattice fracture analysis for their mechanical properties such as Young's modulus and tensile strength. The simulated mechanical properties are compared with the measured value to find out the best simulation, and it is concluded that the randomness used in the best simulation is the correct one.

The next step after creating the lattice network is to assign local mechanical properties to all lattice elements. Either truss element or beam element may be employed in lattice fracture analysis, and the choice is dependent on the application. Generally speaking beam elements are preferred as a beam network can

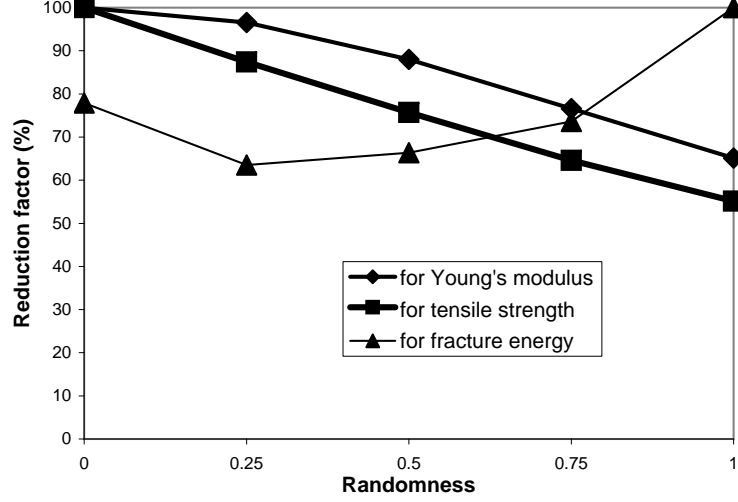


Figure 2.6: Simulated global mechanical properties reduction against randomness

simulate a wider range of Poisson's ratios and more complicated crack patterns [25, 29].

The local mechanical properties of a lattice element is determined by the location of the element, whether it is within a grain or in the matrix, or it connects a grain to the matrix, as shown in Figure 2.7. If both ends of an element are located in the same phase, then this element is assigned the same mechanical properties as the phase in question, otherwise it is classified as an interface element. The mechanical properties of an interface element are preferred to be measured in laboratory test, but in case of lack of experimental data, the following guidelines may be applied. The Young's modulus of an interface element is the harmonic average of the Young's moduli of the grain and the matrix, and its tensile strength takes the lower value of the two phases, as determined by the equation (2.1) and the equation (2.2). Shear modulus of an interface element is determined in a similar way to the determination of its Young's modulus.

$$\frac{2}{E_I} = \frac{1}{E_A} + \frac{1}{E_B} \quad (2.1)$$

in which E_I , E_A and E_B are the Young's modulus for interface element, phase A and phase B respectively.

$$f_{t_I} = \min(f_{t_A}, f_{t_B}) \quad (2.2)$$

2. THREE-DIMENSIONAL LATTICE FRACTURE MODEL

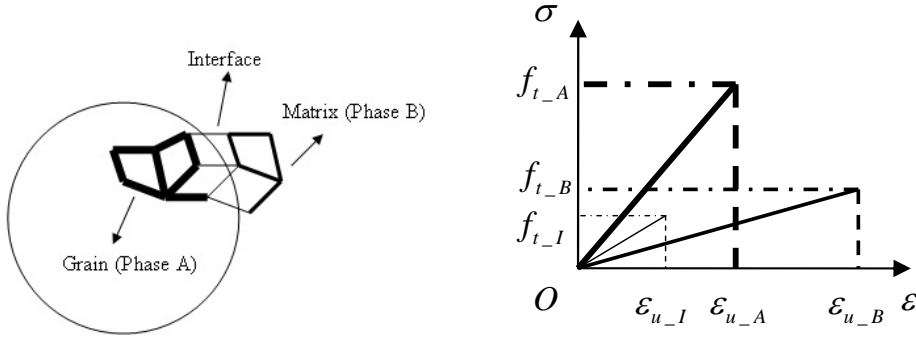


Figure 2.7: Lattice element type determination and its constitutive relation

where f_{t_I} , f_{t_A} and f_{t_B} are the tensile strength for the interface element, phase A and phase B respectively.

Special construction method HymLat: only applicable to spherical particles embedded microstructure

Having introduced the general lattice network construction method for voxel-based microstructure of materials, a special construction method is also developed for the spherical particles embedded microstructure of cement paste from the HYMOSTRUC3D model. A sample of the microstructure simulated by the HYMOSTRUC3D model is given in Figure 2.8. Details about the simulation of microstructures of cement paste can be found in Chapter 3. In total four phases are presented in the microstructure, including one pore (P) phase and three solid phases which are unhydrated cement (U), inner product (I) and outer product (O).

During the lattice network construction, a lattice element is generated if the two particles have overlap, as shown in the Figure 2.9(a). The lattice element goes from the center of the first particle to the center of the other one. The cross-section of the lattice element is assumed to be circular and its area is equal to the contact area of the two particles in question. This construction principle applies to all the pairs of overlapped particles, thus a lattice network can be created, as shown in Figure 2.9(b) for the case of three pairs.

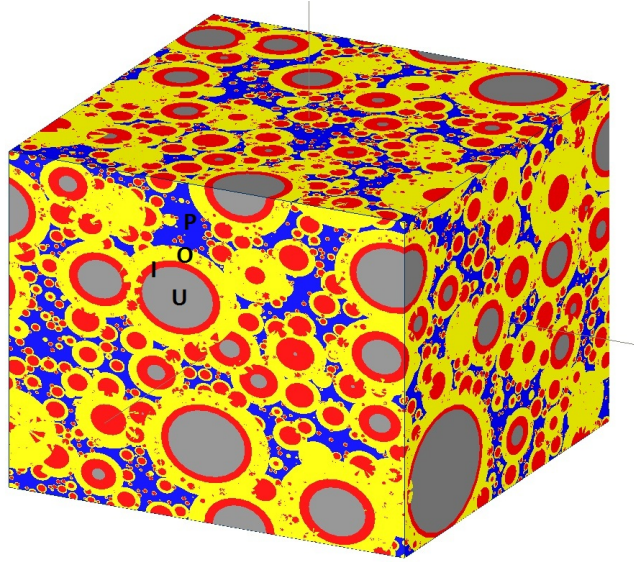


Figure 2.8: Microstructure of cement paste simulated by the HYMOSTRUC3D model

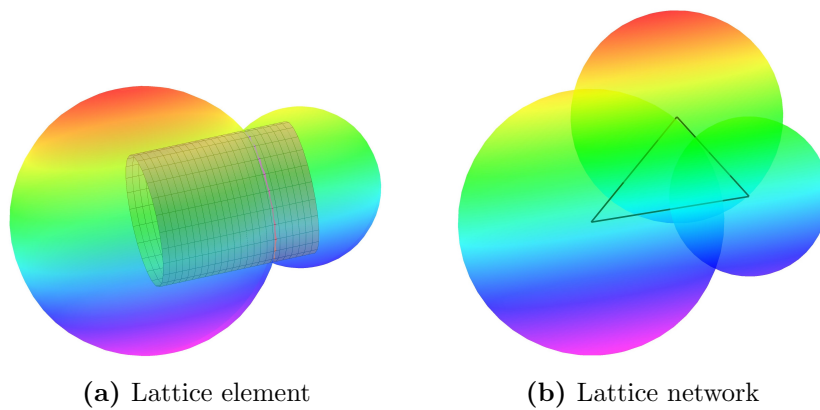


Figure 2.9: 3D contact particles, lattice element and network

2. THREE-DIMENSIONAL LATTICE FRACTURE MODEL

The determination of Young's modulus of a lattice element is through a two-step averaging. The particle modulus is computed as a result of the length-weighted harmonic average modulus of unhydrated cement, inner product and outer product, as determined by the equation (2.3) and illustrated in Figure 2.10,

$$\frac{R_O}{E_p} = \frac{R_U}{E_U} + \frac{R_I - R_U}{E_I} + \frac{R_O - R_I}{E_O} \quad (2.3)$$

where R_U , R_I and R_O are the radius for unhydrated cement, inner product and outer product respectively, E_U , E_I and E_O are the corresponding Young's modulus, E_p is the computed particle modulus. The lattice element modulus is the length-weighted harmonic average of the particle moduli of the two particles which it links. The formula depends on the two particles' relative locations, as given in the equation (2.4) and shown in Figure 2.11,

$$E = \begin{cases} \frac{lE_{p1}E_{p2}(E_{p1} + E_{p2})}{(l - R_1)E_{p1}^2 + (R_1 + R_2)E_{p1}E_{p2} + (l - R_2)E_{p2}^2} & \text{if case 1} \\ \frac{lE_{p1}(E_{p1} + E_{p2})}{(l + R_2)E_{p1} + (l - R_2)E_{p2}} & \text{if case 2} \\ \frac{E_{p1} + E_{p2}}{2} & \text{if case 3} \end{cases} \quad (2.4)$$

where R_1 and R_2 are the radius of the first and the second particle, E_{p1} and E_{p2} are the corresponding particle moduli, l is the lattice element length, and E is the computed element modulus. Shear modulus of a lattice element can be determined through the same procedures, and its tensile strength takes the lowest tensile strength among unhydrated cement, inner product and outer product, as given in the equation (2.5),

$$f_t = \min(f_{t_U}, f_{t_I}, f_{t_O}) \quad (2.5)$$

where f_{t_U} , f_{t_I} and f_{t_O} are the tensile strength for unhydrated cement, inner product and outer product respectively, and f_t is the tensile strength of the lattice element.

2.2.2 Test setup

Similarly to various laboratory experiments, many types of tests can be simulated on a lattice network, including but not limited to tensile test, three-point (four-

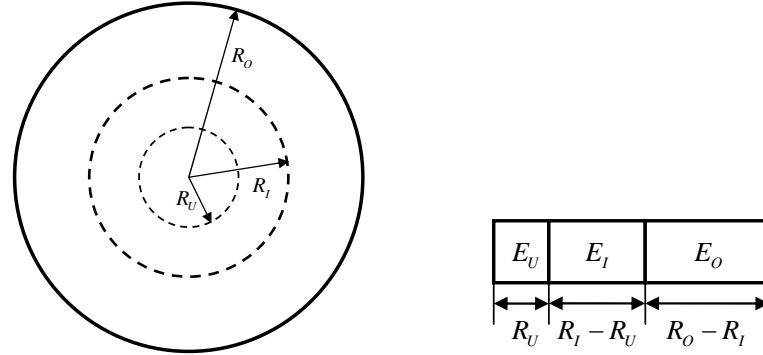
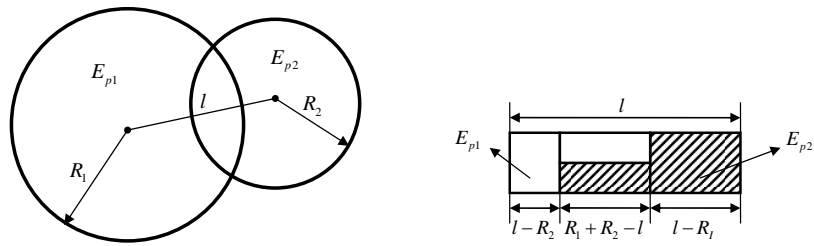


Figure 2.10: Determination of particle modulus (first step averaging)

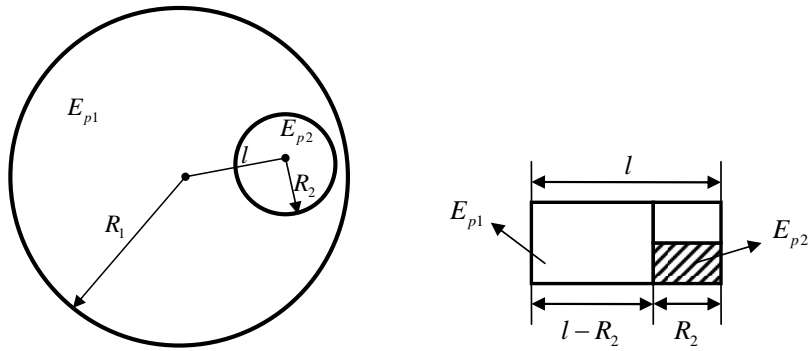
point) bending test, shear test and more. They are implemented by setting up proper boundary conditions of the sample. For example a uniaxial tensile test can be configured by fixing all the nodes on the bottom surface of the specimen and imposing a uniform surface load on the top surface, as shown in Figure 2.12. During the lattice network construction, all the layers close to the surfaces are forced to be regularly meshed, irrespective of the material randomness setting, as irregular geometry on the boundaries might create some extra stresses which may have negative influence on the fracture processes simulation. In addition all the lattice elements involved in the bottom and top layers are not allowed to be broken, even if the stress in such an element has already exceeded its strength, as the external loads need a path to be transferred into the specimen. In other words, it is assumed that all the restraint elements have infinite strength.

In the laboratory tensile test, there are two possible methods to connect the specimen to the testing device: glued and clamped. In the numerical model, these are implemented through whether or not to fix the degrees of freedom of the nodes at the bottom and top surfaces. In both cases for a tensile test, the vertical displacements of all the nodes at the bottom surface are prescribed to be 0, and the top surface to be unit deformation. In the case of a glued specimen, all the other degrees of freedom of the nodes in question are restricted to be 0. But only one node is chosen to be fixed completely in the case of a clamped specimen, as this is required to prevent possible rigid body movement. The clamped setting is suitable for the study about Poisson's ratio. The following example demonstrates

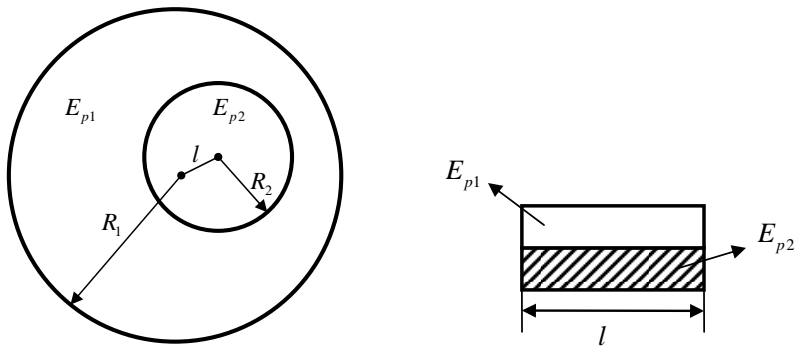
2. THREE-DIMENSIONAL LATTICE FRACTURE MODEL



(a) Case 1



(b) Case 2



(c) Case 3

Figure 2.11: Determination of lattice element modulus (second step averaging)

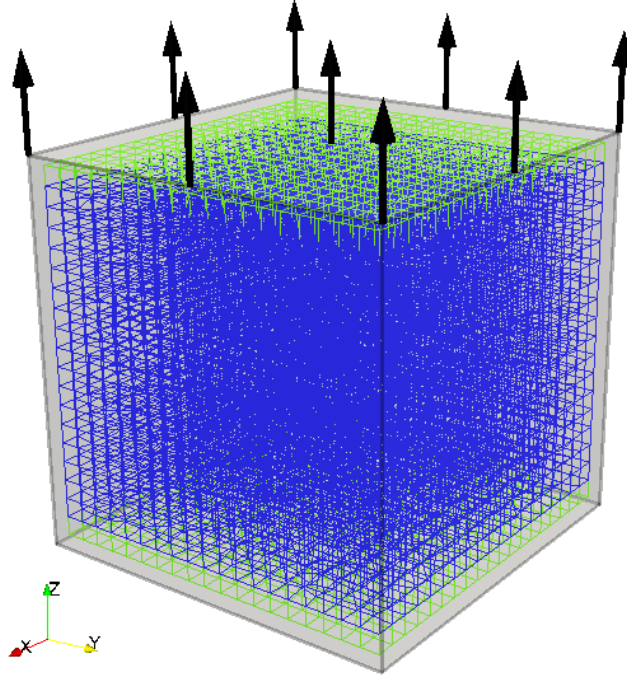


Figure 2.12: Uniaxial tensile test setup

the influences of these two different settings on the simulated global mechanical properties.

A cubic specimen of the size 20 mm at the resolution 1 mm/voxel is configured for a uniaxial tensile test using two different aforementioned boundary conditions, as shown in Figure 2.12. The input local mechanical properties are given in Table 2.2 and it behaves linear-brittle locally as shown in Figure 2.4. The randomness of the material is taken as 0.5 in the numerical experiments. The simulated global Young's modulus, tensile strength and fracture energy are presented in Table 2.5. The comparisons show that the differences are so small that they can be neglected for the glued and the clamped boundary settings, at least this is true for specimens with Poisson's ratio close to 0. If the Poisson's ratio of the specimen is far from 0, then the restriction on the boundaries will affect the deformation of side surfaces, thus the mechanical responses will be different for different boundary settings.

2. THREE-DIMENSIONAL LATTICE FRACTURE MODEL

Table 2.5: Influence of boundary settings on the simulated global Young’s modulus E , tensile strength f_t and fracture energy G_F

Boundary settings	Young’s modulus E (GPa)	Tensile strength f_t (MPa)	Fracture energy G_F (J/m ²)
Glued	31.4	2.74	0.638
Clamped	31.3	2.74	0.643

2.2.3 Fracture processes simulation

After the lattice network is constructed and boundary conditions are imposed, it is ready to proceed with the fracture processes simulation which is the kernel part in the entire lattice fracture analysis. The flowchart of lattice fracture analysis kernel solver is given in Figure 2.13. It seems similar to the traditional finite element analysis, but two major differences exist. One is about the removal of broken lattice elements from the system and the other is the absence of the explicit assembly of global stiffness matrix.

In lattice fracture analysis, a unit prescribed displacement is imposed on the system. At every analysis step it is required to determine the critical element and the corresponding system scaling factor after the calculation of comparative stress in every lattice element. The critical element is the one with highest stress/strength ratio when the system is loaded by a unit prescribed displacement. The inverse of the ratio is defined as system scaling factor. The system scaling factor, together with the reactions on the restraint boundaries, determines one scenario of critical load-displacement pairs. The critical element is removed from the system and if the system does not fail completely yet, it is recomputed as the system is updated due to the element removal. Multiple analysis steps are carried out until the system fails. Hence a set of load-displacement pairs can be obtained and used to plot the load-displacement diagram, which can be converted to a stress-strain diagram later to represent the constitutive relation of the material. The step-by-step removal of critical lattice elements indicates the microcracks evolution in the specimen. Thus the microcracks propagation and the cracks pattern in the final failure state can be simulated.

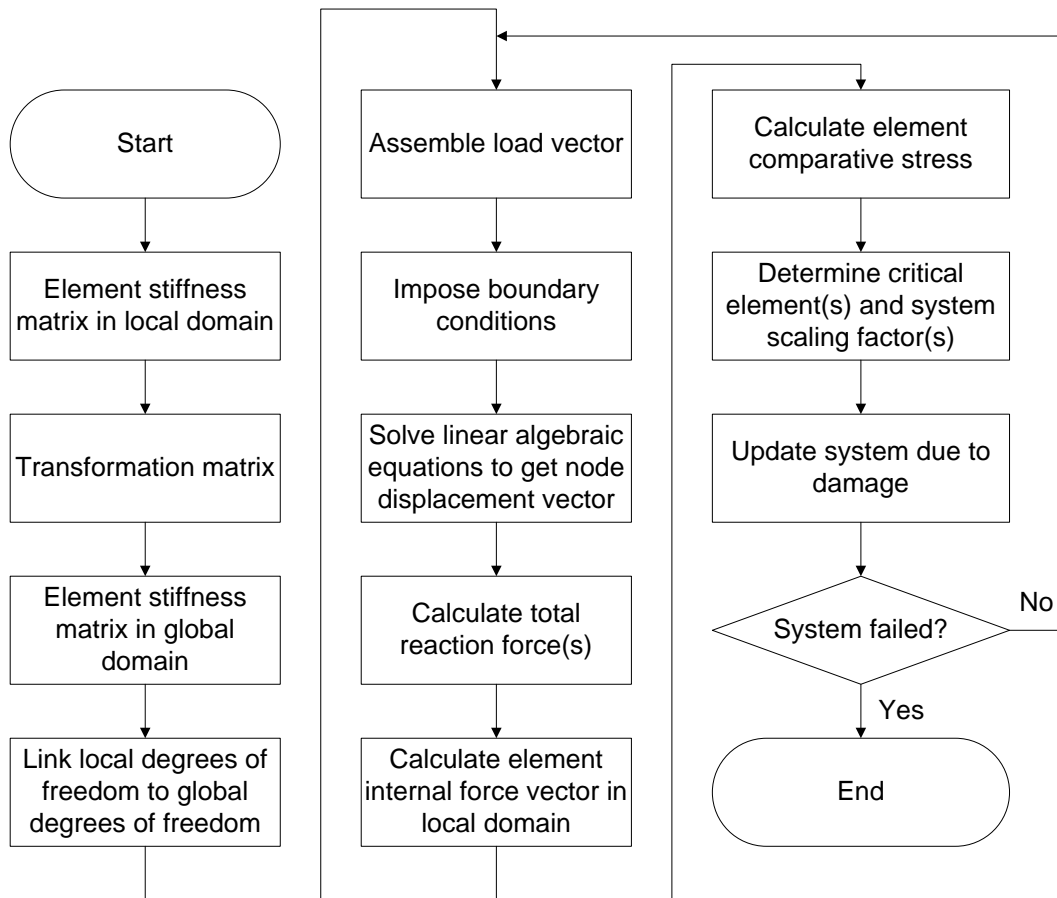


Figure 2.13: Flowchart of lattice fracture analysis kernel solver

2. THREE-DIMENSIONAL LATTICE FRACTURE MODEL

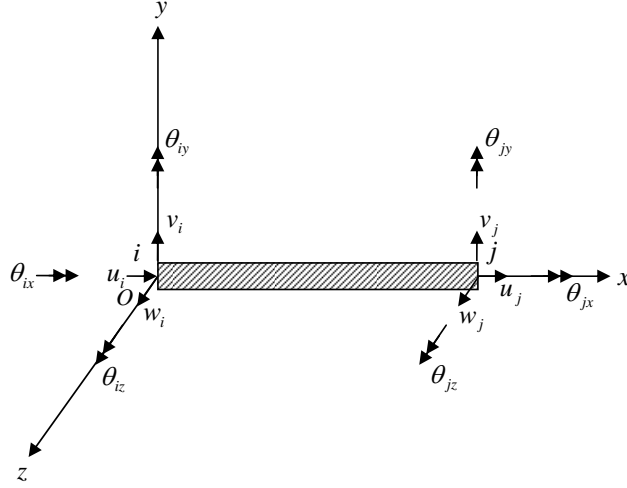


Figure 2.14: 3D lattice beam element in local domain

Another highlight in the lattice fracture analysis is the adoption of the matrix free technique in the linear algebraic equation solver to reduce the computer memory demand. The global stiffness matrix is not assembled or stored explicitly, rather than that the element stiffness matrices in global domain and the connectivity array, which links local degrees of freedom to global degrees of freedom, are sent to the equation solver directly to get the node displacement vector. Jacobi pre-conditioned conjugate gradient iterative method is employed to solve the set of linear equations. More details about the algorithm can be found later in this subsection on Page 64.

3D lattice beam element stiffness matrix in local domain and in global domain

In lattice fracture analysis, continuum materials are discretized into a network of lattice elements. The lattice beam element is a straight bar of uniform cross-section and can transmit axial forces, shear forces, bending moments and torsional moments as shown in Figure 2.14. The formulation of a 3D lattice beam element stiffness matrix is based on the Timoshenko beam theory, which can be found in many textbooks about Finite Element Analysis.

The 3D lattice beam element has two nodes and each node has six degrees

of freedom including three translational and three rotational degrees of freedom. The element stiffness matrix in local domain is of the size 12×12 and can be formulated by assembling axial component, torsional component, bending and shear components in the planes xOy and xOz . The element cross-sectional bending and shear centers are assumed to be coincident.

Along the axial direction as shown in Figure 2.14, the kinematics, equilibrium and constitutive equations are,

$$\begin{cases} \epsilon_x(x) = \frac{du(x)}{dx} \\ A \frac{d\sigma_x(x)}{dx} + f(x) = 0 \\ \sigma_x(x) = E\epsilon_x(x) \end{cases} \quad (2.6)$$

where E is the axial elastic modulus, A is the cross-sectional area of the element, $f(x)$ is the external body force along the axial direction, $\sigma_x(x)$, $\epsilon_x(x)$ and $u(x)$ are the stress, strain and displacement respectively.

The strong form of the axial governing equation can be derived from the equations (2.6) and it is

$$EA \frac{d^2u(x)}{dx^2} + f(x) = 0 \quad (2.7)$$

The corresponding Dirichlet and Neumann boundary conditions are

$$\begin{cases} u(x) = u_0 & \text{on } \Gamma_u \\ EA \frac{du(x)}{dx} n = P_0 & \text{on } \Gamma_F \end{cases} \quad (2.8)$$

where u_0 and P_0 are the given displacement and force at the boundaries respectively, n is the outward unit normal vector, Γ represents the boundaries of the element and it satisfies

$$\Gamma_u \cup \Gamma_F = \Gamma, \Gamma_u \cap \Gamma_F = \emptyset \quad (2.9)$$

To develop the weak form of the governing equation, the strong form equation (2.7) needs to be multiplied by a scalar weight function $w(x)$, which comes from an appropriately defined space V . An important requirement on the space V is that weight functions $w(x)$ be zero where Dirichlet boundary conditions

2. THREE-DIMENSIONAL LATTICE FRACTURE MODEL

are applied. Multiplying the equation (2.7) by the weight function $w(x)$ and integrating over the element Ω yields

$$\int_{\Omega} w(x)EA \frac{d^2u(x)}{dx^2} d\Omega + \int_{\Omega} w(x)f(x)d\Omega = 0 \quad (2.10)$$

Applying integration by parts once yields

$$- \int_{\Omega} \frac{dw(x)}{dx} EA \frac{du(x)}{dx} d\Omega + \int_{\Gamma} w(x)EA \frac{du(x)}{dx} nd\Gamma + \int_{\Omega} w(x)f(x)d\Omega = 0 \quad (2.11)$$

As the boundary Γ can be decomposed into two parts Γ_u and Γ_F , the above equation can be re-written as

$$\begin{aligned} - \int_{\Omega} \frac{dw(x)}{dx} EA \frac{du(x)}{dx} d\Omega + \int_{\Gamma_u} w(x)EA \frac{du(x)}{dx} nd\Gamma \\ + \int_{\Gamma_F} w(x)EA \frac{du(x)}{dx} nd\Gamma + \int_{\Omega} w(x)f(x)d\Omega = 0 \end{aligned} \quad (2.12)$$

The term $\int_{\Gamma_u} w(x)EA \frac{du(x)}{dx} nd\Gamma$ is always equal to zero as by definition the weight function $w(x)$ is equal to zero at Dirichlet boundary. The weak form of the governing equation can be obtained by inserting the Neumann boundary condition (2.8) into the above equation. Solving it involves to find a trial function $u(x) \in S$ such that

$$- \int_{\Omega} \frac{dw(x)}{dx} EA \frac{du(x)}{dx} d\Omega + \int_{\Gamma_F} w(x)P_0 d\Gamma + \int_{\Omega} w(x)f(x)d\Omega = 0 \quad \forall w(x) \in V \quad (2.13)$$

where S is an appropriately defined space of functions which satisfies the Dirichlet boundary condition (2.8). The mathematical description for the spaces S and V is that

$$\begin{cases} S = \{u(x) \mid u(x) \in \mathcal{L}(\Omega), u(x) = u_0 \text{ on } \Gamma_u\} \\ V = \{w(x) \mid w(x) \in \mathcal{L}(\Omega), w(x) = 0 \text{ on } \Gamma_u\} \end{cases} \quad (2.14)$$

Based on the weak form of the governing equation (2.13), a Galerkin problem can be formulated which involves to find $u^h(x) \in S^h$ such that

$$\int_{\Omega} \frac{dw^h(x)}{dx} EA \frac{du^h(x)}{dx} d\Omega = \int_{\Gamma_F} w^h(x)P_0 d\Gamma + \int_{\Omega} w^h(x)f(x)d\Omega \quad \forall w^h(x) \in V^h \quad (2.15)$$

where $S^h \subset S$ and $V^h \subset V$ are finite-dimensional spaces.

The Galerkin method (more specifically, the Bubnov-Galerkin method) requires that the trial function and the weight function come from the same finite-dimensional space, taking into account the requirements on the trial and weight functions where Dirichlet boundary conditions are applied.

To find the solution to the Galerkin problem (2.15), Lagrange polynomials can be used to construct the shape functions, which results in a linear interpolation of the displacement field in the element,

$$u^h(x) = N_i(x)u_i + N_j(x)u_j \quad (2.16)$$

where u_i and u_j are the axial displacements at node i and j respectively, and the shape functions are

$$\begin{cases} N_i(x) = 1 - \frac{x}{l} \\ N_j(x) = \frac{x}{l} \end{cases} \quad (2.17)$$

Denoting that

$$\underline{N}(x) = [N_i(x) \quad N_j(x)] \quad (2.18)$$

and

$$\underline{a}_e = \begin{Bmatrix} u_i \\ u_j \end{Bmatrix} \quad (2.19)$$

Thus the displacement field (2.16) can be re-written as

$$u^h(x) = \underline{N}(x)\underline{a}_e \quad (2.20)$$

The first derivative of the trial function $u^h(x)$ is given by

$$\frac{du^h(x)}{dx} = \frac{d\underline{N}(x)}{dx}\underline{a}_e \quad (2.21)$$

Similarly the weight function and its first derivative are given by

$$w^h(x) = \underline{N}(x)\underline{b}_e \quad (2.22)$$

and

$$\frac{dw^h(x)}{dx} = \frac{d\underline{N}(x)}{dx}\underline{b}_e \quad (2.23)$$

2. THREE-DIMENSIONAL LATTICE FRACTURE MODEL

Inserting the equations (2.21), (2.22) and (2.23) into the Galerkin problem (2.15) yields

$$\begin{aligned} \int_{\Omega} \left[\frac{dN(x)}{dx} \underline{b}_e \right]^T EA \left[\frac{dN(x)}{dx} \underline{a}_e \right] d\Omega \\ = \int_{\Gamma_F} [\underline{N}(x) \underline{b}_e]^T P_0 d\Gamma + \int_{\Omega} [\underline{N}(x) \underline{b}_e]^T f(x) d\Omega \end{aligned} \quad (2.24)$$

Rearranging the above equation yields

$$\int_{\Omega} \left[\frac{dN(x)}{dx} \right]^T EA \left[\frac{dN(x)}{dx} \right] d\Omega \underline{a}_e = \int_{\Gamma_F} [\underline{N}(x)]^T P_0 d\Gamma + \int_{\Omega} [\underline{N}(x)]^T f(x) d\Omega \quad (2.25)$$

Hence the element stiffness matrix for the axial deformation is given by

$$\begin{aligned} \underline{\underline{K}}_a^e &= \int_{\Omega} \left[\frac{dN(x)}{dx} \right]^T EA \left[\frac{dN(x)}{dx} \right] d\Omega \\ &= \int_0^l \begin{bmatrix} -\frac{1}{l} \\ \frac{1}{l} \end{bmatrix} EA \begin{bmatrix} -\frac{1}{l} & \frac{1}{l} \end{bmatrix} dx \\ &= \begin{bmatrix} \frac{EA}{l} & -\frac{EA}{l} \\ \text{sym.} & \frac{EA}{l} \end{bmatrix} \end{aligned} \quad (2.26)$$

where E is the axial elastic modulus, A and l are the cross-sectional area and the length of the element respectively.

The element stiffness matrix for the torsional deformation can be formulated in a similar way and is given by

$$\underline{\underline{K}}_t^e = \begin{bmatrix} \frac{GJ}{l} & -\frac{GJ}{l} \\ \text{sym.} & \frac{GJ}{l} \end{bmatrix} \quad (2.27)$$

where G is the shear modulus, J is the polar moment of inertia about the axial direction, and l is the length of the element.

The element stiffness matrix for the bending and shear deformation in the plane xOy is formulated through two steps. The first step derives the stiffness matrix for Euler-Bernoulli beam element, and then the shear effect is taken into account at the second step, thus the Timoshenko beam element is developed.

In the plane xOy as shown in Figure 2.14, the translational equilibrium requires that

$$\int_{\Gamma} q(x) n d\Gamma + \int_{\Omega} f_y(x) d\Omega = 0 \quad (2.28)$$

where $f_y(x)$ is the body force, $q(x)$ is the distributed load, n is the outward unit normal vector, Ω and Γ are the body and the boundaries of the element respectively.

Noting that $\int_{\Gamma} q(x)n d\Gamma = \int_{\Omega} \frac{dq(x)}{dx} d\Omega$, the above equation can be re-arranged as

$$\int_{\Omega} \frac{dq(x)}{dx} d\Omega + \int_{\Omega} f_y(x) d\Omega = 0 \quad (2.29)$$

Since equilibrium must hold for an infinitely small segment of a beam, it requires that

$$\frac{dq(x)}{dx} + f_y(x) = 0 \quad (2.30)$$

For rotational equilibrium, it is required that

$$\int_{\Gamma} m(x)n d\Gamma - \int_{\Gamma} q(x)n x d\Gamma - \int_{\Omega} f_y(x)x d\Omega = 0 \quad (2.31)$$

where $m(x)$ is the distributed moment.

Noting that $\int_{\Gamma} m(x)n d\Gamma = \int_{\Omega} \frac{dm(x)}{dx} d\Omega$ and integration by parts $\int_{\Omega} x \frac{dq(x)}{dx} d\Omega = - \int_{\Omega} q(x) d\Omega + \int_{\Gamma} x q(x)n d\Gamma$, the above equation can be re-written as

$$\int_{\Omega} \frac{dm(x)}{dx} d\Omega - \left[\int_{\Omega} x \frac{dq(x)}{dx} d\Omega + \int_{\Omega} q(x) d\Omega \right] - \int_{\Omega} f_y(x)x d\Omega = 0 \quad (2.32)$$

Rearranging the above equation yields

$$\int_{\Omega} \left[\frac{dm(x)}{dx} - q(x) \right] d\Omega - \int_{\Omega} \left[\frac{dq(x)}{dx} + f_y(x) \right] x d\Omega = 0 \quad (2.33)$$

The term $\int_{\Omega} \left[\frac{dq(x)}{dx} + f_y(x) \right] x d\Omega$ must be zero due to the satisfaction of the translational equilibrium (2.30), and equilibrium must hold for an infinitely small segment of a beam, hence,

$$\frac{dm(x)}{dx} - q(x) = 0 \quad (2.34)$$

The kinematics equation is based on the Euler-Bernoulli hypothesis, which is plane cross-sections remain plane and normal to the longitudinal axis after deformation. This assumption implies that the shear rotation is equal to zero, hence, the rotation can be directly related to the translational displacement,

$$\theta(x) = \frac{dv(x)}{dx} \quad (2.35)$$

2. THREE-DIMENSIONAL LATTICE FRACTURE MODEL

which also implies that

$$\kappa(x) = \frac{d\theta(x)}{dx} = \frac{d^2v(x)}{dx^2} \quad (2.36)$$

where $\kappa(x)$ is the bending curvature, $\theta(x)$ and $v(x)$ are the rotational and translational displacement respectively.

The constitutive equation relates the bending moment in the beam to the curvature by

$$m(x) = -EI_z\kappa(x) \quad (2.37)$$

where I_z is the moment of inertia of the cross-section about the z -axis.

On the basis of the equations (2.30), (2.34), (2.36) and (2.37), the strong form the the governing equation can be obtained,

$$EI_z \frac{d^4v(x)}{dx^4} - f_y(x) = 0 \quad (2.38)$$

The corresponding Dirichlet and Neumann boundary conditions are

$$\begin{cases} v(x) = v_0 & \text{on } \Gamma_v \\ \theta(x) = \theta_0 & \text{on } \Gamma_\theta \\ m(x)n = M_0 & \text{on } \Gamma_M \\ q(x)n = Q_0 & \text{on } \Gamma_Q \end{cases} \quad (2.39)$$

The Neumann boundary conditions can also be expressed in terms of translational displacement $v(x)$, which are

$$\begin{cases} -EI_z \frac{d^2v(x)}{dx^2} n = M_0 & \text{on } \Gamma_M \\ -EI_z \frac{d^3v(x)}{dx^3} n = Q_0 & \text{on } \Gamma_Q \end{cases} \quad (2.40)$$

where v_0 and θ_0 are the given translational and rotational displacement at the boundaries respectively, M_0 and Q_0 are the given moment and shear force at the boundaries respectively.

The boundary Γ of the element is partitioned such that

$$\begin{cases} \Gamma_v \cup \Gamma_Q = \Gamma, \Gamma_v \cap \Gamma_Q = \emptyset \\ \Gamma_\theta \cup \Gamma_M = \Gamma, \Gamma_\theta \cap \Gamma_M = \emptyset \end{cases} \quad (2.41)$$

To develop the weak form of the governing equation, multiplying both sides of the equation (2.38) by a weight function $w(x)$ and integrating over the beam Ω yields

$$\int_{\Omega} w(x)EI_z \frac{d^4v(x)}{dx^4} d\Omega - \int_{\Omega} w(x)f_y(x)d\Omega = 0 \quad (2.42)$$

Integrating by parts once yields

$$- \int_{\Omega} \frac{dw(x)}{dx} EI_z \frac{d^3v(x)}{dx^3} d\Omega + \int_{\Gamma} w(x)EI_z \frac{d^3v(x)}{dx^3} nd\Gamma - \int_{\Omega} w(x)f_y(x)d\Omega = 0 \quad (2.43)$$

Applying integration by parts again yields

$$\begin{aligned} & - \left[- \int_{\Omega} \frac{d^2w(x)}{dx^2} EI_z \frac{d^2v(x)}{dx^2} d\Omega + \int_{\Gamma} \frac{dw(x)}{dx} EI_z \frac{d^2v(x)}{dx^2} nd\Gamma \right] \\ & + \int_{\Gamma} w(x)EI_z \frac{d^3v(x)}{dx^3} nd\Gamma - \int_{\Omega} w(x)f_y(x)d\Omega = 0 \end{aligned} \quad (2.44)$$

The above equation can be simplified as

$$\begin{aligned} & \int_{\Omega} \frac{d^2w(x)}{dx^2} EI_z \frac{d^2v(x)}{dx^2} d\Omega - \int_{\Gamma} \frac{dw(x)}{dx} EI_z \frac{d^2v(x)}{dx^2} nd\Gamma \\ & + \int_{\Gamma} w(x)EI_z \frac{d^3v(x)}{dx^3} nd\Gamma - \int_{\Omega} w(x)f_y(x)d\Omega = 0 \end{aligned} \quad (2.45)$$

Inserting the moment part of the Neumann boundary conditions (2.40) into the term $\int_{\Gamma} \frac{dw(x)}{dx} EI_z \frac{d^2v(x)}{dx^2} nd\Gamma$ and noting that the first derivative of the weight function is equal to zero on Γ_{θ} yields

$$\begin{aligned} \int_{\Gamma} \frac{dw(x)}{dx} EI_z \frac{d^2v(x)}{dx^2} nd\Gamma &= \int_{\Gamma_M} \frac{dw(x)}{dx} EI_z \frac{d^2v(x)}{dx^2} nd\Gamma + \int_{\Gamma_{\theta}} \frac{dw(x)}{dx} EI_z \frac{d^2v(x)}{dx^2} nd\Gamma \\ &= - \int_{\Gamma_M} \frac{dw(x)}{dx} M_0 d\Gamma \end{aligned} \quad (2.46)$$

Inserting the shear force part of the Neumann boundary conditions (2.40) into the term $\int_{\Gamma} w(x)EI_z \frac{d^3v(x)}{dx^3} nd\Gamma$ and noting that the weight function is equal to zero on Γ_v yields

$$\begin{aligned} \int_{\Gamma} w(x)EI_z \frac{d^3v(x)}{dx^3} nd\Gamma &= \int_{\Gamma_Q} w(x)EI_z \frac{d^3v(x)}{dx^3} nd\Gamma + \int_{\Gamma_v} w(x)EI_z \frac{d^3v(x)}{dx^3} nd\Gamma \\ &= - \int_{\Gamma_Q} w(x)Q_0 d\Gamma \end{aligned} \quad (2.47)$$

2. THREE-DIMENSIONAL LATTICE FRACTURE MODEL

The weak form of the governing equation can be obtained by substituting the equations (2.46) and (2.47) into the equation (2.45). Solving it involves to find a trial function $v(x) \in S$ such that

$$\int_{\Omega} \frac{d^2 w(x)}{dx^2} EI_z \frac{d^2 v(x)}{dx^2} d\Omega + \int_{\Gamma_M} \frac{dw(x)}{dx} M_0 d\Gamma - \int_{\Gamma_Q} w(x) Q_0 d\Gamma - \int_{\Omega} w(x) f_y(x) d\Omega = 0 \quad \forall w(x) \in V \quad (2.48)$$

where S and V are appropriately defined spaces satisfying the following conditions

$$\begin{cases} S = \{v(x) \mid v(x) \in \mathcal{H}^2(\Omega), v(x) = v_0 \text{ on } \Gamma_v, \frac{dv(x)}{dx} = \theta_0 \text{ on } \Gamma_{\theta}\} \\ V = \{w(x) \mid w(x) \in \mathcal{H}^2(\Omega), w(x) = 0 \text{ on } \Gamma_v, \frac{dw(x)}{dx} = 0 \text{ on } \Gamma_{\theta}\} \end{cases} \quad (2.49)$$

Both S and V must be sub-spaces of the Sobolev space $\mathcal{H}^2(\Omega)$, which requires that

$$\begin{cases} \int_{\Omega} \{v^2(x) + \left[\frac{dv(x)}{dx}\right]^2 + \left[\frac{d^2 v(x)}{dx^2}\right]^2\} dx < \infty \\ \int_{\Omega} \{w^2(x) + \left[\frac{dw(x)}{dx}\right]^2 + \left[\frac{d^2 w(x)}{dx^2}\right]^2\} dx < \infty \end{cases} \quad (2.50)$$

Based on the weak form of the governing equation (2.48), a Galerkin problem for the beam can be formulated, which involves to find $v^h(x) \in S^h$ such that

$$\int_{\Omega} \frac{d^2 w^h(x)}{dx^2} EI_z \frac{d^2 v^h(x)}{dx^2} d\Omega = - \int_{\Gamma_M} \frac{dw^h(x)}{dx} M_0 d\Gamma + \int_{\Gamma_Q} w^h(x) Q_0 d\Gamma + \int_{\Omega} w^h(x) f_y(x) d\Omega \quad \forall w^h(x) \in V^h \quad (2.51)$$

where $S^h \subset S$ and $V^h \subset V$ are finite-dimensional spaces.

The Galerkin method (more specifically, the Bubnov-Galerkin method) requires that the trial function and the weight function come from the same finite-dimensional space, taking into account the requirements on the trial and weight functions where Dirichlet boundary conditions are applied.

To find the solution to the Galerkin problem (2.51), Hermitian polynomials can be used to construct the shape functions, which results in a cubic interpolation of the displacement field in the element,

$$v^h(x) = N_i(x)v_i + M_i(x)\theta_i + N_j(x)v_j + M_j(x)\theta_j \quad (2.52)$$

where v_i, θ_i, v_j and θ_j are the translational and rotational displacements at node i and j respectively, and the shape functions are

$$\begin{cases} N_i(x) = 1 - 3\frac{x^2}{l^2} + 2\frac{x^3}{l^3} \\ M_i(x) = x - 2\frac{x^2}{l} + \frac{x^3}{l^2} \\ N_j(x) = 3\frac{x^2}{l^2} - 2\frac{x^3}{l^3} \\ M_j(x) = -\frac{x^2}{l} + \frac{x^3}{l^2} \end{cases} \quad (2.53)$$

Denoting that

$$\underline{N}(x) = [N_i(x) \quad M_i(x) \quad N_j(x) \quad M_j(x)] \quad (2.54)$$

and

$$\underline{a}_e = \begin{Bmatrix} v_i \\ \theta_i \\ v_j \\ \theta_j \end{Bmatrix} \quad (2.55)$$

Thus the displacement field (2.52) can be re-written as

$$v^h(x) = \underline{N}(x)\underline{a}_e \quad (2.56)$$

The second derivative of the trial function $v^h(x)$ is given by

$$\frac{d^2 v^h(x)}{dx^2} = \frac{d^2 \underline{N}(x)}{dx^2} \underline{a}_e \quad (2.57)$$

Similarly the weight function, and its first and second derivatives are given by

$$w^h(x) = \underline{N}(x)\underline{b}_e \quad (2.58)$$

$$\frac{dw^h(x)}{dx} = \frac{d\underline{N}(x)}{dx} \underline{b}_e \quad (2.59)$$

$$\frac{d^2 w^h(x)}{dx^2} = \frac{d^2 \underline{N}(x)}{dx^2} \underline{b}_e \quad (2.60)$$

2. THREE-DIMENSIONAL LATTICE FRACTURE MODEL

Inserting the equations (2.57), (2.58), (2.59) and (2.60) into the Galerkin problem (2.51) yields

$$\begin{aligned} & \int_{\Omega} \left[\frac{d^2 \underline{N}(x)}{dx^2} \underline{b}_e \right]^T EI_z \left[\frac{d^2 \underline{N}(x)}{dx^2} \underline{a}_e \right] d\Omega \\ &= - \int_{\Gamma_M} \left[\frac{d\underline{N}(x)}{dx} \underline{b}_e \right]^T M_0 d\Gamma + \int_{\Gamma_Q} [\underline{N}(x) \underline{b}_e]^T Q_0 d\Gamma + \int_{\Omega} [\underline{N}(x) \underline{b}_e]^T f_y(x) d\Omega \end{aligned} \quad (2.61)$$

Rearranging the above equation yields

$$\begin{aligned} & \int_{\Omega} \left[\frac{d^2 \underline{N}(x)}{dx^2} \right]^T EI_z \left[\frac{d^2 \underline{N}(x)}{dx^2} \right] d\Omega \underline{a}_e \\ &= - \int_{\Gamma_M} \left[\frac{d\underline{N}(x)}{dx} \right]^T M_0 d\Gamma + \int_{\Gamma_Q} [\underline{N}(x)]^T Q_0 d\Gamma + \int_{\Omega} [\underline{N}(x)]^T f_y(x) d\Omega \end{aligned} \quad (2.62)$$

Hence the element stiffness matrix (Euler-Bernoulli beam) for the bending and shear deformation in the plane xOy is given by

$$\begin{aligned} \underline{\underline{K}}_{\text{bExOy}}^e &= \int_{\Omega} \left[\frac{d^2 \underline{N}(x)}{dx^2} \right]^T EI_z \left[\frac{d^2 \underline{N}(x)}{dx^2} \right] d\Omega \\ &= \int_0^l \begin{bmatrix} -\frac{6}{l^2} + \frac{12}{l^3}x \\ -\frac{4}{l} + \frac{6}{l^2}x \\ \frac{6}{l^2} - \frac{12}{l^3}x \\ -\frac{2}{l} + \frac{6}{l^2}x \end{bmatrix} EI_z \left[-\frac{6}{l^2} + \frac{12}{l^3}x \quad -\frac{4}{l} + \frac{6}{l^2}x \quad \frac{6}{l^2} - \frac{12}{l^3}x \quad -\frac{2}{l} + \frac{6}{l^2}x \right] dx \\ &= \begin{bmatrix} \frac{12EI_z}{l^3} & \frac{6EI_z}{l^2} & -\frac{12EI_z}{l^3} & \frac{6EI_z}{l^2} \\ \frac{6EI_z}{l^2} & \frac{4EI_z}{l} & -\frac{6EI_z}{l^2} & \frac{2EI_z}{l} \\ -\frac{12EI_z}{l^3} & -\frac{6EI_z}{l^2} & \frac{12EI_z}{l^3} & -\frac{6EI_z}{l^2} \\ \text{sym.} & & & \frac{4EI_z}{l} \end{bmatrix} \end{aligned} \quad (2.63)$$

The shear deformation and rotational inertia effects can be taken into account (Timoshenko beam) by introducing an adjustment factor Φ into the above element stiffness matrix (2.63), and it is given by

$$\underline{\underline{K}}_{\text{bTxOy}}^e = \begin{bmatrix} \frac{12EI_z}{l^3(1+\Phi_1)} & \frac{6EI_z}{l^2(1+\Phi_1)} & -\frac{12EI_z}{l^3(1+\Phi_1)} & \frac{6EI_z}{l^2(1+\Phi_1)} \\ \frac{(4+\Phi_1)EI_z}{l(1+\Phi_1)} & \frac{(2-\Phi_1)EI_z}{l(1+\Phi_1)} & -\frac{6EI_z}{l^2(1+\Phi_1)} & \frac{6EI_z}{l(1+\Phi_1)} \\ -\frac{12EI_z}{l^3(1+\Phi_1)} & -\frac{6EI_z}{l^2(1+\Phi_1)} & \frac{12EI_z}{l^3(1+\Phi_1)} & -\frac{6EI_z}{l^2(1+\Phi_1)} \\ \text{sym.} & & & \frac{(4+\Phi_1)EI_z}{l(1+\Phi_1)} \end{bmatrix} \quad (2.64)$$

where E is the elastic modulus, I_z is the moment of inertia of the cross-section about the z -axis, l is the length of the element and Φ_1 is the shear effect adjustment factor in the plane xOy .

The element stiffness matrix for the bending and shear deformation in the plane xOz can be formulated in a similar way and is given by

$$\underline{\underline{K}}_{\text{bTxOz}}^e = \begin{bmatrix} \frac{12EI_y}{l^3(1+\Phi_2)} & -\frac{6EI_y}{l^2(1+\Phi_2)} & -\frac{12EI_y}{l^3(1+\Phi_2)} & -\frac{6EI_y}{l^2(1+\Phi_2)} \\ & \frac{(4+\Phi_2)EI_y}{l(1+\Phi_2)} & \frac{6EI_y}{l^2(1+\Phi_2)} & \frac{(2-\Phi_2)EI_y}{l(1+\Phi_2)} \\ & & \frac{12EI_y}{l^3(1+\Phi_2)} & \frac{6EI_y}{l^2(1+\Phi_2)} \\ \text{sym.} & & & \frac{(4+\Phi_2)EI_y}{l(1+\Phi_2)} \end{bmatrix} \quad (2.65)$$

where E is the elastic modulus, I_z is the moment of inertia of the cross-section about the z -axis, l is the length of the element and Φ_1 is the shear effect adjustment factor in the plane xOy .

The element stiffness matrix in local domain for a lattice Timoshenko beam element can be obtained by assembly of the axial (2.26), torsional (2.27), bending and shear components in the plane xOy (2.64) and in the plane xOz (2.65), and it is given by

$$\underline{\underline{K}}_{\text{local}}^e = \begin{bmatrix} \frac{EA}{l} & 0 & 0 & 0 & 0 & 0 & -\frac{EA}{l} & 0 & 0 & 0 & 0 & 0 \\ & \frac{12EI_z}{l^3(1+\Phi_1)} & 0 & 0 & 0 & \frac{6EI_z}{l^2(1+\Phi_1)} & 0 & -\frac{12EI_z}{l^3(1+\Phi_1)} & 0 & 0 & 0 & \frac{6EI_z}{l^2(1+\Phi_1)} \\ & & \frac{12EI_y}{l^3(1+\Phi_2)} & 0 & -\frac{6EI_y}{l^2(1+\Phi_2)} & 0 & 0 & 0 & -\frac{12EI_y}{l^3(1+\Phi_2)} & 0 & -\frac{6EI_y}{l^2(1+\Phi_2)} & 0 \\ & & & \frac{GJ}{l} & 0 & 0 & 0 & 0 & 0 & -\frac{GJ}{l} & 0 & 0 \\ & & & & \frac{(4+\Phi_2)EI_y}{l(1+\Phi_2)} & 0 & 0 & 0 & \frac{6EI_y}{l^2(1+\Phi_2)} & 0 & \frac{(2-\Phi_2)EI_y}{l(1+\Phi_2)} & 0 \\ & & & & & \frac{(4+\Phi_1)EI_z}{l(1+\Phi_1)} & 0 & -\frac{6EI_z}{l^2(1+\Phi_1)} & 0 & 0 & 0 & \frac{(2-\Phi_1)EI_z}{l(1+\Phi_1)} \\ & & & & & & \frac{EA}{l} & 0 & 0 & 0 & 0 & 0 \\ & & & & & & & \frac{12EI_z}{l^3(1+\Phi_1)} & 0 & 0 & 0 & -\frac{6EI_z}{l^2(1+\Phi_1)} \\ & & & & & & & & \frac{12EI_y}{l^3(1+\Phi_2)} & 0 & \frac{6EI_y}{l^2(1+\Phi_2)} & 0 \\ & & & & & & & & & \frac{GJ}{l} & 0 & 0 \\ & & & & & & & & & & \frac{(4+\Phi_2)EI_y}{l(1+\Phi_2)} & 0 \\ \text{sym.} & & & & & & & & & & & \frac{(4+\Phi_1)EI_z}{l(1+\Phi_1)} \end{bmatrix} \quad (2.66)$$

where E is the elastic modulus, G is the shear modulus, A is the cross-sectional area of the element, l is the length of the element, I_z and I_y are the moment of inertia about the z -axis and the y -axis respectively, J is the polar moment of inertia about the x -axis, Φ_1 and Φ_2 are the shear effect adjustment factors in the plane xOy and xOz respectively and can be computed by

$$\begin{cases} \Phi_1 = \frac{12EI_z}{GA_s l^2} \\ \Phi_2 = \frac{12EI_y}{GA_s l^2} \end{cases} \quad (2.67)$$

2. THREE-DIMENSIONAL LATTICE FRACTURE MODEL

in which A_s is the shear cross-sectional area and is given by

$$A_s = \frac{A}{\kappa} \quad (2.68)$$

where κ is the shear correction factor and it is equal to $\frac{10}{9}$ for circular cross-section.

In 3D lattice network construction a circular cross-section of the element is preferred to rectangular one as it gives isotropic geometry properties about the cross-section, and the following formulas apply,

$$\begin{cases} A = \pi r^2 \\ I_z = \frac{\pi}{4} r^4 \\ I_y = \frac{\pi}{4} r^4 \\ J = \frac{\pi}{2} r^4 \end{cases} \quad (2.69)$$

The element stiffness matrix in global domain can be computed by the following formula,

$$\underline{\underline{K}}_{\text{global}}^e = \underline{\underline{T}} \underline{\underline{K}}_{\text{local}}^e \underline{\underline{T}}^T \quad (2.70)$$

where $\underline{\underline{K}}_{\text{local}}^e$ is the element stiffness matrix in local domain as shown in the expression (2.66), $\underline{\underline{T}}$ is the transformation matrix of local and global domains, and $\underline{\underline{T}}^T$ represents the transposed matrix of $\underline{\underline{T}}$.

The local and global domains are illustrated in Figure 2.15 and the local domain $O^*x^*y^*z^*$ is attached to the element. The relationship of the two domains is indicated by the transformation matrix $\underline{\underline{T}}$, which is in the size of 12×12 and in the form of

$$\underline{\underline{T}} = \begin{bmatrix} \underline{\underline{t}} & & & \\ & \underline{\underline{t}} & & \\ & & \underline{\underline{t}} & \\ & & & \underline{\underline{t}} \end{bmatrix} \quad (2.71)$$

where the matrix $\underline{\underline{t}}$ of the size 3×3 is given by

$$\underline{\underline{t}} = \begin{bmatrix} l_1 = \cos(x, x^*) & l_2 = \cos(x, y^*) & l_3 = \cos(x, z^*) \\ m_1 = \cos(y, x^*) & m_2 = \cos(y, y^*) & m_3 = \cos(y, z^*) \\ n_1 = \cos(z, x^*) & n_2 = \cos(z, y^*) & n_3 = \cos(z, z^*) \end{bmatrix} \quad (2.72)$$

in which nine direction cosines are defined.

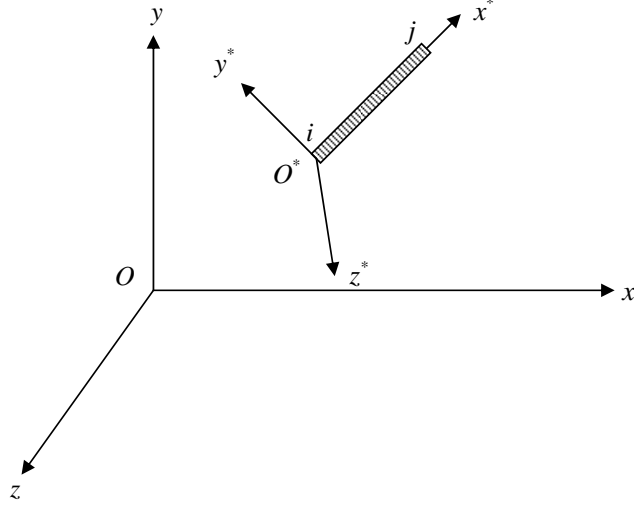


Figure 2.15: Local and global domains

Procedure. The nine direction cosines can be determined based on the coordinates of the two nodes $i(x_i, y_i, z_i)$ and $j(x_j, y_j, z_j)$ in global domain. The procedure is

(1) calculate a_1 , a_2 and a_3 according to

$$\begin{cases} a_1 = x_j - x_i \\ a_2 = y_j - y_i \\ a_3 = z_j - z_i \end{cases} \quad (2.73)$$

(2) choose an arbitrary reference point $B(x_b, y_b, z_b)$ on the principal plane $x^*O^*y^*$ or $x^*O^*z^*$, provided that the point B is not located at the x^* -axis, and then compute b_1 , b_2 and b_3 according to

$$\begin{cases} b_1 = x_b - x_i \\ b_2 = y_b - y_i \\ b_3 = z_b - z_i \end{cases} \quad (2.74)$$

(3) calculate c_1 , c_2 and c_3 using the following formulas,

$$\begin{cases} c_1 = a_2b_3 - a_3b_2 \\ c_2 = a_3b_1 - a_1b_3 \\ c_3 = a_1b_2 - a_2b_1 \end{cases} \quad (2.75)$$

2. THREE-DIMENSIONAL LATTICE FRACTURE MODEL

(4) compute d_1 , d_2 and d_3 according to

$$\begin{cases} d_1 = c_2 a_3 - c_3 a_2 \\ d_2 = c_3 a_1 - c_1 a_3 \\ d_3 = c_1 a_2 - c_2 a_1 \end{cases} \quad (2.76)$$

(5) calculate the length of the element $l = \sqrt{a_1^2 + a_2^2 + a_3^2}$, and then l_1 , m_1 and n_1 can be obtained,

$$\begin{cases} l_1 = \frac{a_1}{l} \\ m_1 = \frac{a_2}{l} \\ n_1 = \frac{a_3}{l} \end{cases} \quad (2.77)$$

(6) compute the expression $d = \sqrt{d_1^2 + d_2^2 + d_3^2}$, and then l_2 , m_2 and n_2 can be obtained,

$$\begin{cases} l_2 = \frac{d_1}{d} \\ m_2 = \frac{d_2}{d} \\ n_2 = \frac{d_3}{d} \end{cases} \quad (2.78)$$

(7) finally l_3 , m_3 and n_3 can be computed according to

$$\begin{cases} l_3 = m_1 n_2 - m_2 n_1 \\ m_3 = n_1 l_2 - n_2 l_1 \\ n_3 = l_1 m_2 - l_2 m_1 \end{cases} \quad (2.79)$$

□

Jacobi pre-conditioned conjugate gradient linear equations solver

A set of linear equations are formulated and solved during the lattice fracture analysis, and the Jacobi pre-conditioned conjugate gradient method [30] is employed. The basic algorithm is presented as following.

Algorithm. Suppose that a system of linear equations is represented by

$$Ax = b \quad (2.80)$$

where A is the coefficient matrix, b is the constant vector, x is the solution vector.

Given the inputs A , b , an initial guess of x , absolute error tolerance $\epsilon_a < 1$, relative error tolerance $\epsilon_r < 1$, and a maximum number of iterations i_{\max} .

$$\begin{aligned} m &\leftarrow \text{diag}(A) \\ m &\leftarrow m^{-1} \\ r &\leftarrow b - Ax \\ d &\leftarrow m. * r \\ \delta_{\text{new}} &\leftarrow r^T d \\ \delta_0 &\leftarrow \delta_{\text{new}} \end{aligned}$$

if $\delta_0 < \epsilon_a^2$, then terminate;

for (int $i = 1$; $i \leq i_{\max}$; $i++$)

{

$$\begin{aligned} q &\leftarrow Ad \\ \alpha &\leftarrow \frac{\delta_{\text{new}}}{d^T q} \\ x &\leftarrow x + \alpha d \\ r &\leftarrow r - \alpha q \\ s &\leftarrow m. * r \\ \delta_{\text{old}} &\leftarrow \delta_{\text{new}} \\ \delta_{\text{new}} &\leftarrow r^T s \end{aligned}$$

if $\delta_{\text{new}} < \epsilon_a^2$ or $\delta_{\text{new}} < \epsilon_r^2 \delta_0$, then terminate;

$$\begin{aligned} \beta &\leftarrow \frac{\delta_{\text{new}}}{\delta_{\text{old}}} \\ d &\leftarrow s + \beta d \end{aligned}$$

}

□

Fracture law

The most frequently used fracture law in lattice fracture model is the classic Rankine failure criterion, which requires the comparative stress in the lattice beam element is smaller than its strength. Other fracture laws are also possible, and see [21] for more discussions. The comparative stress defined in this thesis is caused by the normal force and bending moments, and can be computed by

$$\sigma = \alpha_N \frac{N}{A} + \alpha_M \frac{\max(M_{xOy}, M_{xOz})}{W} \quad (2.81)$$

2. THREE-DIMENSIONAL LATTICE FRACTURE MODEL

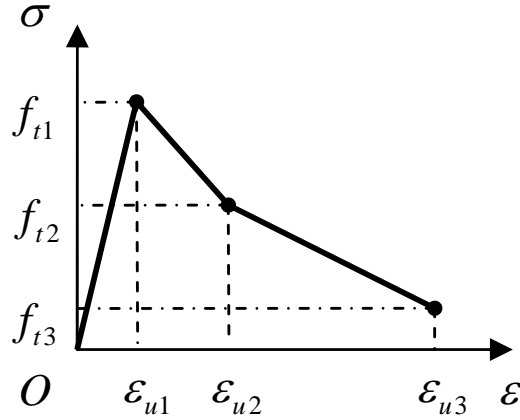


Figure 2.16: Multi-linear constitutive law of lattice elements

where A is the area of the cross-section, W is the cross-sectional factor for bending resistance, α_N and α_M are the normal force influence factor and the bending influence factor whose values are 1.0 and 0.05 respectively in this thesis.

Lattice element removal mechanisms

The basic removal procedure is to remove one element at one lattice analysis step. To speed up the analysis, it is also possible to remove multiple elements at one analysis step. Alternatively the bending resistance of an element may be removed first and then the axial resistance. In the case of local softening implemented, as shown in Figure 2.16, the element loses its stiffness and strength gradually and eventually quits from the system through several analysis steps.

2.2.4 Load-displacement response and cracks propagation

The major outputs of lattice fracture analysis include the load-displacement response, microcracks propagation and cracks pattern in the final failure state. The load-displacement response can be converted to stress-strain diagram, which represents the constitutive relation of the material analyzed. The cracks are represented by the broken lattice elements. As the broken lattice elements are removed step by step during the analysis, the sequence of the removal is traced, which simulates the microcracks propagation. At the end of the lattice fracture

analysis, all the broken lattice elements form the cracks pattern in the final failure state. An application of the 3D lattice fracture model is given in Section 3.1 on Page 70, which is about the micromechanical modeling of cement paste.

2.3 Summary

In this chapter the development of some fracture models (such as discrete cracking model, smeared cracking model and lattice fracture model) for brittle materials were reviewed. The 3D lattice fracture model is implemented for parallel computing on shared memory architecture computers, which enables the study on large systems within a relatively short computing time.

The modeling procedures of 3D lattice fracture model are discussed in detail. The lattice network may be constructed according to ImgLat scheme and/or HymLat scheme, depending on whether the input microstructure of materials is described in terms of voxels or spheres. The influences of mesh randomness and random seed are investigated through a uniaxial tensile test on a prism of the size $40\text{ mm} \times 40\text{ mm} \times 60\text{ mm}$. The local mechanical properties determination principles for lattice elements are developed for ImgLat and HymLat schemes respectively.

The lattice fracture model can be configured to simulate various laboratory tests such as tensile test, shear test, bending test and more. The uniaxial tensile test is illustrated in detail and two types of boundary conditions are distinguished and compared: glued and clamped boundaries. It turns out that the influences of different boundaries on the tensile behavior of materials can be neglected, provided that the Poisson's ratio of the specimen is close to 0, otherwise the influences are significant.

The fracture process simulation is the kernel part of the lattice fracture analysis. The critical lattice elements are removed from the system step by step, representing the propagation of microcracks. The lattice element fracture law and removal mechanisms are also discussed. The load-displacement response of the specimen in question can be obtained from lattice fracture analysis, and it

2. THREE-DIMENSIONAL LATTICE FRACTURE MODEL

can be converted to stress-strain diagram, based on which some mechanical properties such as Young's modulus, strength and fracture energy can be computed. The cracks pattern and microcracks propagation can also be obtained.

The 3D lattice fracture model described in this chapter is applied to simulate the fracture processes in cement paste at microscale in Chapter 3, and the fracture processes in mortar and concrete at mesoscale in Chapter 5.

Chapter 3

Cement Paste at Microscale

The microstructure of materials determines its global performance. This fundamental principle of materials science is adapted in this chapter to predict the mechanical performance of cement paste.

The microstructure of cement paste can be imaged either experimentally or numerically. The micro X-ray computed tomography (CT) [31] offers a non-destructive experimental technique to collect microstructure information of cement paste in terms of digitized voxels. Computer modeling packages are also available to simulate the cement hydration and microstructure formation processes, for instance, the HYMOSTRUC3D model developed by TU Delft [4, 32], the NIST CEMHYD3D toolkit [33] and the Mic model by EPFL [34]. Subsection 3.1.1 talks about simulations of microstructures of cement paste using the HYMOSTRUC3D model, and Subsection 3.1.3 introduces a microstructure of cement paste obtained through CT scan.

After obtaining the microstructure of cement paste, the 3D lattice fracture model can be employed to simulate the fracture behavior of the cement paste. For example, a uniaxial tensile test can be set up and simulated on the cement paste to predict its Young's modulus, tensile strength and fracture energy, as well as the microcracks propagation and cracks pattern in the final failure state. It will be elaborated in Subsection 3.1.2.

The cement hydration and microstructure formation model, HYMOSTRUC3D model, and the mechanical performance evaluation model, 3D lattice fracture

3. CEMENT PASTE AT MICROSCALE

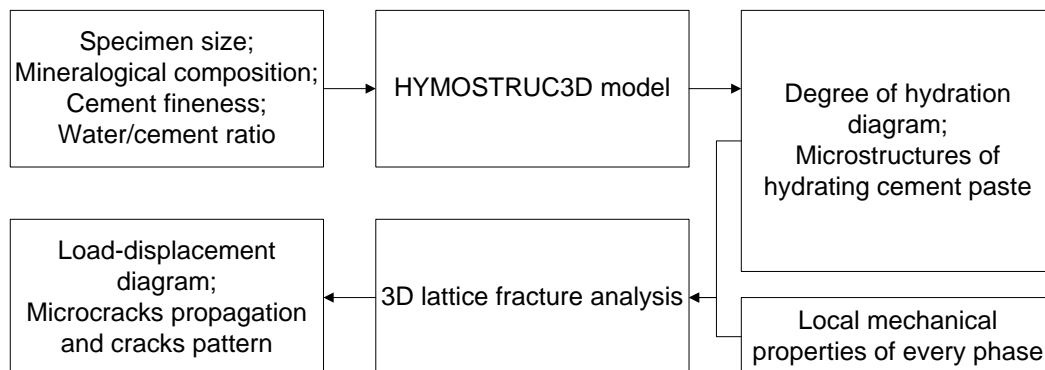


Figure 3.1: Combined application of the HYMOSTRUC3D model and the 3D lattice fracture model

model, can be combined to study the influences of various factors on the mechanical properties of cement paste, including but not limited to the influences of degree of hydration, cement fineness, water/cement ratio and mineral composition of cement. Details and findings can be found in Section 3.2.

3.1 Micromechanical modeling of cement paste

In Subsection 3.1.1 and 3.1.2, a numerical experiment is carried out to illustrate the combined application of the HYMOSTRUC3D model and the 3D lattice fracture model. A series of microstructures are simulated for the cement paste at different degrees of hydration by the HYMOSTRUC3D model, and then the mechanical performance of the microstructure at the curing age of 28 days is evaluated through the 3D lattice fracture analysis. The workflow is shown in Figure 3.1.

In Subsection 3.1.3, an alternative method to obtain the microstructure of cement paste is introduced, which is the micro X-ray computed tomography [35]. A sample microstructure at the curing age of 28 days is scanned and provided by the researchers at UIUC (University of Illinois at Urbana-Champaign, United States) [36], and then it is tested for its uniaxial tensile properties using the 3D lattice fracture model [37]. This example demonstrates that the 3D lattice

3.1 Micromechanical modeling of cement paste

fracture analysis can accept microstructures of cement paste from laboratory experiments, in addition to the computer simulated microstructures.

3.1.1 Simulated microstructures of cement paste

The clinker of Portland cement is mainly composed of calcium, silicon and oxygen. In cement chemistry it is usually represented in terms of constituents as tricalcium silicate $3CaO \cdot SiO_2$ (C_3S), dicalcium silicate $2CaO \cdot SiO_2$ (C_2S), tricalcium aluminate $3CaO \cdot Al_2O_3$ (C_3A) and calcium ferroaluminate $4CaO \cdot Al_2O_3 \cdot Fe_2O_3$ (C_4AF). A set of chemical reactions is initiated when water is mixed with cement, the process of which is called hydration. The hydration process is always accompanied by heat release as the energy state of cement mixture turns from higher one to lower one. The heat release indicates the degree of hydration and it can be used as a measurement to determine the extent of hydration. The hydration products are also generated during the hydration process, which mainly include calcium silicate hydrates (CSH) and calcium hydroxides (CH).

In the HYMOSTRUC3D model, the cement particles are modeled as spheres and these spherical particles grow during the hydration process. The inputs include the specimen size, the mineralogical composition of cement, the cement fineness in terms of Blaine value (Rosin-Rammler particle size distribution is assumed) and the water/cement ratio. The amount of hydration products is dependent on the degree of hydration. A simplification is made in the model that the amount of CH product is substituted with the same amount of CSH product. In general the hydrating cement particle contains three layers from center to outward surface, namely unhydrated cement, inner product and outer product, as shown in Figure 3.2.

The cement grain dissolves and the hydration products are generated gradually during the hydration process, which yields expansion and layer thickness change of the cement particle, as shown in Figure 3.2. The amount of unhydrated cement is decreasing, while inner product and outer product are being produced.

The interactions between neighboring particles are taken into account in the HYMOSTRUC3D model. If the outer product of one hydrating cement particle

3. CEMENT PASTE AT MICROSCALE

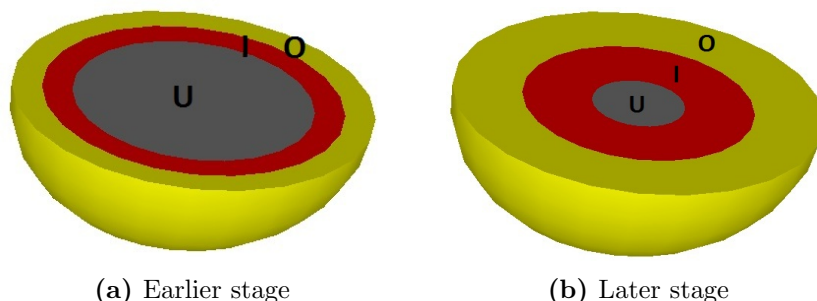


Figure 3.2: Hydration of a single cement particle



Figure 3.3: Contact of hydrating cement particles

meets the outer product of another particle, then the overlapping part is redistributed to the outer layer of the particles. As a result contact volume and area can be formed as shown in Figure 3.3. In [38] it is found that the mechanical properties (such as Young's modulus, shear modulus and compressive strength) of cement paste can be related to the contact area.

An example is given to demonstrate the application of the HYMOSTRUC3D model. The cement CEM I 42.5N is used, and the specification of the cement mix is summarized in Table 3.1. The initial microstructure of cement paste can be created by parking multiple spherical particles into an empty container, as shown in Figure 3.4(a). The simulated degree of hydration diagram is given in Figure 3.5, on which each point corresponds to a microstructure. The microstructures at the curing ages of 28 days and 365 days are shown in Figure 3.4(b) and 3.4(c) respectively, the corresponding degrees of hydration are 69 % and 88 %. Periodic material boundary conditions apply.

3.1 Micromechanical modeling of cement paste

Table 3.1: Specification of the cement mix used in the simulation

Cement type	CEM I 42.5N
Mineralogical composition	C_3S : 64 %, C_2S : 13 %, C_3A : 8 %, C_4AF : 9 %
Fineness (Blaine value)	420 m ² /kg
Minimum particle diameter	1 μm
Maximum particle diameter	37 μm
Particle size distribution	Rosin-Rammler distribution $F(x) = 1 - e^{-bx^n}$ ($n = 1.0698$, $b = 0.04408$)
Specimen size	100 μm × 100 μm × 100 μm
Water/cement ratio	0.4
Curing temperature	20 °C

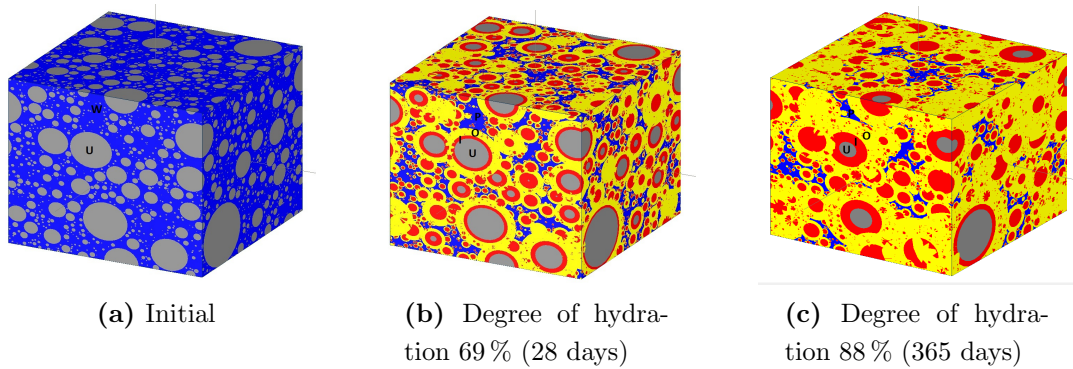


Figure 3.4: Microstructures of cement paste at different degrees of hydration with the specification in Table 3.1

3. CEMENT PASTE AT MICROSCALE

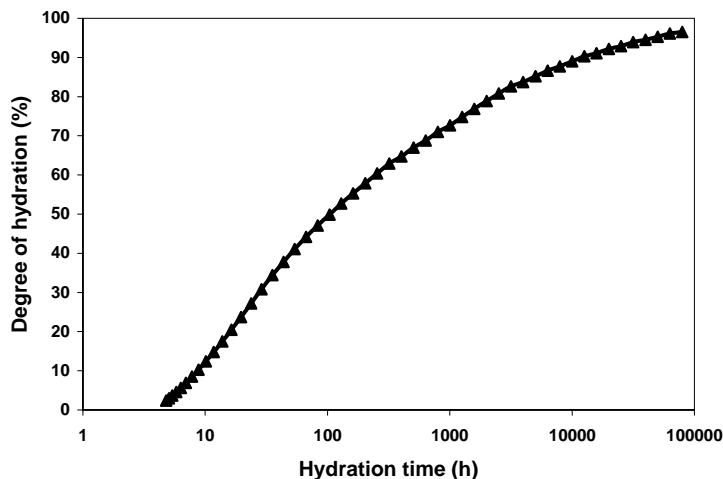


Figure 3.5: Simulated degree of hydration diagram against hydration time

The cement paste of curing age 28 days is usually of interest, as the strength at 28 days is commonly used in many structural design codes, hence the microstructure in Figure 3.4(b) is further analyzed after it is converted to a voxel-based digital image, as shown in Figure 3.6. It can be decomposed to four phases, including a pore phase shown in Figure 3.7(a), and three solid phases namely unhydrated cement shown in Figure 3.7(b), inner product in Figure 3.7(c) and outer product in Figure 3.7(d). The volume percentage of every individual phase is indicated in the subcaptions in Figure 3.7.

3.1.2 Mechanical performance evaluation of the microstructures

Having obtained the microstructure of cement paste, the next step is to evaluate its mechanical performance using the 3D lattice fracture model. It is required to convert the spherical particle embedded microstructure to a voxel-based digital image, where the ImgLat lattice construction method applies, as discussed in Subsection 2.2.1 on Page 35. The microstructure of cement paste in Figure 3.6 is taken for the mechanical performance evaluation. The water/cement ratio is 0.4, the degree of hydration is 69% and the porosity is 13%.

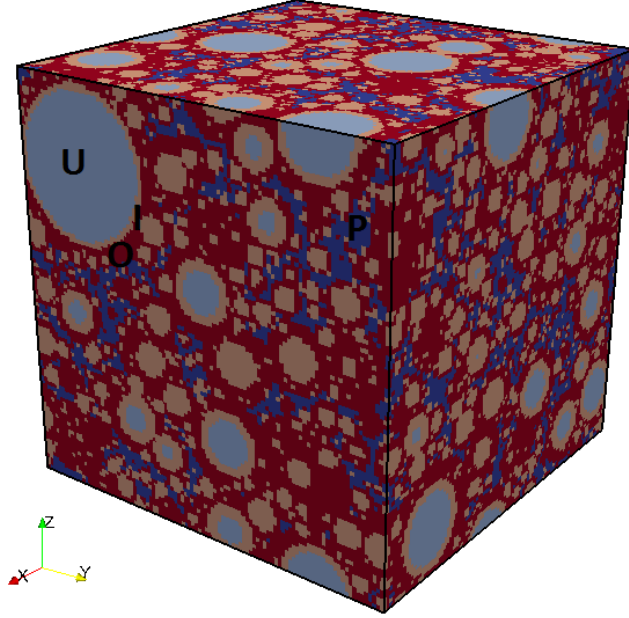


Figure 3.6: Voxel-based image of the microstructure of cement paste in Figure 3.4(b) ($100\ \mu\text{m} \times 100\ \mu\text{m} \times 100\ \mu\text{m}$)

The specimen of the size $100\ \mu\text{m} \times 100\ \mu\text{m} \times 100\ \mu\text{m}$ is meshed at the resolution $1\ \mu\text{m}/\text{voxel}$, and a quadrangular lattice network is constructed. The randomness of the lattice system is set to 0 for all the boundary cells and 0.5 for other cells. This configuration would yield a realistic crack pattern and a regular specimen shape. The influence of randomness on the simulated mechanical performance is studied in Subsection 2.2.1 and the results are summarized in Table 2.4. The cross-section of a lattice element is assumed to be circular, and its area is equal to the perpendicular voxel surface area which is $1\ \mu\text{m}^2$ in this example. The elastic properties of solid phases can be measured or simulated as presented in [39, 40], the values of which are scattered due to different measurement approaches used. The tensile strength ratio of each phase is considered equal to the nanoindentation hardness ratio. The assumed local mechanical properties of individual solid phases are given in Table 3.2. More discussions about the local mechanical properties can be found in [41].

The assignment of local mechanical properties to a lattice element is related to the type of the lattice element in question, which is determined by the locations

3. CEMENT PASTE AT MICROSCALE

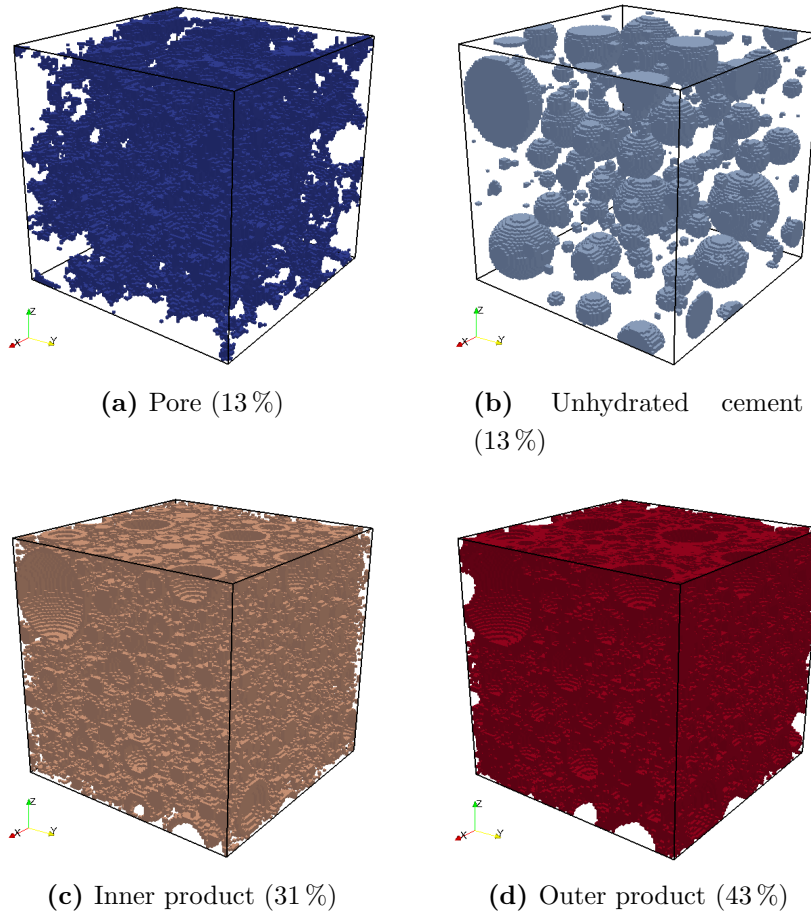


Figure 3.7: Individual phases of the microstructure of cement paste in Figure 3.6

Table 3.2: Assumed local mechanical properties of solid phases of cement paste

No	Solid phase	Young's modulus E (GPa)	Shear modulus G (GPa)	Tensile strength f_t (GPa)
1	Unhydrated cement	135	52	1.8
2	Inner product	30	12	0.24
3	Outer product	22	8.9	0.15

3.1 Micromechanical modeling of cement paste

Table 3.3: Classification of lattice element types

No	Element type	Node 1 phase	Node 2 phase
1	Unhydrated cement	Unhydrated cement	Unhydrated cement
2	Inner product	Inner product	Inner product
3	Outer product	Outer product	Outer product
4	Interface U-I	Unhydrated cement	Inner product
5	Interface I-O	Inner product	Outer product
6	Interface O-U	Outer product	Unhydrated cement

Table 3.4: Local mechanical properties of lattice elements

No	Element type	Young's modulus E (GPa)	Shear modulus G (GPa)	Tensile strength f_t (GPa)
1	Unhydrated cement	135	52	1.8
2	Inner product	30	12	0.24
3	Outer product	22	8.9	0.15
4	Interface U-I	49	20	0.24
5	Interface I-O	25	10	0.15
6	Interface O-U	38	15	0.15

of its two nodes, as shown in Figure 2.7. Three solid phases in the microstructure result in six types of lattice elements, as listed in Table 3.3. No lattice node is generated in the voxels which represent pore phase, as it does not contribute to the global mechanical performance of the specimen.

The local mechanical properties of lattice elements are determined according to the rules laid down in Subsection 2.2.1 on Page 41. All lattice elements behave linear-brittle, and the Young's modulus, shear modulus and tensile strength are given in Table 3.4.

A conventional uniaxial tensile test is simulated on the lattice system, the external load is imposed on the top and bottom surfaces in the z -direction, and all the other surfaces are free to expand and/or shrink as shown in Figure 3.8.

The fracture process is simulated by the removal of lattice elements step by

3. CEMENT PASTE AT MICROSCALE

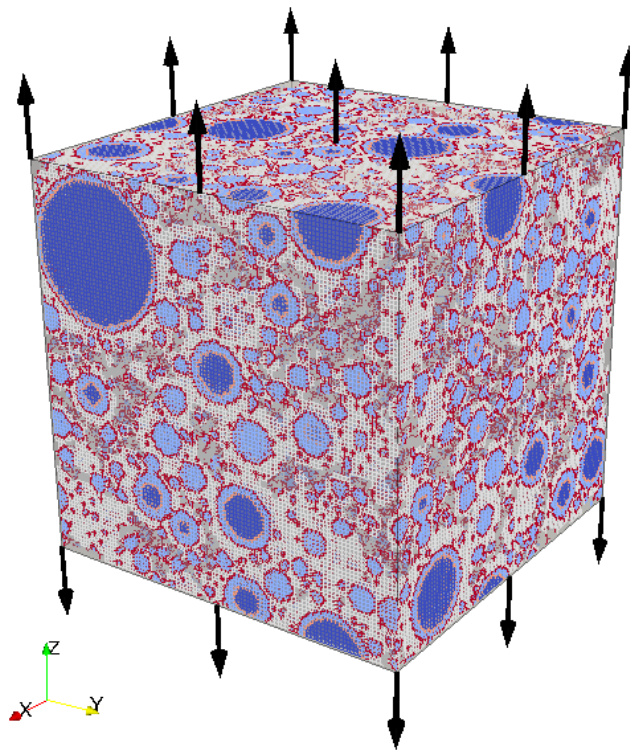


Figure 3.8: Uniaxial tensile test on lattice system of cement paste at microscale

3.1 Micromechanical modeling of cement paste

Table 3.5: Simulated mechanical properties of cement paste at microscale, corresponding with Figure 3.9

Young's modulus E (GPa)	Tensile strength f_t (MPa)	Strain at peak load ϵ_p	Fracture energy G_F (J/m ²)
13	20	0.18 %	22

step. The basic idea of lattice fracture analysis is that imposing a prescribed displacement on the lattice structure, finding the critical element that has highest stress/strength ratio, and then removing it from the system. This procedure is repeated until the system fails. The final outcomes of the simulation include the load-displacement diagram which can be converted to a stress-strain diagram, as shown in Figure 3.9, and the microcracks propagation as shown in Figure 3.10.

The stress-strain diagram reveals the tensile behavior of cement paste at microscale, from which the elastic modulus, tensile strength, strain at peak load and fracture energy can be obtained. For the example given hereby, the simulated mechanical properties of cement paste at microscale are given in Table 3.5. The Young's modulus is the slope of the curve at the linear stage in the stress-strain diagram in Figure 3.9, the tensile strength corresponds to the peak point, and the fracture energy can be computed as the area below the stress-strain curve. The absolute values of global tensile strength and the strain at peak load are linearly dependent on the local input strength listed in Table 3.4. If all the local strengths would be doubled, then the resulting global tensile strength and the strain at peak load would also be doubled, and the fracture energy would be four times larger as it is related to the square of the local strength values.

Figure 3.10 shows that first a few microcracks are initiated around the middle part of the specimen, and then the microcracks spread further until the final failure state. In total 38 106 lattice analysis steps are performed, which means 38 106 lattice elements are broken and thus removed from the system, as all elements behave linear-brittle locally. The pre-peak and post-peak microcracks are also shown in Figure 3.10. The deformed specimen in the final failure state is shown in Figure 3.11.

3. CEMENT PASTE AT MICROSCALE

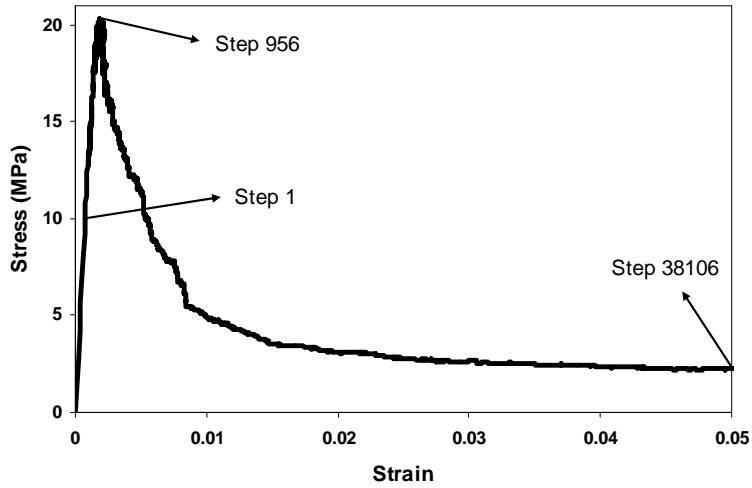


Figure 3.9: Simulated stress-strain diagram of cement paste at microscale

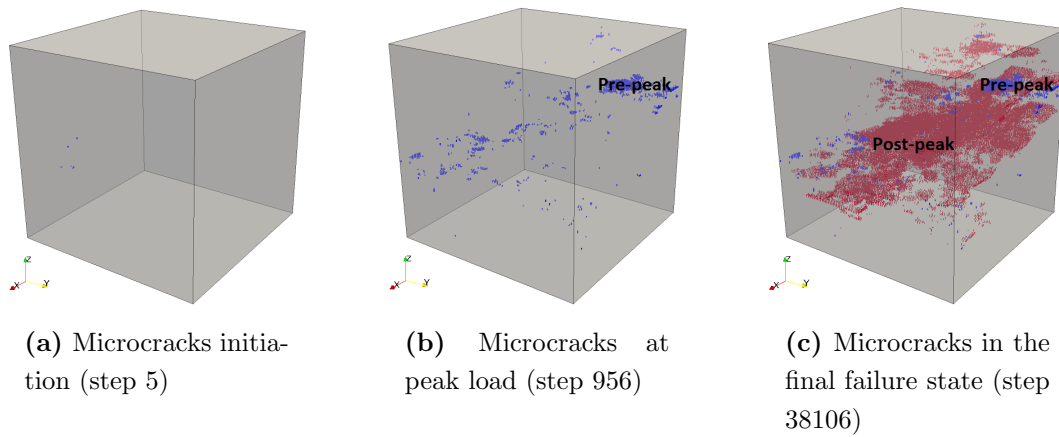


Figure 3.10: 3D microcracks propagation of cement paste due to tension at microscale, corresponding with Figure 3.9

3.1 Micromechanical modeling of cement paste

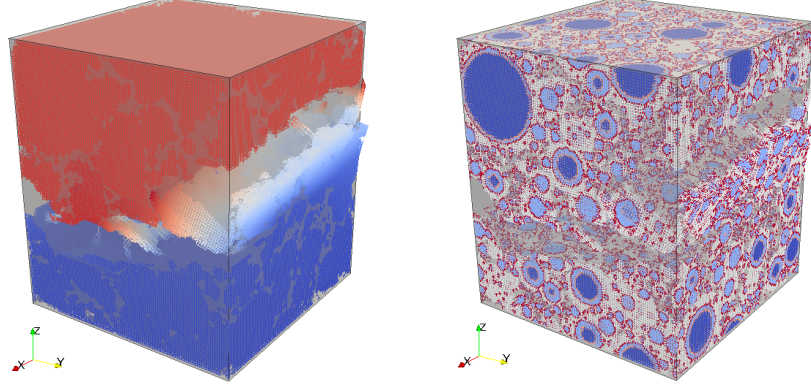


Figure 3.11: Deformed specimen due to vertical tension in the final failure state, corresponding with Figure 3.9

Table 3.6: Simulated mechanical properties of cement paste at microscale, loaded horizontally along x -direction or y -direction, and vertically along z -direction

Loading direction	Young's modulus E (GPa)	Tensile strength f_t (MPa)	Strain at peak load ϵ_p	Fracture energy G_F (J/m ²)
x -axis	13	21	0.18 %	17
y -axis	13	21	0.21 %	20
z -axis	13	20	0.18 %	22

Influences of loading directions

The external tensile load is imposed along the vertical z -direction in Figure 3.8, alternatively the specimen can also be loaded horizontally along x -direction or y -direction. The simulated mechanical properties are not necessary to be exactly the same, as summarized in Table 3.6, due to the fact that the cement paste is not ideal isotropic homogeneous. The stress-strain responses are given in Figure 3.12 and the cracks patterns are shown in Figure 3.13.

Comparisons can be made based on Table 3.6 and Figure 3.12 to learn the influences of loading directions on the simulated stress-strain response. It is apparent that differences exist but not too much. The cracks patterns in the final failure state also have some differences, as shown in Figure 3.13.

3. CEMENT PASTE AT MICROSCALE

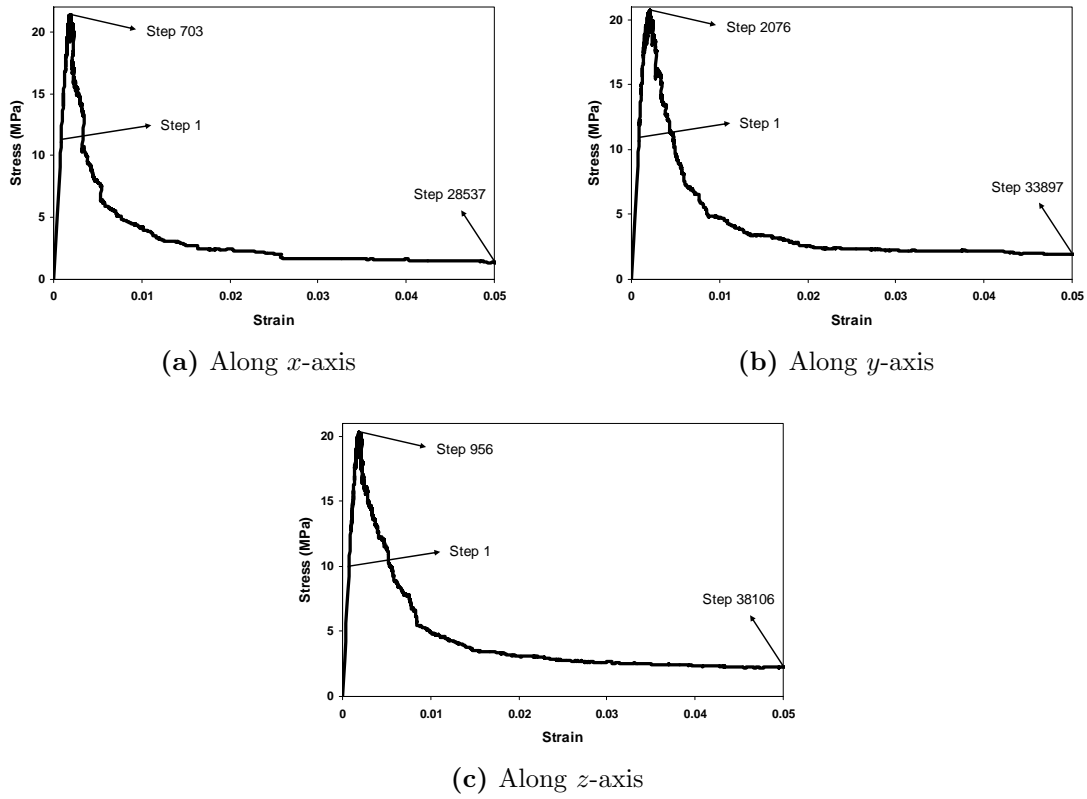


Figure 3.12: Simulated stress-strain diagrams of cement paste at microscale, loaded horizontally along x -direction or y -direction, and vertically along z -direction

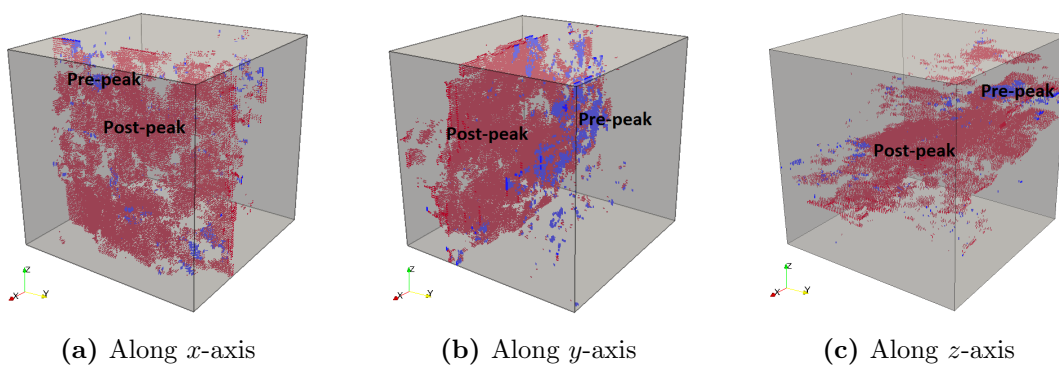


Figure 3.13: Cracks patterns in the final failure state, loaded horizontally along x -direction or y -direction, and vertically along z -direction

3.1 Micromechanical modeling of cement paste

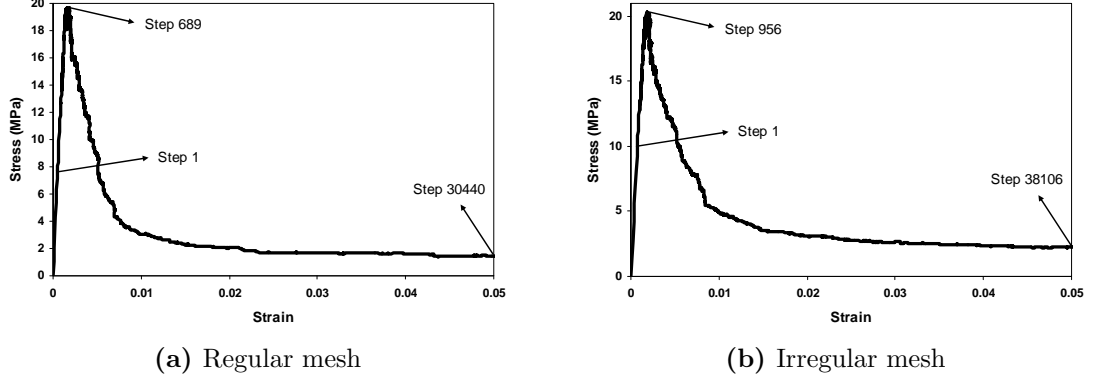


Figure 3.14: Simulated stress-strain diagrams of cement paste with regular lattice mesh, and irregular lattice mesh at the randomness of 0.5

Regular lattice mesh

During the construction of the lattice network, the randomness is set to 0 for all the boundary cells and 0.5 for other cells in the previous examples in this chapter. A regular mesh can be made by setting the randomness to 0 for all cells. The simulated tensile mechanical response is shown in Figure 3.14. Some mechanical properties can be computed based on this diagram, as listed in Table 3.7.

Comparisons can be made based on Figure 3.14 and Table 3.7 to see the influences of randomness on the simulated mechanical properties. Adopting an irregular mesh introduces artificial heterogeneity and thus makes the simulated Young's modulus lower. This finding is in accordance with the trend found in Table 2.4, which studies the influences of randomness using a homogeneous prism. The pre-peak and post-peak microcracks are shown in Figure 3.15 for the regular meshed lattice system and the irregular meshed lattice system at the randomness of 0.5.

3.1.3 CT-scanned microstructures and its micromechanical properties

A lattice network can be constructed based on a microstructure simulated by a computer modeling package, as shown in the examples in Subsection 3.1.1 and

3. CEMENT PASTE AT MICROSCALE

Table 3.7: Simulated mechanical properties of cement paste with regular lattice mesh at the randomness of 0, and with irregular lattice mesh at the randomness of 0.5

Mesh	Young's modulus E (GPa)	Tensile strength f_t (MPa)	Strain at peak load ϵ_p	Fracture energy G_F (J/m ²)
Regular	14	20	0.15 %	16
Irregular	13	20	0.18 %	22

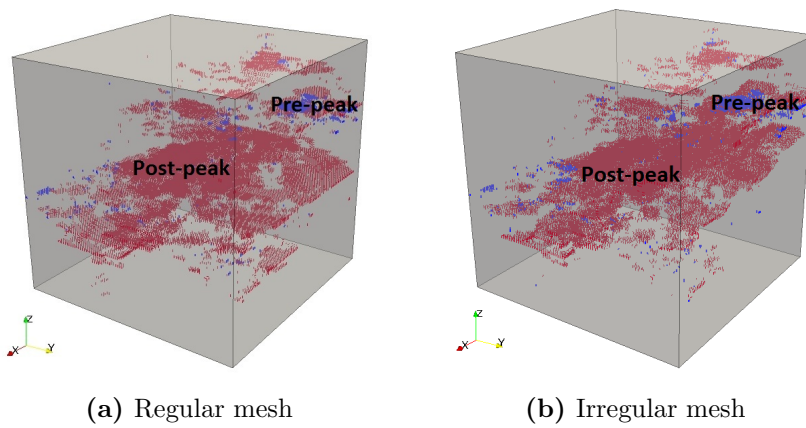


Figure 3.15: Pre-peak and post-peak microcracks for the regular meshed lattice system, and the irregular meshed lattice system at the randomness of 0.5

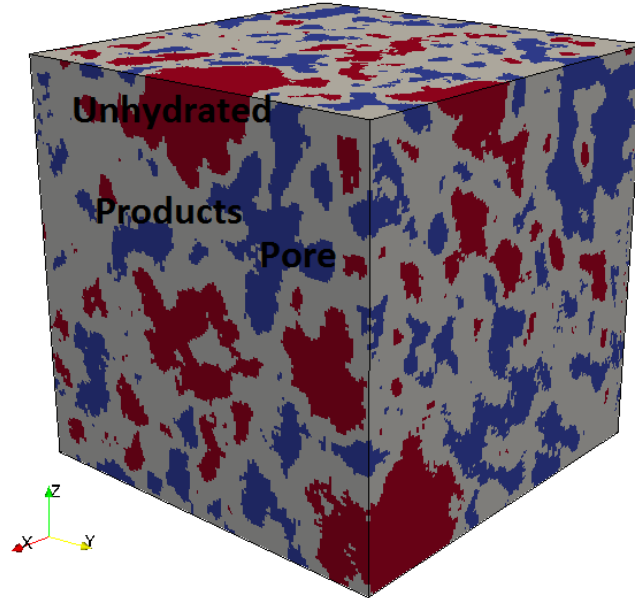


Figure 3.16: Microstructure of cement paste of size $75\ \mu\text{m} \times 75\ \mu\text{m} \times 75\ \mu\text{m}$ at the curing age 28 days with water/cement ratio 0.5 from CT scan (provided by UIUC)

Subsection 3.1.2. Alternatively the microstructure can also be obtained through laboratory experimental method like CT scan. A microstructure of real cement paste is given in Figure 3.16, which is taken from an X-ray tomograph of a real cement paste sample captured using a micro X-ray CT system located at UIUC (University of Illinois at Urbana-Champaign, US). The water/cement ratio of the paste is 0.5, the curing age is 28 days and the size of the specimen is $75\ \mu\text{m} \times 75\ \mu\text{m} \times 75\ \mu\text{m}$. The resolution of the digital image in Figure 3.16 is $0.5\ \mu\text{m}/\text{voxel}$, resulting in 150 voxels per direction.

In the microstructure shown in Figure 3.16, three phases are distinguished, including the pore phase and two solid phases, namely unhydrated cement and hydration products [36]. The phase segmentation is carried out on the microstructure and the result is given in Figure 3.17.

The local mechanical properties of individual solid phases are given in Table 3.8, which are derived from the properties in Table 3.2. Two solid phases result in three types of lattice elements, as listed in Table 3.9. The tensile strength

3. CEMENT PASTE AT MICROSCALE

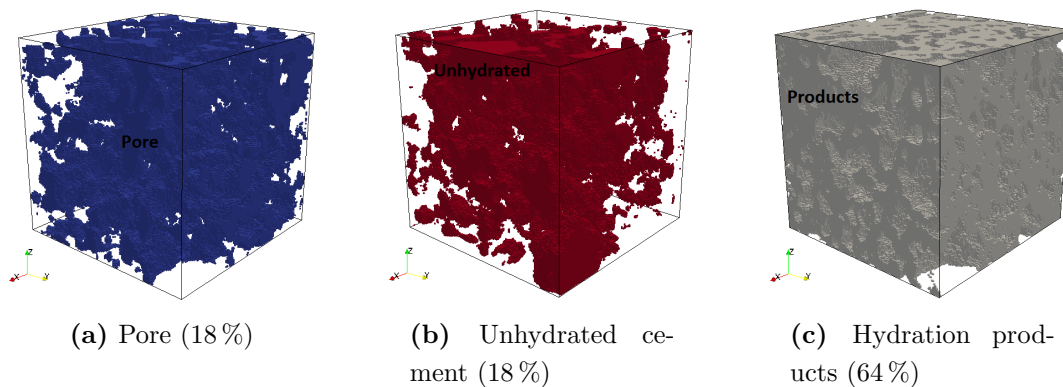


Figure 3.17: Phase segmentation of the microstructure of cement paste in Figure 3.16

Table 3.8: Local mechanical properties of solid phases of experimental cement paste

No	Solid phase	Young's modulus E (GPa)	Shear modulus G (GPa)	Tensile strength f_t (GPa)
1	Hydration products	26	10	0.2
2	Unhydrated cement	135	52	1.8

ratio of hydration products to unhydrated cement is 1:9, which is equal to the measured nanoindentation hardness ratio.

A uniaxial tensile test is simulated on the experimental microstructure, and the stress-strain response is shown in Figure 3.18. Some mechanical properties are computed and summarized in Table 3.10. The cracks pattern in the final failure state is given in Figure 3.19.

3.2 Influences of various factors

The combination of the HYMOSTRUC3D model and 3D lattice fracture analysis makes it possible to investigate the influences of various factors on the global mechanical performance of cement paste at microscale, including but not limited to the degree of hydration, cement fineness, water/cement ratio and mineral

3.2 Influences of various factors

Table 3.9: Local mechanical properties of lattice elements for experimental cement paste

No	Element type	Young's modulus E (GPa)	Shear modulus G (GPa)	Tensile strength f_t (GPa)
1	Hydration products	26	10	0.2
2	Unhydrated cement	135	52	1.8
3	Interface	44	17	0.2

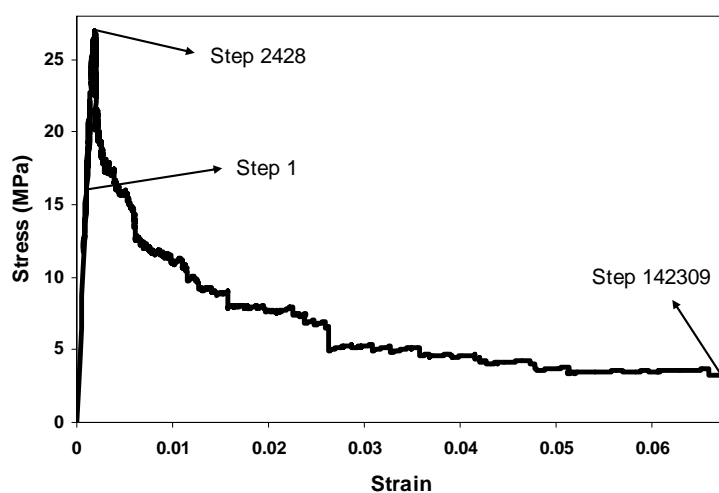


Figure 3.18: Simulated stress-strain diagram of the experimental cement paste at microscale

Table 3.10: Simulated mechanical properties of the experimental cement paste at microscale, corresponding with Figure 3.18

Young's modulus E (GPa)	Tensile strength f_t (MPa)	Strain at peak load ϵ_p	Fracture energy G_F (J/m ²)
16	27	0.19%	34

3. CEMENT PASTE AT MICROSCALE

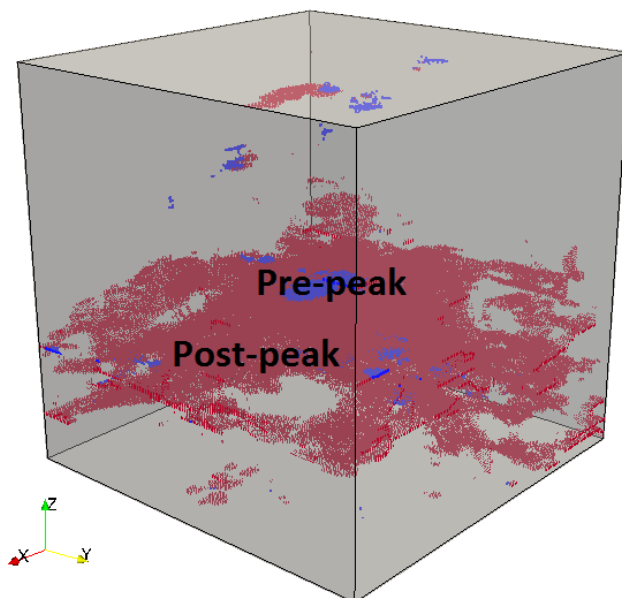


Figure 3.19: Simulated cracks pattern in the final failure state for the experimental cement paste at microscale, corresponding with Figure 3.18

composition of cement. Numerical experiments are carried out to simulate the microstructure and the corresponding tensile properties of the cement paste samples of the size $100\ \mu\text{m} \times 100\ \mu\text{m} \times 100\ \mu\text{m}$. The starting point is the cement mixture and the resulting outcomes are the Young's modulus, tensile strength, fracture energy and cracks pattern, as shown in Figure 3.1.

3.2.1 Degree of hydration

For the cement mixture given in Table 3.1, the HYMOSTRUC3D model is employed to simulate the initial microstructure and a set of microstructures at various degrees of hydration. The resulting degree of hydration curve is shown in Figure 3.5. The following curing ages and degrees of hydration are chosen for further mechanical performance evaluation, as given in Table 3.11. The corresponding microstructures are simulated and analyzed, and the results are summarized in Table 3.11. The local mechanical properties of individual phases are given in Table 3.2.

3.2 Influences of various factors

Table 3.11: Influences of degree of hydration on the tensile mechanical properties of cement paste at microscale

Curing age (h)	29	67	83	162	203	1999	7947	12 593
Degree of hydration	31 %	44 %	47 %	55 %	58 %	79 %	88 %	90 %
Porosity	36.2 %	27.2 %	25.2 %	20.0 %	18.4 %	8.2 %	5.4 %	4.8 %
Young's modulus E (GPa)	1.9	4.8	5.6	8.2	9.1	15.7	17.5	17.9
Tensile strength f_t (MPa)	2.7	6.9	8.5	12.4	14.1	27.1	31.5	31.6
Strain at peak load ϵ_p	0.37 %	0.28 %	0.21 %	0.22 %	0.19 %	0.19 %	0.20 %	0.20 %
Fracture energy G_F (J/m ²)	6.4	13.1	14.7	20.8	24.1	14.9	14.3	14.4

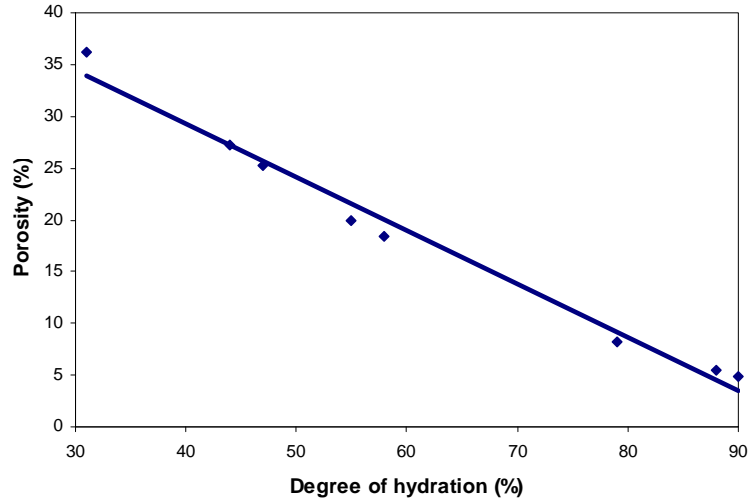


Figure 3.20: Porosity of the hydrating cement paste system against degree of hydration

The porosity of the hydrating cement paste is decreasing when the hydration process continues, as shown in Figure 3.20, and strong linear relevance is found. The pores in the system are filled by hydration products gradually, resulting in a microstructure with low porosity in the end.

Both the Young's modulus and the tensile strength increase linearly with the increase of degree of hydration, as shown in Figure 3.21, which is obtained based on the data from Table 3.11. As the porosity is linearly dependent on the degree of hydration, it can be derived that the Young's modulus and the tensile strength also change linearly against the porosity, as shown in Figure 3.22. The

3. CEMENT PASTE AT MICROSCALE

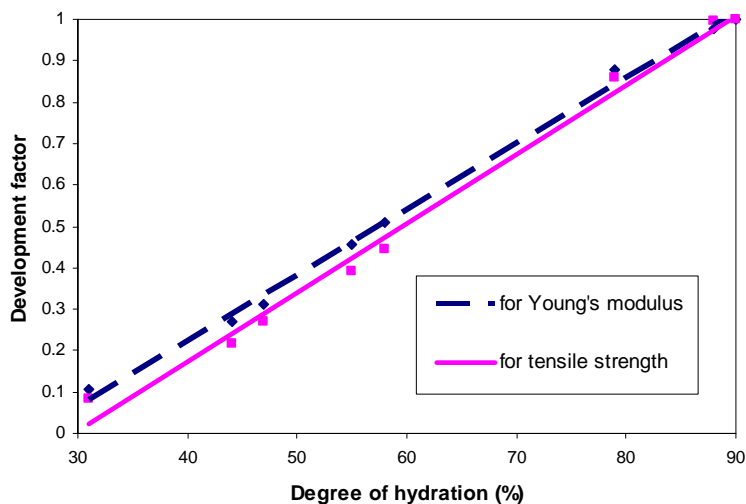


Figure 3.21: Development of the Young's modulus and the tensile strength against the degree of hydration

development of Young's modulus and tensile strength is due to the continuous maturing of the microstructure of cement paste during hydration, and eventually a well developed system is obtained.

At the initial stage of hydration, the strain at peak load is relatively high, up to 0.37% at the degree of hydration 31%, then it drops to the range of [0.19%, 0.22%] when the degree of hydration reaches 47%, and then it stays in that range although the hydration process continues, as shown in Figure 3.23. This suggests that the tensile strain at peak load for well developed cement paste is about 0.2% at microscale.

The fracture energy increases first and then decreases during the hydration process, as shown in Figure 3.24. The paste system is getting stronger all the time, which would increase the fracture energy. At earlier stage the number of microcracks in the final failure state also increases as shown in Figure 3.27(a) and (b), thus the more fracture energy is required to break the system. However, a more localized cracks pattern shows up for better developed microstructure at later stage as shown in Figure 3.27(b) and (c). Thus less microcracks are required to bring the system to failure, which would decrease the fracture energy. The two forces that higher strength and less microcracks push the change of fracture

3.2 Influences of various factors

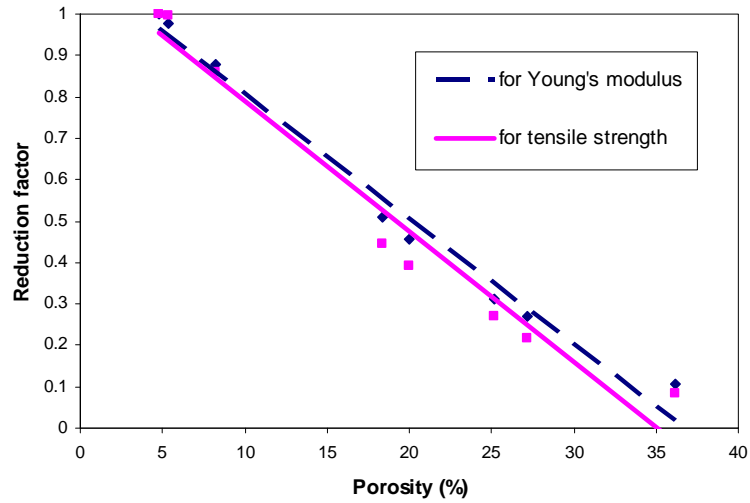


Figure 3.22: Trendlines of the Young's modulus and the tensile strength against the porosity of the cement paste system

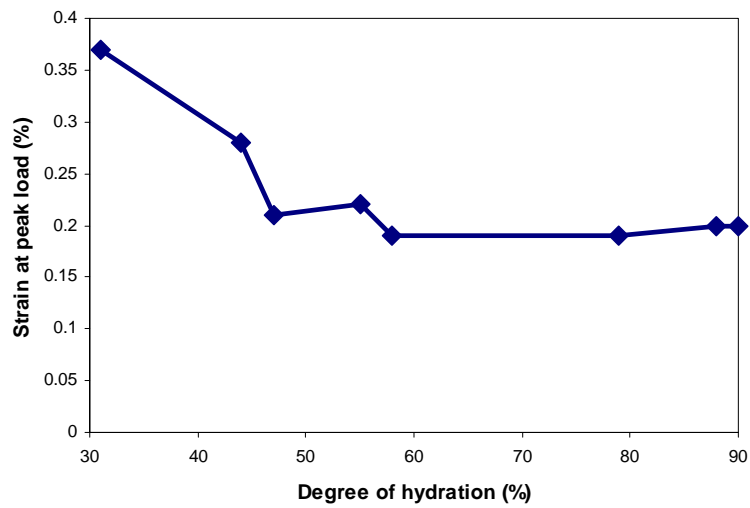


Figure 3.23: Relationship between the strain at peak load and the degree of hydration

3. CEMENT PASTE AT MICROSCALE

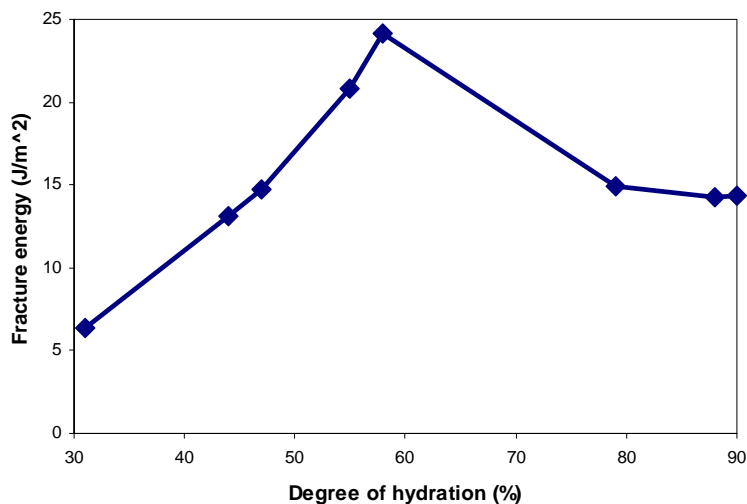


Figure 3.24: Relationship between the fracture energy and the degree of hydration

energy towards opposite directions, hence the net effect is dependent on which force wins. The curve in Figure 3.24 shows that the effect of less microcracks becomes dominant for paste at high degree of hydration.

In this particular example it is observed that the fracture energy reaches the maximum when the porosity of the system is 18.4%, as shown in Figure 3.25. It indicates that a low porosity does not correspond to a system which can absorb maximum energy during the fracture processes. If seeking capacity to absorb fracture energy is the objective when designing a material, then leaving some pores in the system may help. More investigations on this aspect could be done to find out the relationship between the fracture energy and the porosity of the system under varying conditions.

The entire stress-strain responses are compared at three different degrees of hydration, which are 44%, 58% and 90%, as shown in Figure 3.26. The cracks patterns in the final failure state are given in Figure 3.27. The two figures suggest that the paste behaves more brittle and microcracks are more localized at higher degree of hydration. The number of microcracks in the final failure state increases with the degree of hydration at early stage of hydration, and then decreases after the degree of hydration exceeds a certain level. The increase is because more and more solid phases are present in the microstructure, while the decrease is the

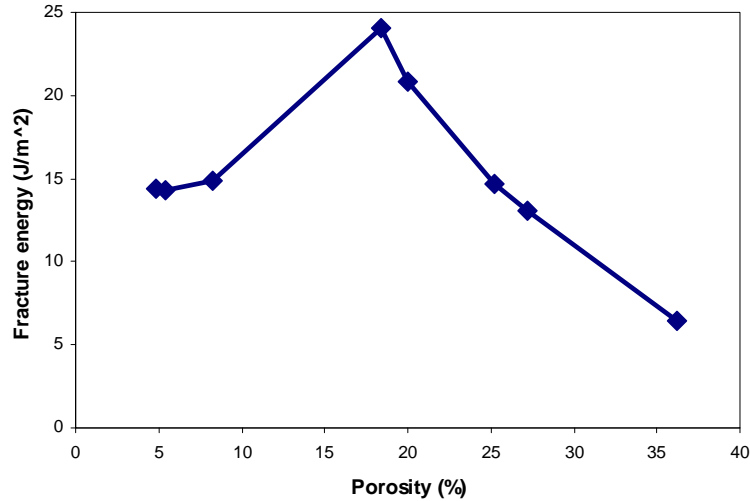


Figure 3.25: Relationship between the fracture energy and the porosity

result of cracks localization.

3.2.2 Cement fineness

The cement fineness can be indicated by the Blaine value. A higher Blaine value represents finer cement particles. The cement paste mixture in Table 3.1 is used and the cement fineness is varied at 210 m²/kg, 420 m²/kg and 600 m²/kg respectively. The microstructures are simulated by the HYMOSTRUC3D model and then their mechanical properties are predicted by the 3D lattice fracture analysis. The local mechanical properties of individual solid phase are listed in Table 3.2.

The fineness of cement affects the hydration rate, i.e. finer cement hydrates faster, as shown in Table 3.12. Higher degree of hydration corresponds with lower porosity, higher Young's modulus and higher tensile strength. The strains at peak load for these three microstructures are almost the same, around 0.2%, which supports the findings from Figure 3.23. The fracture energy goes with cement fineness due to the fact that higher strength is reached at a higher degree of hydration at 28 days and the crack localization is not dominant yet, as shown in Figure 3.28.

It is also possible to compare the mechanical behavior of paste at the same degree of hydration instead of at the same curing age. The stress-strain response

3. CEMENT PASTE AT MICROSCALE

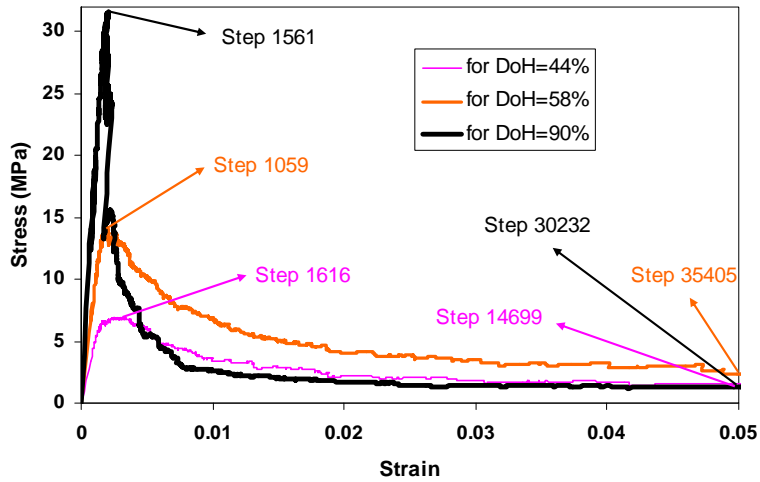


Figure 3.26: Influences of degree of hydration on the tensile stress-strain response

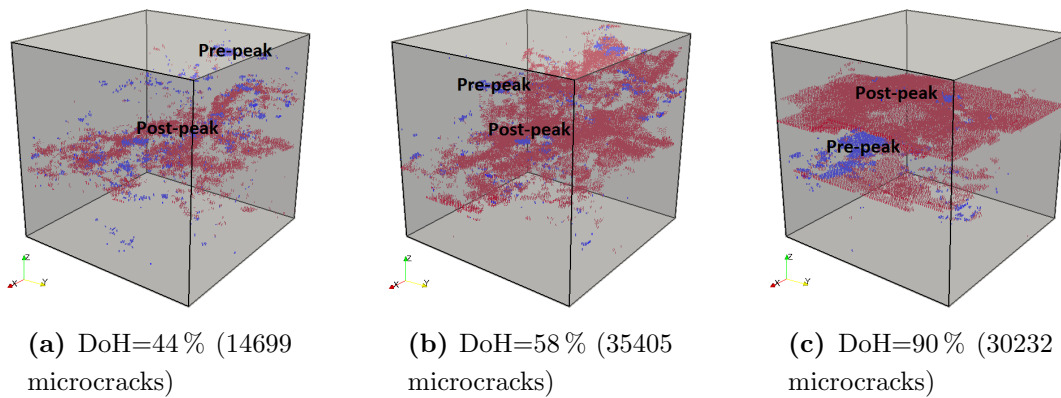


Figure 3.27: Influences of degree of hydration on the cracks pattern in the final failure state, corresponding with Figure 3.26

3.2 Influences of various factors

Table 3.12: Influences of cement fineness, compared at the same curing age of 28 days, all values are resulted from simulations

Cement fineness (m^2/kg)	210	420	600
Degree of hydration	62 %	69 %	73 %
Porosity	15.0 %	12.5 %	11.1 %
Young's modulus E (GPa)	11.0	12.9	14.3
Tensile strength f_t (MPa)	14.9	20.3	28.2
Strain at peak load ϵ_p	0.18 %	0.18 %	0.21 %
Fracture energy G_F (J/m^2)	18.9	21.6	23.2

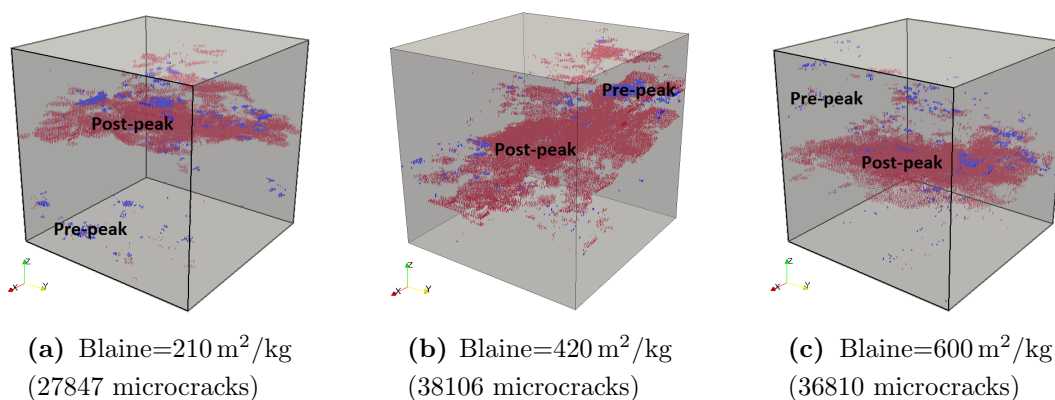


Figure 3.28: Influences of cement fineness on the cracks pattern in the final failure state, compared at the same curing age of 28 days, corresponding with Table 3.12

3. CEMENT PASTE AT MICROSCALE

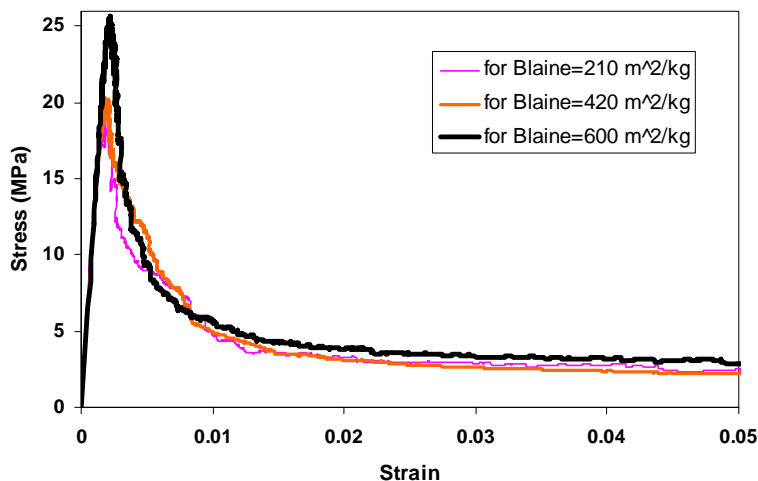


Figure 3.29: Influences of cement fineness on the tensile stress-strain response, compared at the same degree of hydration 69 %

diagrams are given in Figure 3.29 for cement paste specimens with different cement fineness. The computed Young's modulus is independent of the Blaine value. The tensile strength and fracture energy are higher for finer cement paste system, as it contains smaller but more particles to fill the gap between big particles. The cracks patterns in the final failure state are shown in Figure 3.30.

3.2.3 Water/cement ratio

The water/cement ratio of the cement paste mixture in Table 3.1 is varied at 0.3, 0.4 and 0.5 to study its influences on the mechanical properties of paste. The HYMOSTRUC3D model gives the microstructures, and then the 3D lattice fracture model evaluates the mechanical performance by simulating a uniaxial tensile test on the $100\ \mu\text{m} \times 100\ \mu\text{m} \times 100\ \mu\text{m}$ specimen, using the local mechanical properties of individual solid phases given in Table 3.2.

The water/cement ratio influences the hydration rate. A higher water/cement ratio speeds up the hydration process, as shown in Table 3.13. However, a higher degree of hydration does not result in lower porosity, because of the higher initial water/cement ratio. The change trend of Young's modulus and tensile strength can be linked to the porosity. The strain at peak load is about 0.2%, which

3.2 Influences of various factors

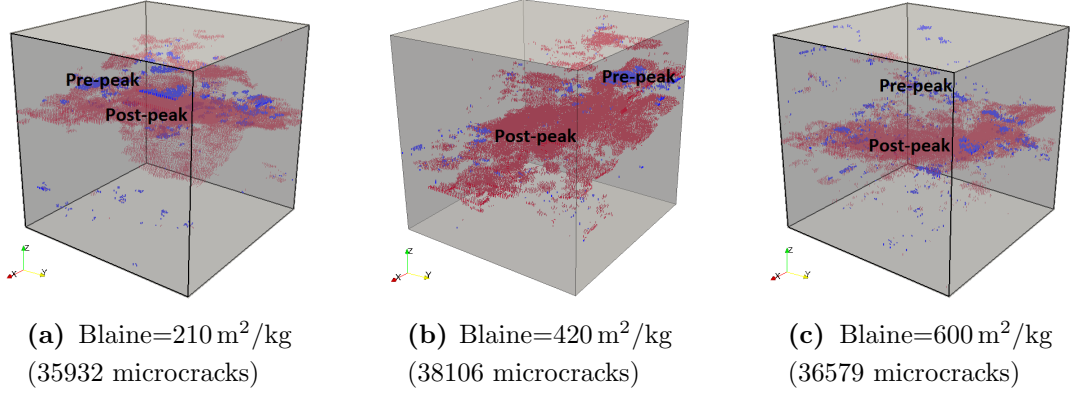


Figure 3.30: Influences of cement fineness on the cracks pattern in the final failure state, compared at the same degree of hydration 69 %, corresponding with Figure 3.29

supports the findings from Figure 3.23. The fracture energy decreases when the water/cement ratio increases, which is dominated by the decrease of the tensile strength. The cracks patterns at the same curing age of 28 days are shown in Figure 3.31. It is apparent that a more localized microcracks pattern is observed in the cement paste with lower water/cement ratio.

It is also possible to compare the mechanical performance of paste at the same degree of hydration, as given in Table 3.14. Higher water/cement ratio takes less time to reach the target degree of hydration 69 %, and is accompanied by higher

Table 3.13: Influences of water/cement ratio, compared at the same curing age of 28 days

Water/cement ratio	0.3	0.4	0.5
Degree of hydration	65 %	69 %	75 %
Porosity	3.2 %	12.5 %	20.1 %
Young's modulus E (GPa)	23.4	12.9	7.0
Tensile strength f_t (MPa)	42.1	20.3	10.6
Strain at peak load ϵ_p	0.19 %	0.18 %	0.18 %
Fracture energy G_F (J/m ²)	23.1	21.6	12.3

3. CEMENT PASTE AT MICROSCALE

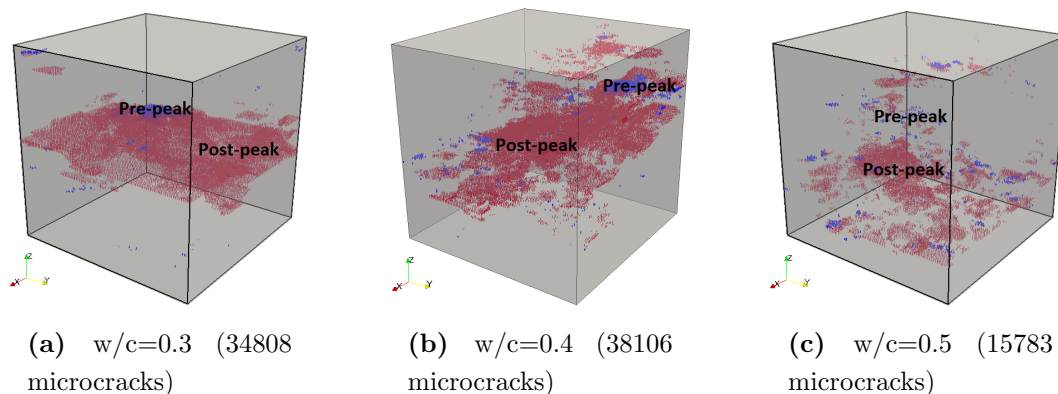


Figure 3.31: Influences of water/cement ratio on the cracks pattern in the final failure state, compared at the same curing age of 28 days, corresponding with Table 3.13

porosity, lower Young's modulus and tensile strength. The strains at peak load for the three cases are about the same, around 0.2%, which supports the findings from Figure 3.23. The fracture energy is dependent on the strength and the number of microcracks in the final failure state. The water/cement ratio 0.4 produces more microcracks and thus requires the highest fracture energy among the three cases, although the strength is not the highest one. The stress-strain response diagrams are given in Figure 3.32. More brittle softening behavior is observed for the lower water/cement ratio system. The cracks patterns in the final failure state are given in Figure 3.33. It is observed that microcracks are more localized in the paste with lower water/cement ratio.

3.2.4 Mineral composition of cement

The hydration processes and products are dependent on the mineral composition of cement. Hence the mechanical performance of cement paste can be altered by changing the cement mineral composition. The ordinary Portland cement usually consists of C_3S , C_2S , C_3A and C_4AF . Four special combinations are made to study the effect of C_3S and C_2S on the mechanical properties of cement paste, as given in Table 3.15. These special cements are produced in laboratory by Italcementi in Italy [42]. The particle size distributions are measured and then

3.2 Influences of various factors

Table 3.14: Influences of water/cement ratio, compared at the same degree of hydration 69 %

Water/cement ratio	0.3	0.4	0.5
Curing age (h)	1262	635	402
Porosity	2.0 %	12.5 %	22.5 %
Young's modulus E (GPa)	24.2	12.9	6.0
Tensile strength f_t (MPa)	41.7	20.3	9.0
Strain at peak load ϵ_p	0.19 %	0.18 %	0.18 %
Fracture energy G_F (J/m ²)	17.7	21.6	12.0

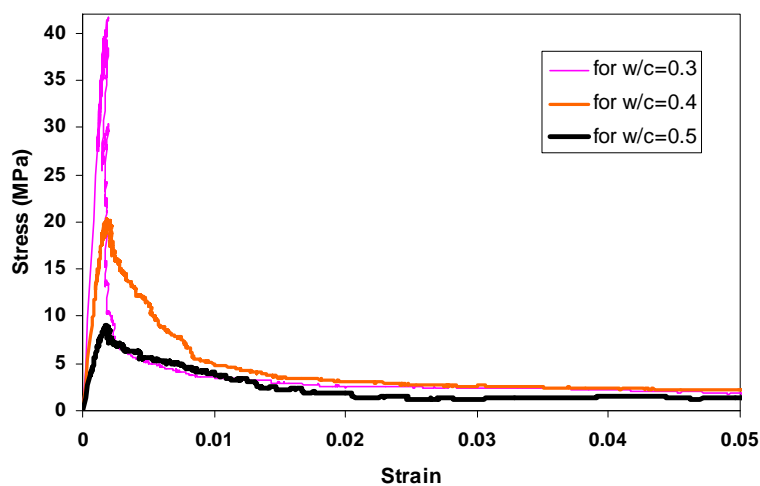


Figure 3.32: Influences of water/cement ratio on the tensile stress-strain response, compared at the same degree of hydration 69 %, corresponding with Table 3.14

3. CEMENT PASTE AT MICROSCALE

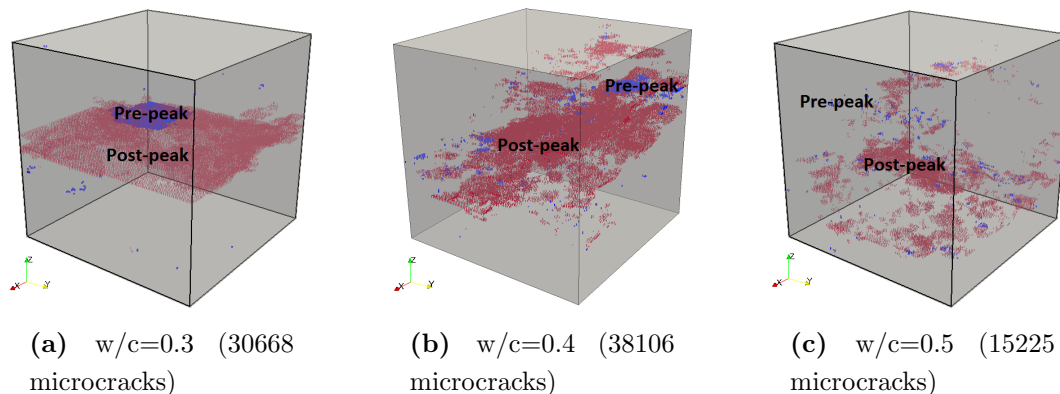


Figure 3.33: Influences of water/cement ratio on the cracks pattern in the final failure state, compared at the same degree of hydration 69 %, corresponding with Figure 3.32

Table 3.15: Mineral compositions of the special cements

Combination	C_3S	C_2S
(a)	100 %	0
(b)	70 %	30 %
(c)	30 %	70 %
(d)	0	100 %

hydration tests are carried out by CSIC (Spanish National Research Council) in Spain [43]. Several batches of the special cements are measured and a Rosin-Rammler distribution $F(x) = 1 - e^{-bx^n}$ with $n = 1.014$ and $b = 0.0754$ is fitted, as shown in Figure 3.34. The corresponding Blaine value is $600 \text{ m}^2/\text{kg}$. The fitted curve will be used in the HYMOSTRUC3D model to simulate the microstructures of cement paste.

In the numerical experiment the water/cement ratio is 0.4 and the specimen size is $100 \mu\text{m} \times 100 \mu\text{m} \times 100 \mu\text{m}$. The initial microstructures of cement paste for the four combinations of mineral compositions are the same, because the same particle size distribution and water/cement ratio are applied, as shown in Figure 3.35.

The degrees of hydration are measured and simulated for the four combina-

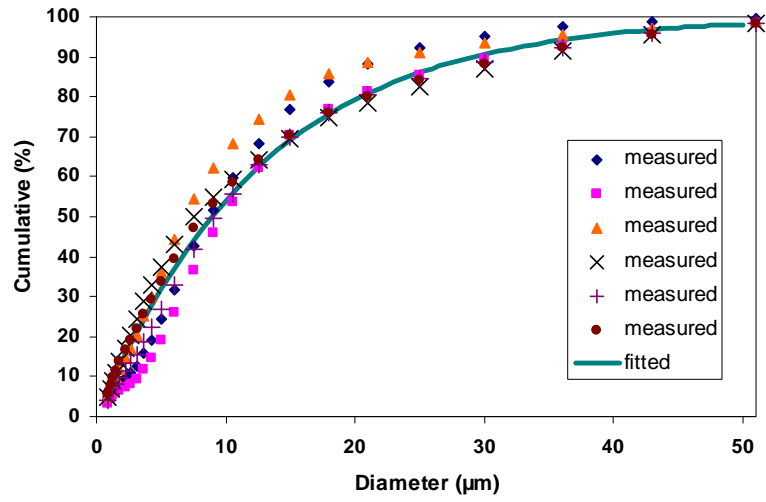


Figure 3.34: Particle size distribution of the special cements

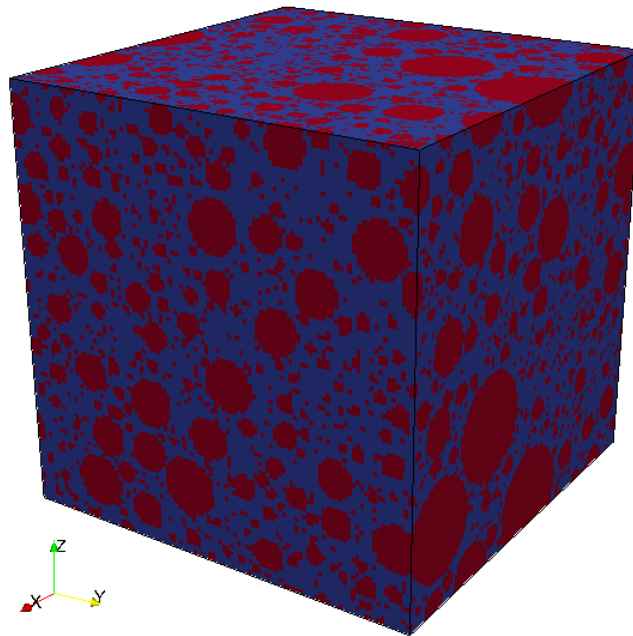


Figure 3.35: Initial microstructure of the special cement paste (porosity=56%)

3. CEMENT PASTE AT MICROSCALE

Table 3.16: Degree of hydration and phase segmentation for the special cement pastes at the curing age of 28 days, corresponding with Figure 3.37

Combination	Degree of hydration	Pore	Unhydrated cement	Inner product	Outer product
(a)	79%	8%	9%	35%	48%
(b)	84%	6%	7%	37%	50%
(c)	68%	12%	14%	30%	44%
(d)	38%	30%	27%	17%	26%

tions respectively, and the resulting hydration diagrams are shown in Figure 3.36. The microstructures at the curing age of 28 days are taken for further analysis, as shown in Figure 3.37. The corresponding degree of hydration and phase segmentation are given in Table 3.16. It is observed that C_3S hydrates faster than C_2S by comparing the combination (a) and (d). However, the combination (b) hydrates faster than pure C_3S , even though it consists of some C_2S . This phenomenon can be explained by separating the hydrations of C_3S and C_2S . The combination (b) can be obtained by replacing 30% C_3S with C_2S based on the combination (a). At 28 days the 30% C_2S consumes less water than C_3S as C_2S hydrates slower, the effect is the 70% C_3S could attract more water, thus its hydration process speeds up. The 30% C_2S hydrates slower while the 70% C_3S hydrates faster, the net effect is determined by the amount portions of C_3S and C_2S . When the weight of C_2S is increased to 70%, as shown in the combination (c), the hydration rate is decreased.

The 3D lattice fracture model is employed to evaluate the mechanical performance of the microstructures in Figure 3.37 through simulating a uniaxial tensile test. The local mechanical properties for individual solid phases are taken from Table 3.2. The resulting stress-strain response diagrams are shown in Figure 3.38. Some global mechanical properties are computed and summarized in Table 3.17 based on Figure 3.38. The microcracks in the final failure state are shown in Figure 3.39. The combination (b) has the best mechanical performance in terms of Young's modulus and tensile strength, and the most localized cracks pattern, as its degree of hydration is the highest one among the four combinations. This suggests that the mineral composition of the ordinary Portland cement is already

3.2 Influences of various factors

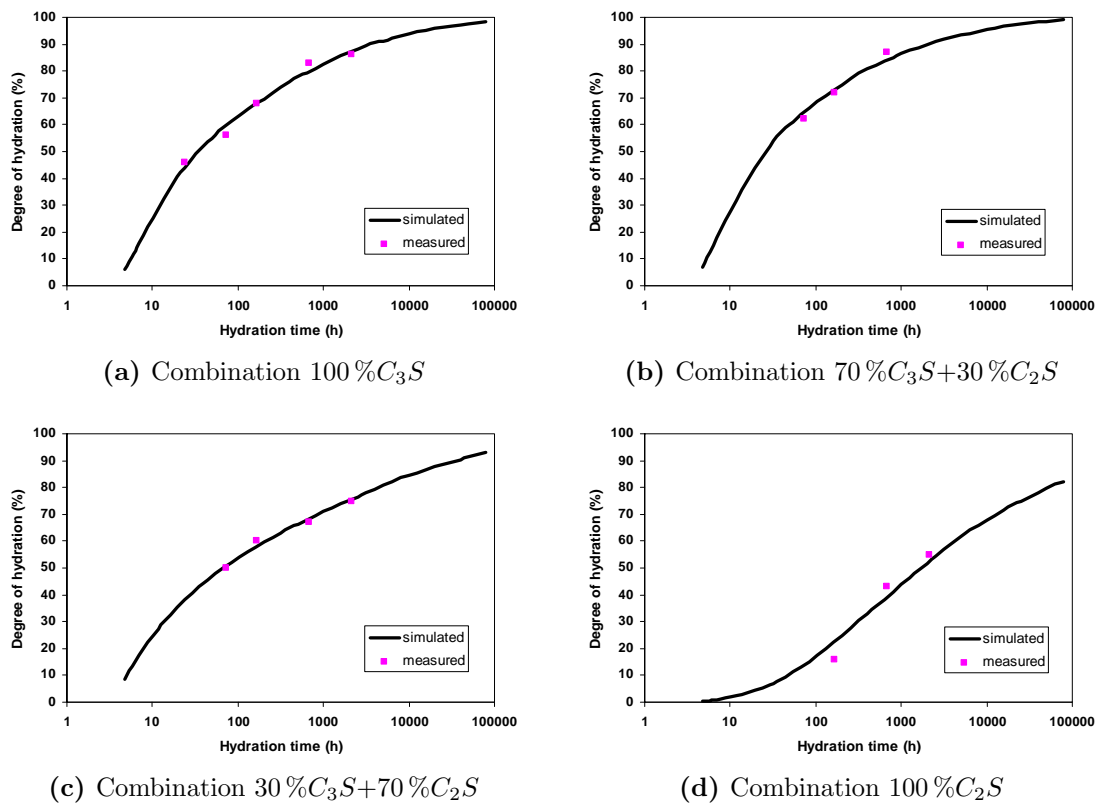
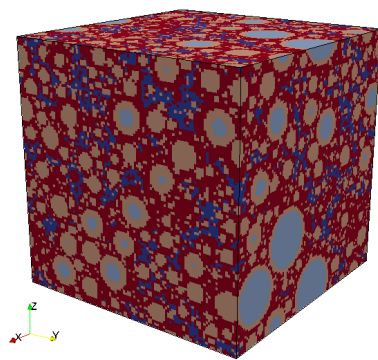
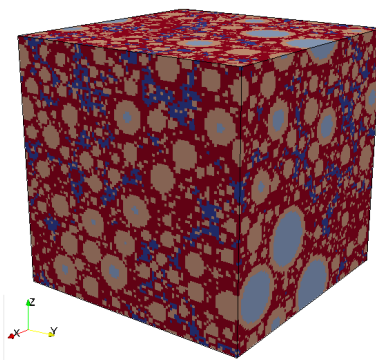


Figure 3.36: Degree of hydration diagrams for the special cement pastes

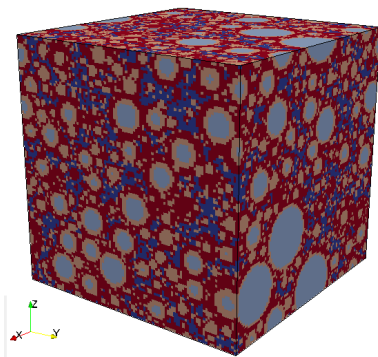
3. CEMENT PASTE AT MICROSCALE



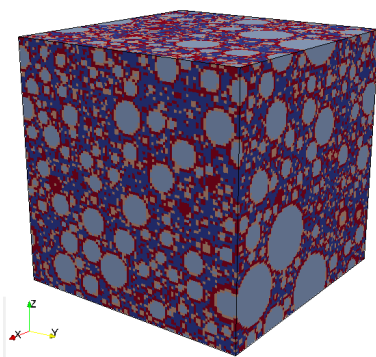
(a) Combination 100 % C_3S
(porosity=8 %)



(b) Combination
70 % C_3S +30 % C_2S
(porosity=6 %)



(c) Combination
30 % C_3S +70 % C_2S
(porosity=12 %)



(d) Combination 100 % C_2S
(porosity=30 %)

Figure 3.37: Microstructures of the special cement pastes at the curing age of 28 days

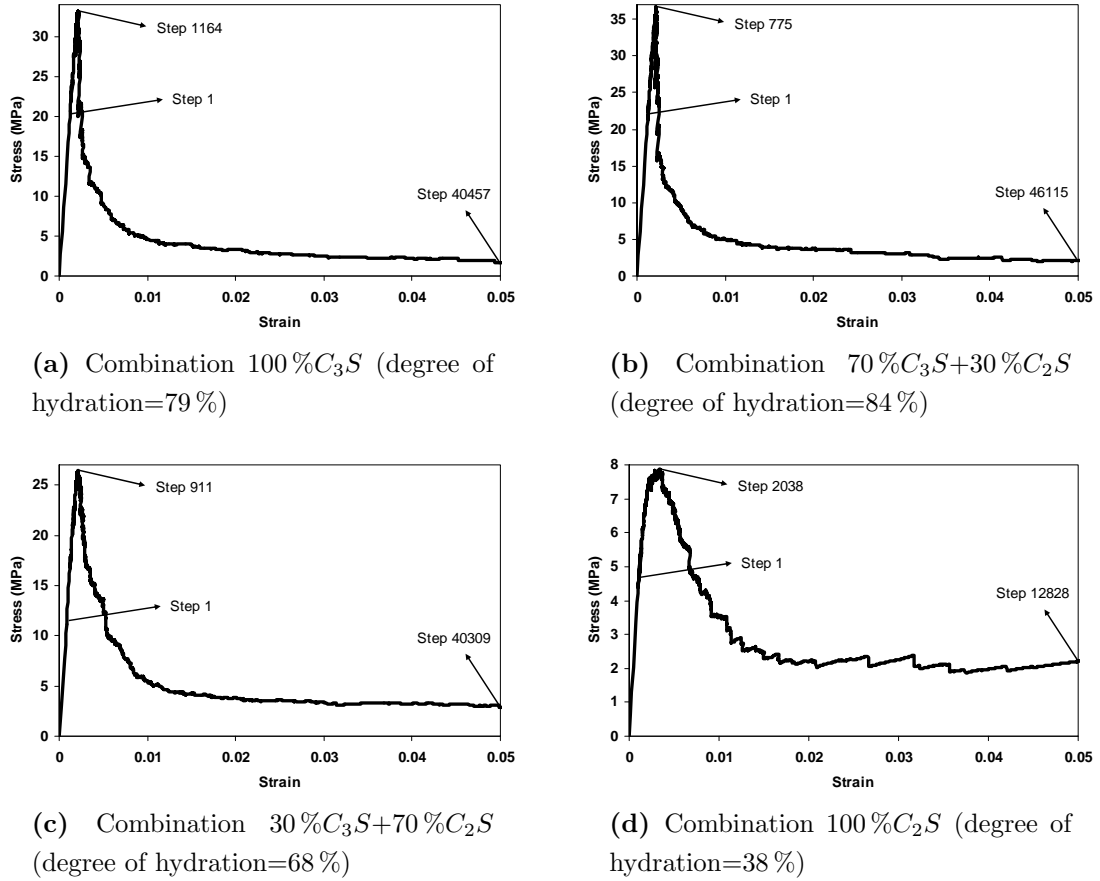


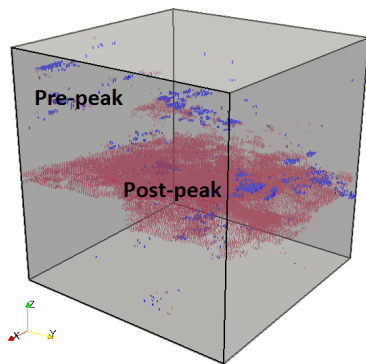
Figure 3.38: Stress-strain response diagrams for the special cement pastes at the curing age of 28 days

optimized, as combination (b) is the most similar one to the ordinary Portland cement.

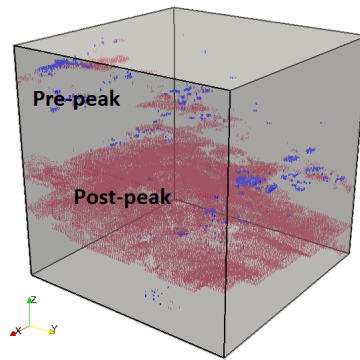
3.3 Summary

The microstructure of cement paste and its mechanical performance are studied numerically in detail in this chapter. The microstructure of cement paste can be obtained by the HYMOSTRUC3D computer modeling program, and/or by the experimental method of CT scan. The 3D lattice fracture model developed in Chapter 2 is employed to predict the mechanical properties and cracks propaga-

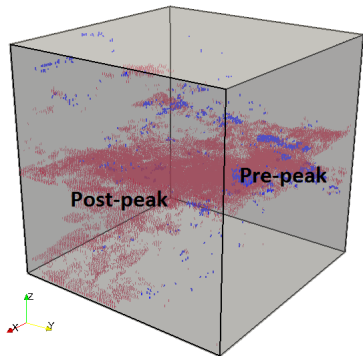
3. CEMENT PASTE AT MICROSCALE



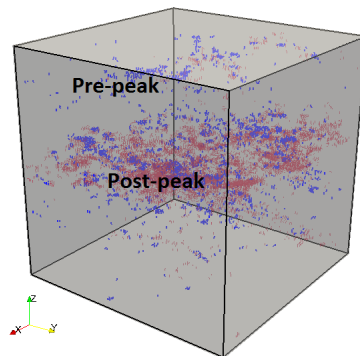
(a) Combination 100% C_3S
(40457 microcracks)



(b) Combination
70% C_3S +30% C_2S (46115
microcracks)



(c) Combination
30% C_3S +70% C_2S (40309
microcracks)



(d) Combination 100% C_2S
(12828 microcracks)

Figure 3.39: Cracks patterns in the final failure state for the special cement pastes at the curing age of 28 days, corresponding with Figure 3.38

Table 3.17: Global mechanical properties of the special cement pastes at the curing age of 28 days, corresponding with Figure 3.38

Combination	Young's modulus E (GPa)	Tensile strength f_t (MPa)	Strain at peak load ϵ_p	Fracture energy G_F (J/m ²)
(a)	17	33	0.22 %	22
(b)	18	37	0.22 %	23
(c)	14	26	0.21 %	26
(d)	4.2	7.9	0.33 %	14

tion by simulating a uniaxial tensile test on the microstructure of cement paste at microscale. The influences of loading directions and mesh randomness are examined. The simulated mechanical properties of $100 \mu\text{m} \times 100 \mu\text{m} \times 100 \mu\text{m}$ cement paste specimen are used as input properties for mesoscale modeling in Chapter 5.

Some factors, such as degree of hydration, cement fineness, water/cement ratio and mineral composition of cement were investigated to see their influences on the mechanical performance of cement paste at microscale. It turns out that better mechanical properties can be achieved with higher degree of hydration, finer cement and lower water/cement ratio, and the mineral composition of ordinary Portland cement is already an optimal combination. Both the Young's modulus and the tensile strength increases linearly against the increase of degree of hydration, while the fracture energy increases first and then decreases during the hydration process. At the same degree of hydration the Young's modulus is independent of the Blaine value, but the tensile strength and fracture energy are higher for finer cement paste system. The increase of water/cement ratio results in a decrease of Young's modulus and tensile strength, while the fracture energy goes up first and then down if compared at the same degree of hydration. It is observed that the tensile strain at peak load for well developed cement paste is about 0.2% at microscale in the numerical experiments. It is also interesting to notice that the system with lowest porosity does not have the maximum capacity to absorb the energy during the fracture processes, thus planting some pores in the system may help to improve the fracture energy dissipation.

3. CEMENT PASTE AT MICROSCALE

Chapter 4

Mortar and Concrete at Mesoscale

Concrete is a kind of multiscale and multiphase heterogeneous construction material. Normal concrete is made from coarse aggregates (e.g. crushed stones, river gravels), fine aggregates (e.g. sands), cement and water. A chemical reaction starts immediately when water is mixed with cement, and reaction products are produced. The resulting cement paste keeps aggregates together and forms a system which is able to carry loads. Mortar consists of cement paste and sand, and concrete is composed of mortar and coarse aggregates. The relationship between cement paste, mortar and concrete is illustrated in Figure 4.1.

From the modeling point of view, the material mesostructures of both mortar and concrete can be represented by particles embedded in matrix material model, as shown in Figure 4.2. The particles are interpreted as sands, and the matrix



Figure 4.1: Cement paste, mortar and concrete

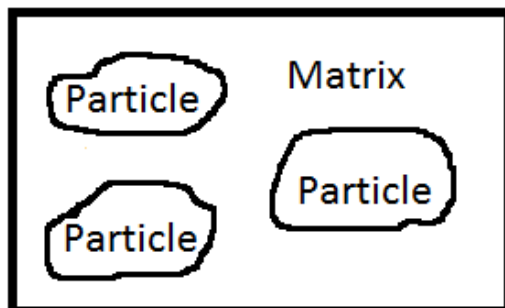


Figure 4.2: Particles embedded matrix material model

as cement paste for mortar model, while the particles are coarse aggregates, and the matrix is mortar in the concrete model. Hence it is achievable to make a universal material mesostructure model for mortar and concrete. However, the particle shape characterizations can be different for sands and coarse aggregates, and furthermore they can even be different for different classes of sands or coarse aggregates. This requires the universal material model to be able to recognize various particle shape characterizations. It is pointed out by Garboczi that spherical harmonics is a good mathematical tool to characterize the shape of particles numerically, and the procedures to retrieve particle shape characterizations for a given class of aggregates from CT (computed tomography) scanned digital images are also established [44]. The next step is to place multiple irregular shape particles into a pre-defined empty container to build up a complete particles embedded in matrix material model, which is elaborated in Section 4.1. An application of the proposed material model is given in Section 4.2, for simulating the mesostructures of mortar and concrete respectively.

4.1 Anm material model

There are many existing particles embedded in matrix material models [45, 46, 47, 48], most of which employ regular shape particles like spheres, ellipsoids, or multi-faceted polyhedrons, as shown in Figure 4.3. However, the real particle shapes are more complex and sometimes play an essential role. In this section a material model with irregular shape particles is proposed, the Anm material

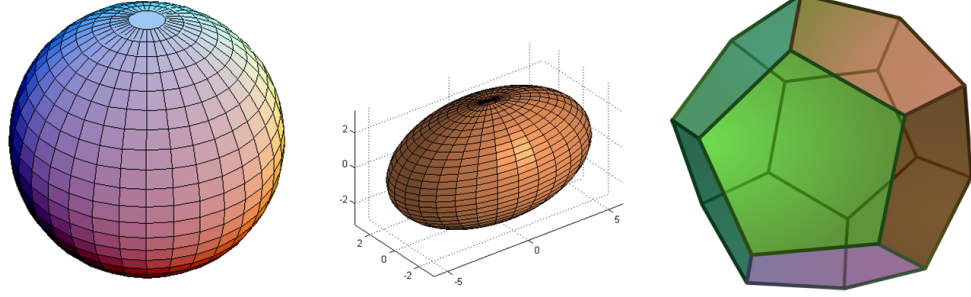


Figure 4.3: Spheres, ellipsoids and multi-faceted polyhedrons [<http://wikipedia.org>]

model, which is named after the fact that the particle shapes are described in terms of spherical harmonic expansion coefficients a_{nm} .

4.1.1 Irregular shape description

In mathematics an arbitrary 2D surface can be represented by a function $r(\theta, \phi)$ in the 3D spherical coordinate system as shown in Figure 4.4. The particle mass center is placed at the origin in the local coordinate system.

The function $r(\theta, \phi)$ might be difficult or even impossible to be expressed explicitly for complex shapes, but it can always be approximated by a summation of spherical harmonic functions for star-like shapes [49, 50, 51]. The spherical harmonic expansion is given in the equation (4.1),

$$r(\theta, \phi) = \sum_{n=0}^{\infty} \sum_{m=-n}^n a_{nm} Y_n^m(\theta, \phi) \quad (4.1)$$

where $r(\theta, \phi)$ is any smooth function defined on the unit sphere ($0 \leq \theta \leq \pi, 0 \leq \phi < 2\pi$), $Y_n^m(\theta, \phi)$ is the spherical harmonic function and is given in the equation (4.2),

$$Y_n^m(\theta, \phi) = \sqrt{\frac{(2n+1)(n-m)!}{4\pi(n+m)!}} P_n^m(\cos \theta) e^{im\phi} \quad (4.2)$$

in which $P_n^m(\cos \theta)$ is the associated Legendre polynomial, i is the imaginary unit.

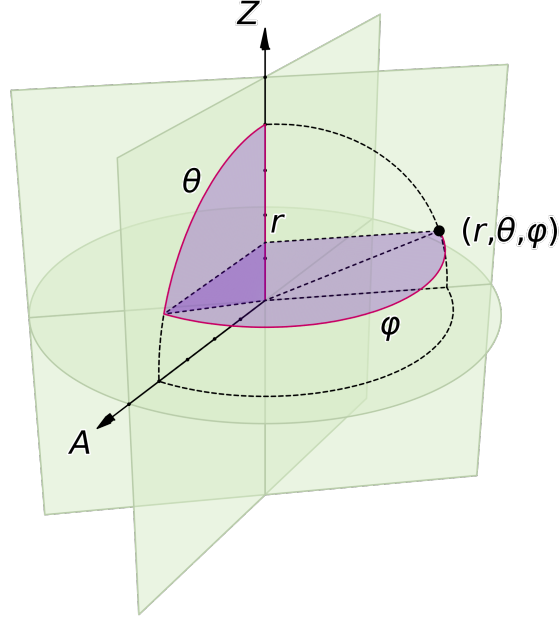


Figure 4.4: Spherical coordinate system [<http://wikipedia.org>]

The first derivatives of the function $r(\theta, \phi)$ are involved in the expressions (4.25) and can be computed as follows,

$$\begin{cases} \frac{\partial r(\theta, \phi)}{\partial \theta} = \sum_{n=0}^{\infty} \sum_{m=-n}^n a_{nm} \frac{\partial Y_n^m(\theta, \phi)}{\partial \theta} \\ \frac{\partial r(\theta, \phi)}{\partial \phi} = \sum_{n=0}^{\infty} \sum_{m=-n}^n a_{nm} \frac{\partial Y_n^m(\theta, \phi)}{\partial \phi} \end{cases} \quad (4.3)$$

where the two derivatives of the spherical harmonic function $Y_n^m(\theta, \phi)$ can be computed as below,

$$\begin{cases} \frac{\partial Y_n^m(\theta, \phi)}{\partial \theta} = \frac{1}{s} \left(nxY_n^m(\theta, \phi) - \sqrt{\frac{(2n+1)(n^2-m^2)}{2n-1}} Y_{n-1}^m(\theta, \phi) \right) \\ \frac{\partial Y_n^m(\theta, \phi)}{\partial \phi} = imY_n^m(\theta, \phi) \end{cases} \quad (4.4)$$

in which $x = \cos \theta$ and $s = \sqrt{1-x^2}$.

Proof. Here is the derivation about $\frac{\partial Y_n^m(\theta, \phi)}{\partial \theta}$ in the equation (4.4).

$$(x^2 - 1) \frac{dP_n^m(x)}{dx} = nxP_n^m(x) - (n+m)P_{n-1}^m(x) \quad (4.5)$$

let $x = \cos \theta$, $s = \sqrt{1 - x^2}$,

$$\begin{aligned}
 \frac{dP_n^m(\cos \theta)}{d\theta} &= \frac{dP_n^m(x)}{dx} \frac{dx}{d\theta} \\
 &= -\sin \theta \frac{dP_n^m(x)}{dx} \\
 &= -\sin \theta \frac{nxP_n^m(x) - (n+m)P_{n-1}^m(x)}{x^2 - 1} \\
 &= -s \frac{nxP_n^m(x) - (n+m)P_{n-1}^m(x)}{-s^2} \\
 &= \frac{nx}{s} P_n^m(x) - \frac{n+m}{s} P_{n-1}^m(x)
 \end{aligned} \tag{4.6}$$

$$\begin{aligned}
 \therefore \frac{\partial Y_n^m(\theta, \phi)}{\partial \theta} &= \sqrt{\frac{(2n+1)(n-m)!}{4\pi(n+m)!}} e^{im\phi} \frac{dP_n^m(\cos \theta)}{d\theta} \\
 &= \sqrt{\frac{(2n+1)(n-m)!}{4\pi(n+m)!}} e^{im\phi} \left(\frac{nx}{s} P_n^m(x) - \frac{n+m}{s} P_{n-1}^m(x) \right) \\
 &= \frac{nx}{s} \sqrt{\frac{(2n+1)(n-m)!}{4\pi(n+m)!}} P_n^m(x) e^{im\phi} - \frac{n+m}{s} \sqrt{\frac{(2n+1)(n-m)!}{(2n-1)(n+m)}} \\
 &\quad \sqrt{\frac{[2(n-1)+1][(n-1)-m]!}{4\pi[(n-1)+m]!}} P_{n-1}^m(x) e^{im\phi} \\
 &= \frac{nx}{s} Y_n^m(\theta, \phi) - \frac{1}{s} \sqrt{\frac{(2n+1)(n^2-m^2)}{2n-1}} Y_{n-1}^m(\theta, \phi) \\
 &= \frac{1}{s} \left(nx Y_n^m(\theta, \phi) - \sqrt{\frac{(2n+1)(n^2-m^2)}{2n-1}} Y_{n-1}^m(\theta, \phi) \right)
 \end{aligned} \tag{4.7}$$

□

Proof. Here is the derivation about $\frac{\partial Y_n^m(\theta, \phi)}{\partial \phi}$ in the equation (4.4).

$$\begin{aligned}
 \frac{\partial Y_n^m(\theta, \phi)}{\partial \phi} &= \sqrt{\frac{(2n+1)(n-m)!}{4\pi(n+m)!}} P_n^m(\cos \theta) e^{im\phi} im \\
 &= im Y_n^m(\theta, \phi)
 \end{aligned} \tag{4.8}$$

□

The particle shape is uniquely defined by a set of spherical harmonic coefficients a_n^m , which is a complex number. The data structure of the coefficients a_n^m is shown in Figure 4.5, where n is the degree and m is the order.

4. MORTAR AND CONCRETE AT MESOSCALE

$n = 0$			$a_{0,0}$		
$n = 1$		$a_{1,-1}$	$a_{1,0}$	$a_{1,1}$	
$n = 2$	$a_{2,-2}$	$a_{2,-1}$	$a_{2,0}$	$a_{2,1}$	$a_{2,2}$
			\dots		
	$m = -2$	$m = -1$	$m = 0$	$m = 1$	$m = 2$

Figure 4.5: Spherical harmonic coefficients data structure

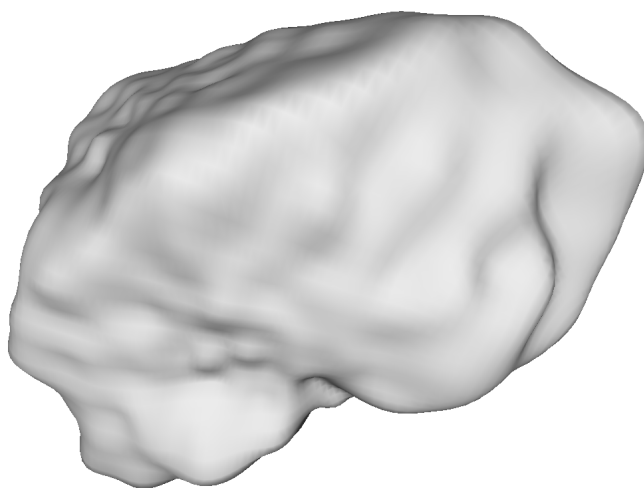


Figure 4.6: An irregular shape particle described by spherical harmonics

The number of the coefficients up to the degree n is $(n + 1)^2$, and the index of the coefficient is $n(n + 1) + m$. There should be sufficient coefficients involved in the spherical harmonic expansion to describe a shape accurately. The number of the coefficients required is dependent on the shape characterizations. As a general guideline, the degree n should be about 26 for common aggregates in mortar and concrete, thus the corresponding number of coefficients is about $(26 + 1)^2 = 729$. See [44] for more discussions on this aspect. An example irregular shape particle described in terms of spherical harmonic coefficients is shown in Figure 4.6.

4.1.2 Individual particle properties and operations

Many geometric properties of the particle shape can be computed once the spherical harmonic coefficients are known, including the particle volume, length, width and thickness. Length is the longest surface-surface distance in the particle, width is the longest surface-surface distance in the particle such that width is perpendicular to length, and thickness is the longest surface-surface distance in the particle such that thickness is perpendicular to both length and width [44]. A particle can be scaled by multiplying each coefficient with a scaling factor. The scaling factor s is determined by the equation (4.9),

$$s = \frac{W_a}{W_b} \quad (4.9)$$

where W_a is the particle width after scaling, and W_b is the width before scaling. The particle volume will be also be scaled according to the equation (4.10),

$$V_a = s^3 V_b \quad (4.10)$$

where V_a is the particle volume after scaling, and V_b is the volume before scaling.

The operation of a rotation on the particle in the local coordinate system can be done by transforming the spherical harmonic expansion coefficients [50]. Denote the rotation Euler angles as α, β, γ , then the new spherical harmonic coefficients after rotation can be determined by the equation (4.11),

$$a_{nm}^{\text{new}} = \sum_{m'=-n}^n a_{nm'} D_{m'm}^{(n)}(\alpha, \beta, \gamma) \quad (4.11)$$

where the complex number $D_{m'm}^{(n)}(\alpha, \beta, \gamma)$ is one element in the $(2n+1) \times (2n+1)$ square rotation matrix $D^{(n)}(\alpha, \beta, \gamma)$. The complex number $D_{m'm}^{(n)}(\alpha, \beta, \gamma)$ is computed according to the equation (4.12),

$$D_{m'm}^{(n)}(\alpha, \beta, \gamma) = e^{-im'\alpha} d_{m'm}^{(n)}(\beta) e^{-im\gamma} \quad (4.12)$$

4. MORTAR AND CONCRETE AT MESOSCALE

in which the β dependant real number $d_{m'm}^{(n)}(\beta)$ is calculated by the equation (4.13),

$$d_{m'm}^{(n)}(\beta) = \sqrt{\frac{(n+m')!(n-m')!}{(n+m)!(n-m)!}} \sum_{k=\max(0, m-m')}^{\min(n-m', n+m)} [(-1)^{k+m'-m} \binom{n+m}{k} \binom{n-m}{n-m'-k} (\cos \frac{\beta}{2})^{2n+m-m'-2k} (\sin \frac{\beta}{2})^{2k+m'-m}] \quad (4.13)$$

where the binomial notation $\binom{M}{N} = \frac{M!}{N!(M-N)!}$ applies.

4.1.3 Parking procedures and algorithms

In the Anm material model, the concept of particles embedded in matrix applies. An empty container is created to represent a specimen at the beginning, and then all the particles are placed one after another into this container, from the larger ones to smaller ones. It is good to start with the largest particles as it would be more difficult to place them if they were processed at a later stage. All the particles are separated into several sieve ranges according to the particle sizes indicated by the particle widths. The largest sieve range is processed first, a width within this sieve range is picked randomly and assigned to a particle which is chosen from the appropriate particle shape database. The particle shape database can be created for varying classes of powders and aggregates with the procedures proposed in [44]. An arbitrary rotation is performed on the particle to get rid of possible orientation bias, which might be introduced during the production of the particle shape database. After the rotation the particle is placed at a randomly chosen primary location in the specimen, and then the ghost locations are determined if any, depending on the type of the specimen boundary conditions and the position of the particle. See Subsection 4.1.4 for the details about periodic and non-periodic material boundaries. The primary particle and its ghost particles are checked against all the previously placed particles for overlap. If no overlap is detected, then the particle enters the simulation box successfully, otherwise it will be moved to a new randomly chosen location. The reassignment of the location is subject to a pre-defined maximum number of attempts. After the consecutive

failures reach the limit, the particle will be resized to another randomly selected width within the current sieve range, and then be thrown into the specimen following the same trial-and-error procedure. The particle size rescale is also subject to a pre-defined maximum number of attempts. If the rescales do not help, then the particle will be rotated again to have another orientation. If the problem still exists, then a new shape will be chosen from the particle shape database. In case the particle cannot find its position eventually, it may suggest there is no space available for new particles within the current sieve range. The next sieve range will be processed if no availability for the current sieve range is found, or all the particles within the current sieve range have already been placed. The above trial-and-error procedures are called parking procedures and are illustrated in Figure 4.7.

The key algorithm required in the parking procedures is to determine whether two particles overlap. This can be examined by formulating and solving contact equations. As shown in Figure 4.8, the mass center of the two particles are $O_1(x_1, y_1, z_1)$ and $O_2(x_2, y_2, z_2)$ respectively in a global coordinate system $O(x, y, z)$. Two local coordinate systems are also defined and their origins are placed at O_1 and O_2 respectively. It is assumed that there is a contact point $C(x_c, y_c, z_c)$, and its local coordinates are (θ_{c1}, ϕ_{c1}) and (θ_{c2}, ϕ_{c2}) respectively in the corresponding local coordinate system.

The contact point C is located on the surface of particle O_1 , thus the following equations (4.14) should be satisfied,

$$\begin{cases} x_c = x_1 + r_1(\theta_{c1}, \phi_{c1}) \sin \theta_{c1} \cos \phi_{c1} \\ y_c = y_1 + r_1(\theta_{c1}, \phi_{c1}) \sin \theta_{c1} \sin \phi_{c1} \\ z_c = z_1 + r_1(\theta_{c1}, \phi_{c1}) \cos \theta_{c1} \end{cases} \quad (4.14)$$

The contact point C is also located on the surface of particle O_2 , thus the equations (4.15) should also be valid,

$$\begin{cases} x_c = x_2 + r_2(\theta_{c2}, \phi_{c2}) \sin \theta_{c2} \cos \phi_{c2} \\ y_c = y_2 + r_2(\theta_{c2}, \phi_{c2}) \sin \theta_{c2} \sin \phi_{c2} \\ z_c = z_2 + r_2(\theta_{c2}, \phi_{c2}) \cos \theta_{c2} \end{cases} \quad (4.15)$$

The contact equations can be formulated by combining the equations (4.14) and

4. MORTAR AND CONCRETE AT MESOSCALE

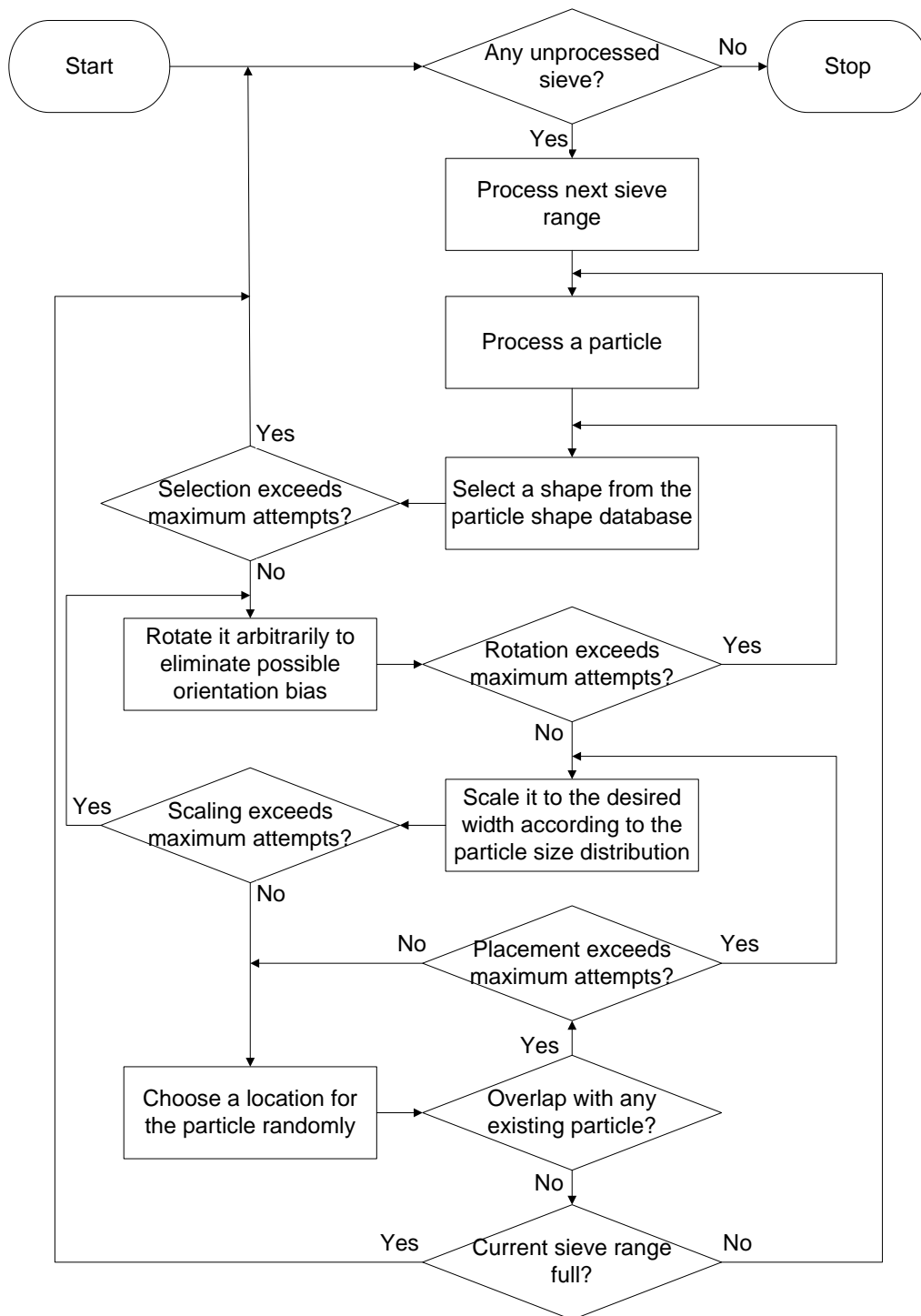


Figure 4.7: Flowchart of parking procedures

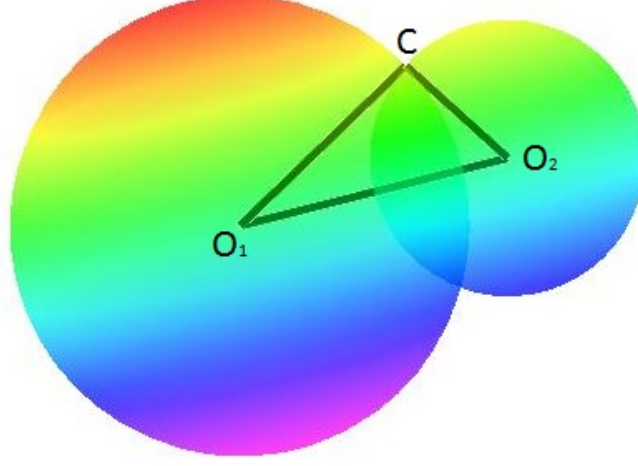


Figure 4.8: Two particles overlap

(4.15), which yields

$$\begin{cases} x_1 + r_1(\theta_{c1}, \phi_{c1}) \sin \theta_{c1} \cos \phi_{c1} = x_2 + r_2(\theta_{c2}, \phi_{c2}) \sin \theta_{c2} \cos \phi_{c2} \\ y_1 + r_1(\theta_{c1}, \phi_{c1}) \sin \theta_{c1} \sin \phi_{c1} = y_2 + r_2(\theta_{c2}, \phi_{c2}) \sin \theta_{c2} \sin \phi_{c2} \\ z_1 + r_1(\theta_{c1}, \phi_{c1}) \cos \theta_{c1} = z_2 + r_2(\theta_{c2}, \phi_{c2}) \cos \theta_{c2} \end{cases} \quad (4.16)$$

However, the equations (4.16) have four unknowns $\theta_{c1}, \phi_{c1}, \theta_{c2}, \phi_{c2}$ but only three equations, which makes it unsolvable. The strategy to overcome this difficulty is to fix one of the four unknowns (e.g. ϕ_{c2}) at pre-select values in the range of $[0, 2\pi)$, and then try to solve the three equations with the three unknowns $\theta_{c1}, \phi_{c1}, \theta_{c2}$. If a solution is found, then it demonstrates that the contact point exists, and the two particles overlap. If no solution can be obtained for every selected value of ϕ_{c2} , then it may suggest that the contact point does not exist, thus there is no overlap between the two particles.

The number of select ϕ_{c2} values should be sufficient, and it is recommend to take at least 20 different values evenly distributed in the range $[0, 2\pi)$ according to the following sequence (4.17),

$$\phi_{c2} = \phi_{2d}, \phi_{2d} \pm \text{incremental}(\phi_{c2}), \phi_{2d} \pm 2 \times \text{incremental}(\phi_{c2}), \dots \quad (4.17)$$

where ϕ_{2d} is the second entry in the direction vector (θ_{2d}, ϕ_{2d}) from particle O_2 to particle O_1 and can be determined by the equations (4.19) or (4.20).

4. MORTAR AND CONCRETE AT MESOSCALE

The direction vector (θ_{1d}, ϕ_{1d}) from particle O_1 to particle O_2 can be determined by solving the following equations (4.18),

$$\begin{cases} x_2 - x_1 = d \sin \theta_{1d} \cos \phi_{1d} \\ y_2 - y_1 = d \sin \theta_{1d} \sin \phi_{1d} \\ z_2 - z_1 = d \cos \theta_{1d} \end{cases} \quad (4.18)$$

Similarly the direction vector (θ_{2d}, ϕ_{2d}) from particle O_2 to particle O_1 can be determined by solving the following equations (4.19),

$$\begin{cases} x_1 - x_2 = d \sin \theta_{2d} \cos \phi_{2d} \\ y_1 - y_2 = d \sin \theta_{2d} \sin \phi_{2d} \\ z_1 - z_2 = d \cos \theta_{2d} \end{cases} \quad (4.19)$$

where $d = \sqrt{(x_2 - x_1)^2 + (y_2 - y_1)^2 + (z_2 - z_1)^2}$

Alternatively the direction vector (θ_{2d}, ϕ_{2d}) can also be determined by the equations (4.20),

$$\begin{cases} \theta_{2d} = \pi - \theta_{1d} \\ \phi_{2d} = \phi_{1d} \pm \pi \end{cases} \text{ (take the sign which makes } \phi_{2d} \text{ in the range of } [0, 2\pi) \text{)} \quad (4.20)$$

The contact equations (4.16) can be re-arranged as

$$\begin{cases} F(\theta_{c1}, \phi_{c1}, \theta_{c2}) = 0 \\ G(\theta_{c1}, \phi_{c1}, \theta_{c2}) = 0 \\ H(\theta_{c1}, \phi_{c1}, \theta_{c2}) = 0 \end{cases} \quad (4.21)$$

in which

$$\begin{cases} F(\theta_{c1}, \phi_{c1}, \theta_{c2}) = r_1(\theta_{c1}, \phi_{c1}) \sin \theta_{c1} \cos \phi_{c1} - r_2(\theta_{c2}, \phi_{c2}) \sin \theta_{c2} \cos \phi_{c2} + x_1 - x_2 \\ G(\theta_{c1}, \phi_{c1}, \theta_{c2}) = r_1(\theta_{c1}, \phi_{c1}) \sin \theta_{c1} \sin \phi_{c1} - r_2(\theta_{c2}, \phi_{c2}) \sin \theta_{c2} \sin \phi_{c2} + y_1 - y_2 \\ H(\theta_{c1}, \phi_{c1}, \theta_{c2}) = r_1(\theta_{c1}, \phi_{c1}) \cos \theta_{c1} - r_2(\theta_{c2}, \phi_{c2}) \cos \theta_{c2} + z_1 - z_2 \end{cases}$$

The contact equations (4.21) are non-linear equations and can be solved by Newton-Raphson iteration method. In the Newton-Raphson iteration scheme, an initial guess of the solution $(\theta_{c1}, \phi_{c1}, \theta_{c2})$ should be given and then it gets updated after every iteration step until it is close enough to the real solution, as shown in Figure 4.9.

A good initial guess can speed up the convergence. It is suggested that the direction vectors (θ_{1d}, ϕ_{1d}) and (θ_{2d}, ϕ_{2d}) , which connect the two particle centers,

Initial guess	$\theta_{c1}^{(0)}$	$\phi_{c1}^{(0)}$	$\theta_{c2}^{(0)}$
Newton-Raphson iteration step 1	$\theta_{c1}^{(1)}$	$\phi_{c1}^{(1)}$	$\theta_{c2}^{(1)}$
Newton-Raphson iteration step 2	$\theta_{c1}^{(2)}$	$\phi_{c1}^{(2)}$	$\theta_{c2}^{(2)}$
Newton-Raphson iteration step 3	$\theta_{c1}^{(3)}$	$\phi_{c1}^{(3)}$	$\theta_{c2}^{(3)}$
...

Figure 4.9: Newton-Raphson iteration scheme

can be taken as the initial guess of the solution, that is,

$$\begin{cases} \theta_{c1}^{(0)} = \theta_{1d} \\ \phi_{c1}^{(0)} = \phi_{1d} \\ \theta_{c2}^{(0)} = \theta_{2d} \end{cases} \quad (4.22)$$

The iteration formulas are

$$\begin{cases} \theta_{c1}^{(i)} = \theta_{c1}^{(i-1)} + h^{(i)} \\ \phi_{c1}^{(i)} = \phi_{c1}^{(i-1)} + k^{(i)} \\ \theta_{c2}^{(i)} = \theta_{c2}^{(i-1)} + l^{(i)} \end{cases} \quad (4.23)$$

where $h^{(i)}, k^{(i)}, l^{(i)}$ are the corrections at the i th iteration step and must satisfy the following three linear equations,

$$\begin{bmatrix} \frac{\partial F(\theta_{c1}, \phi_{c1}, \theta_{c2})}{\partial \theta_{c1}} & \frac{\partial F(\theta_{c1}, \phi_{c1}, \theta_{c2})}{\partial \phi_{c1}} & \frac{\partial F(\theta_{c1}, \phi_{c1}, \theta_{c2})}{\partial \theta_{c2}} \\ \frac{\partial G(\theta_{c1}, \phi_{c1}, \theta_{c2})}{\partial \theta_{c1}} & \frac{\partial G(\theta_{c1}, \phi_{c1}, \theta_{c2})}{\partial \phi_{c1}} & \frac{\partial G(\theta_{c1}, \phi_{c1}, \theta_{c2})}{\partial \theta_{c2}} \\ \frac{\partial H(\theta_{c1}, \phi_{c1}, \theta_{c2})}{\partial \theta_{c1}} & \frac{\partial H(\theta_{c1}, \phi_{c1}, \theta_{c2})}{\partial \phi_{c1}} & \frac{\partial H(\theta_{c1}, \phi_{c1}, \theta_{c2})}{\partial \theta_{c2}} \end{bmatrix}^{(i-1)} \begin{Bmatrix} h \\ k \\ l \end{Bmatrix}^{(i)} = \begin{Bmatrix} -F(\theta_{c1}, \phi_{c1}, \theta_{c2}) \\ -G(\theta_{c1}, \phi_{c1}, \theta_{c2}) \\ -H(\theta_{c1}, \phi_{c1}, \theta_{c2}) \end{Bmatrix}^{(i-1)} \quad (4.24)$$

where the derivatives of the functions $F(\theta_{c1}, \phi_{c1}, \theta_{c2}), G(\theta_{c1}, \phi_{c1}, \theta_{c2}), H(\theta_{c1}, \phi_{c1}, \theta_{c2})$

4. MORTAR AND CONCRETE AT MESOSCALE

with respect to the variables $\theta_{c1}, \phi_{c1}, \theta_{c2}$ can be computed as following,

$$\left\{ \begin{array}{l} \frac{\partial F(\theta_{c1}, \phi_{c1}, \theta_{c2})}{\partial \theta_{c1}} = \cos \phi_{c1} \left(\sin \theta_{c1} \frac{\partial r_1(\theta_{c1}, \phi_{c1})}{\partial \theta_{c1}} + r_1(\theta_{c1}, \phi_{c1}) \cos \theta_{c1} \right) \\ \frac{\partial F(\theta_{c1}, \phi_{c1}, \theta_{c2})}{\partial \phi_{c1}} = \sin \theta_{c1} \left(\cos \phi_{c1} \frac{\partial r_1(\theta_{c1}, \phi_{c1})}{\partial \phi_{c1}} - r_1(\theta_{c1}, \phi_{c1}) \sin \phi_{c1} \right) \\ \frac{\partial F(\theta_{c1}, \phi_{c1}, \theta_{c2})}{\partial \theta_{c2}} = -\cos \phi_{c2} \left(\sin \theta_{c2} \frac{\partial r_2(\theta_{c2}, \phi_{c2})}{\partial \theta_{c2}} + r_2(\theta_{c2}, \phi_{c2}) \cos \theta_{c2} \right) \\ \frac{\partial G(\theta_{c1}, \phi_{c1}, \theta_{c2})}{\partial \theta_{c1}} = \sin \phi_{c1} \left(\sin \theta_{c1} \frac{\partial r_1(\theta_{c1}, \phi_{c1})}{\partial \theta_{c1}} + r_1(\theta_{c1}, \phi_{c1}) \cos \theta_{c1} \right) \\ \frac{\partial G(\theta_{c1}, \phi_{c1}, \theta_{c2})}{\partial \phi_{c1}} = \sin \theta_{c1} \left(\sin \phi_{c1} \frac{\partial r_1(\theta_{c1}, \phi_{c1})}{\partial \phi_{c1}} + r_1(\theta_{c1}, \phi_{c1}) \cos \phi_{c1} \right) \\ \frac{\partial G(\theta_{c1}, \phi_{c1}, \theta_{c2})}{\partial \theta_{c2}} = -\sin \phi_{c2} \left(\sin \theta_{c2} \frac{\partial r_2(\theta_{c2}, \phi_{c2})}{\partial \theta_{c2}} + r_2(\theta_{c2}, \phi_{c2}) \cos \theta_{c2} \right) \\ \frac{\partial H(\theta_{c1}, \phi_{c1}, \theta_{c2})}{\partial \theta_{c1}} = \cos \theta_{c1} \frac{\partial r_1(\theta_{c1}, \phi_{c1})}{\partial \theta_{c1}} - r_1(\theta_{c1}, \phi_{c1}) \sin \theta_{c1} \\ \frac{\partial H(\theta_{c1}, \phi_{c1}, \theta_{c2})}{\partial \phi_{c1}} = \cos \theta_{c1} \frac{\partial r_1(\theta_{c1}, \phi_{c1})}{\partial \phi_{c1}} \\ \frac{\partial H(\theta_{c1}, \phi_{c1}, \theta_{c2})}{\partial \theta_{c2}} = -\cos \theta_{c2} \frac{\partial r_2(\theta_{c2}, \phi_{c2})}{\partial \theta_{c2}} + r_2(\theta_{c2}, \phi_{c2}) \sin \theta_{c2} \end{array} \right. \quad (4.25)$$

in which the functions $r_1(\theta_{c1}, \phi_{c1})$ and $r_2(\theta_{c2}, \phi_{c2})$, that represent the shapes of particle O_1 and particle O_2 respectively, can be computed by the equation (4.1), and the first derivatives by the formulas (4.3).

4.1.4 Periodic and non-periodic material boundaries

In mathematical models and computer simulations, periodic boundary conditions are a set of boundary conditions that are often used to simulate a large system by modeling a small part that is far from its edge [http://en.wikipedia.org/wiki/Periodic_boundary_conditions]. In the Anm material model, both periodic and non-periodic boundary conditions are implemented. The periodic boundary permits a particle to pass through the surface of the simulation box and the part outside the simulation box is put on the opposite surface, while the non-periodic boundary does not allow a particle to pass through the surface of the simulation box, as shown in Figure 4.10. In the specimen with periodic boundary conditions, if a particle passes through a surface, then it generates one mirroring

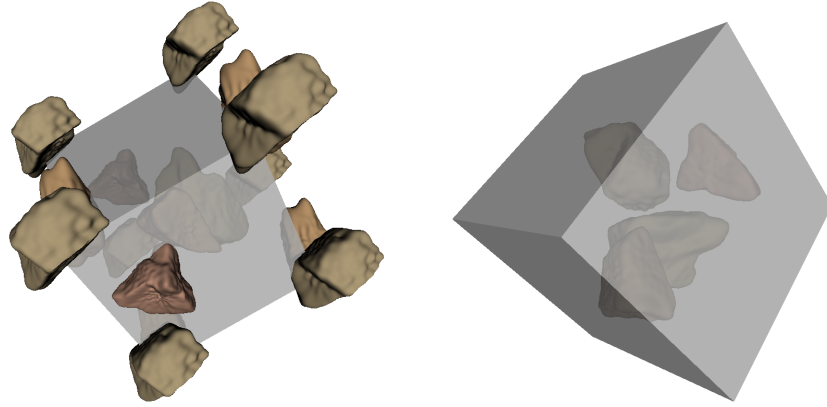


Figure 4.10: Periodic and non-periodic material boundaries

ghost particle; if a particle goes through an edge, then three ghost particles are mirrored; if a particle passes through at a corner, then the number of its ghost particles is seven.

4.2 Material mesostructures for mortar and concrete

Concrete is a kind of heterogeneous materials with multiple phases at multiple scales. Normal concrete usually consists of hardened cement paste and aggregates like sands and stones. A normal concrete mix is given in Table 4.1 and it will be used to simulate the material mesostructures for mortar and concrete by the Anm material model.

In the simulations, the concrete specimen is a cube of the dimension 150 mm, consisting of two phases: mortar and crushed stones. The mortar specimen is in the shape of a cube at the size 10 mm and consists of two phases: cement paste and uncrushed sands. The sizes of the specimens are taken at least 2.5 times larger than the largest aggregate [52].

4.2.1 Mortar mesostructure

The mesostructure of mortar is simulated for a cubic specimen of the size 10 mm and it is represented by sand particles embedded in cement paste matrix. Periodic

4. MORTAR AND CONCRETE AT MESOSCALE

Table 4.1: A normal concrete mix

Crushed stones (≥ 4 mm)	786 kg/m ³	Grading:	
Uncrushed sands (< 4 mm)	983 kg/m ³	Crushed stones: 786 kg/m ³	
Cement	463 kg/m ³	[8, 16) mm	503 kg/m ³
Water	185 kg/m ³	[4, 8) mm	283 kg/m ³
		Uncrushed sands: 983 kg/m ³	
Concrete mass density	2417 kg/m ³	[2, 4) mm	270 kg/m ³
Water/cement ratio	0.4	[1, 2) mm	252 kg/m ³
		[0.5, 1) mm	192 kg/m ³
Stone and sand mass density	2650 kg/m ³	[0.25, 0.5) mm	153 kg/m ³
Cement mass density	3150 kg/m ³	[0.125, 0.25) mm	116 kg/m ³

Table 4.2: Particle size sieve ranges for the sands in mortar

Sieve ranges	[2, 4) mm	[1, 2) mm	[0.5, 1) mm	[0.25, 0.5) mm	[0.125, 0.25) mm
Mass percentage	27 %	26 %	19 %	16 %	12 %

material boundary condition is employed, which mirrors the sticking out particles onto the opposite surfaces. The total mass of the sands used in the mortar specimen is 1.397 g, the corresponding volume of which is 527 mm³ and takes up 52.7 % space of the specimen. The size of the sand particles are indicated by the width and varies from 0.125 mm to 4 mm. The particle size distribution is given in Figure 4.11 and summarized in Table 4.2 in terms of sieve ranges.

The Anm material model parks all the sand particles into the empty simulation box with periodic material boundaries one after one, making sure that there is no overlap between any of the two particles. The resulting mesostructure of the 10 mm cubic mortar specimen with irregular shape sand particles is sketched in Figure 4.12.

4.2.2 Concrete mesostructure

Concrete specimen of the size 150 mm in the cubic shape is simulated. The specimen has two phases, the mortar matrix and crushed stone aggregates. Non-periodic material boundary applies, which requires all the particles are inside the

4.2 Material mesostructures for mortar and concrete

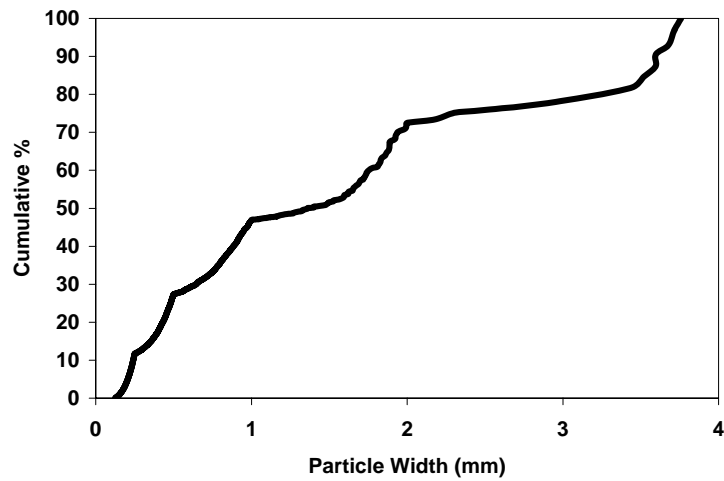


Figure 4.11: Particle size distribution for the sands in mortar



Figure 4.12: The mesostructure of the mortar specimen with irregular shape sand particles

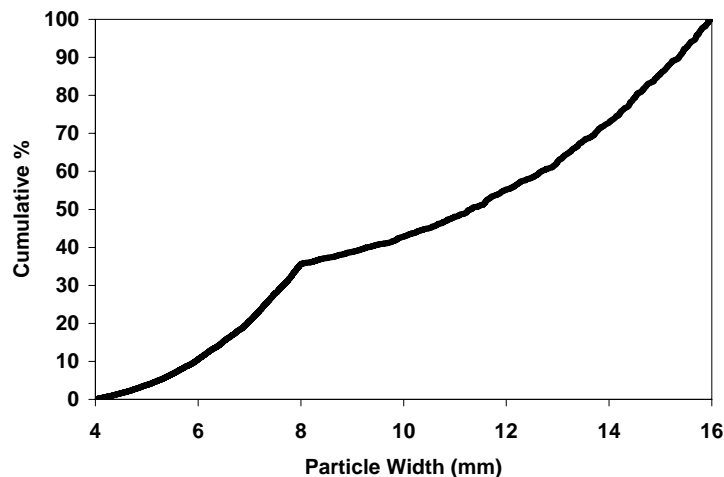


Figure 4.13: Particle size distribution for the coarse aggregates in concrete

specimen and no part of a particle can pass through a surface. The total mass of the crushed stones is 2653 g, and 64 % of which are in the sieve [8, 16)mm, the rest 36 % are in the sieve [4, 8)mm. The particle size is taken as the particle width and its distribution for the coarse aggregates is given in Figure 4.13. The volume percentage of the crushed stones in the concrete specimen is 30 %. The simulated mesostructure of the concrete specimen with irregular shape crushed stones is sketched in Figure 4.14.

4.3 Summary

In this chapter an innovative material model is proposed to simulate the material structures of cementitious materials: the Anm material model. In mathematics any arbitrary shape can be represented in terms of spherical harmonic coefficients a_{nm} . Sands in mortar or stones in concrete can be regarded as irregular shape particles in a matrix. The shapes of a class of aggregate can be captured by CT scan, and then discretized by spherical harmonic expansion. The characteristics of shapes represented by a_{nm} are stored in a shape database. The material structure can be reproduced by parking multiple particles with the appropriate shape characteristics into an empty container, and the parking algorithm is the key to

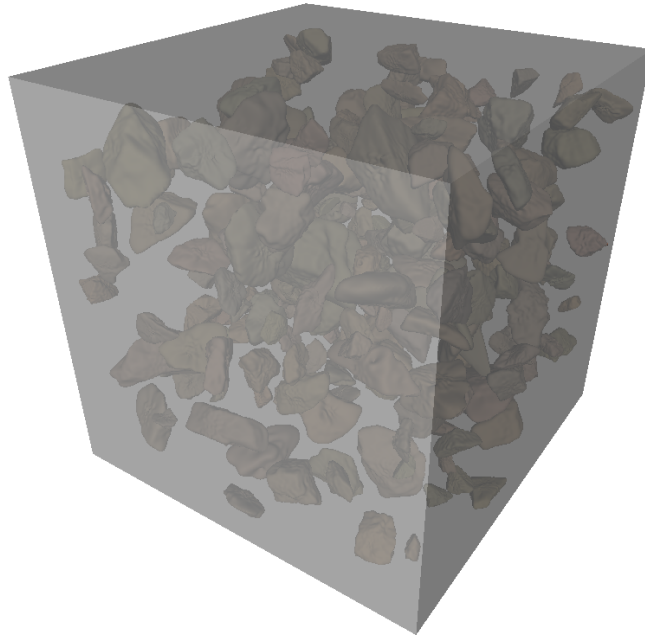


Figure 4.14: The mesostructure of the concrete specimen with irregular shape crushed stones

work it out. Both periodic and non-periodic material boundaries are implemented in the Anm material model. The mesostructures of mortar and concrete are simulated in this chapter and further analyzed for the mechanical performance in Chapter 5.

4. MORTAR AND CONCRETE AT MESOSCALE

Chapter 5

Multiscale Modeling

Cement-based materials, such as cement paste, mortar and concrete, are multiscale heterogeneous construction materials. Two types of multiscale modeling problems are addressed in this chapter, for the cement paste only but at different sizes, and for the integrated system of cement paste, mortar and concrete at different scales. Section 5.1 discusses the parameter-passing scheme, and then it is applied to link the micromechanical model to the mesomechanical model of cement paste. Section 5.2 bridges the scales among cement paste, mortar and concrete by employing the parameter-passing scheme and the domain decomposition technique.

5.1 Parameter-passing scheme and size effect of cement paste

Crack localization occurs during the fracture processes of hardened cement paste and influences its mechanical behaviors. The phenomenon is observed in laboratory and must be reproduced in numerical experiments. This section attempts to answer some questions arising from the fracture processes of hardened cement paste and to study its mechanical performance using multiscale modeling approach. Uniaxial tensile tests are simulated at microscale and mesoscale respectively, by employing the 3D lattice fracture model. The two scales are seamlessly connected, and the simulated output properties of cement paste from microscale

5. MULTISCALE MODELING

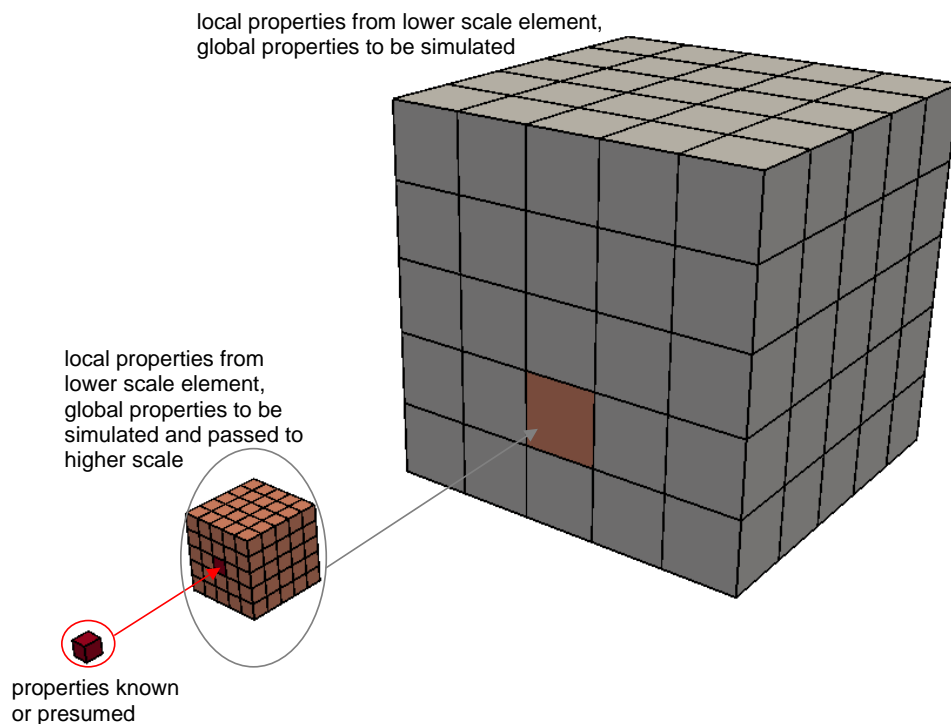


Figure 5.1: Parameter-passing multiscale modeling scheme

modeling are used as the input properties for the mesoscale modeling, thus the parameter-passing multiscale modeling scheme is established, as illustrated in Figure 5.1.

The cement paste specimens are in the shape of a cube, and the side length is $100\ \mu\text{m}$ with mesh size $1\ \mu\text{m}$ at microscale and $7\ \text{mm}$ with mesh size $0.1\ \text{mm}$ at mesoscale. Hence, the length $100\ \mu\text{m}$ is the point which connects the microscale model to the mesoscale model. At microscale the sphere-based model is employed to represent the microstructure of cement paste, but at mesoscale the cement paste is modeled as continuum material with some heterogeneity, which is implemented during the lattice network construction by introducing some geometry randomness. The method to determine the randomness is suggested in Subsection 2.2.1 on Page 40. It is assumed that the material behaves linear-brittle locally at microscale, while some softening is allowed locally at mesoscale and is determined by the output of the microscale model.

5.1 Parameter-passing scheme and size effect of cement paste

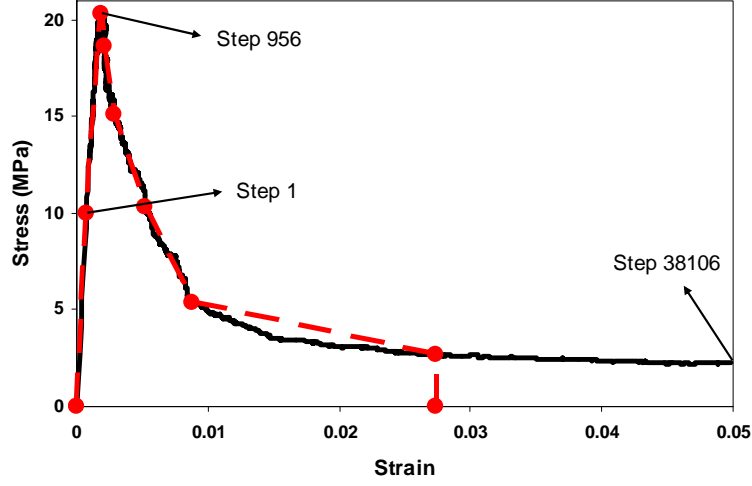


Figure 5.2: Approximation of non-linear stress-strain response by multi-linear curve

At microscale the microstructure of cement paste is simulated by the hydration and microstructure formation model HYMOSTRUC3D with the specifications in Table 3.1. The microstructure at the curing age of 28 days is taken to evaluate its global mechanical properties, using the linear-brittle local mechanical properties given in Table 3.2 as input. The simulated tensile stress-strain response of the $100\ \mu\text{m} \times 100\ \mu\text{m} \times 100\ \mu\text{m}$ specimen is shown in Figure 3.9, from which the softening behavior is observed. Seven points are picked up from this stress-strain diagram to form a multi-linear curve to approximate the original non-linear one, as shown in Figure 5.2. The multi-linear curve is served as the input local mechanical properties for mesoscale modeling. The points should be chosen in such a way that makes the change of input properties gradual in terms of Young's modulus and tensile strength, as listed in Table 5.1.

At mesoscale a uniaxial tensile test is simulated on the specimen of the size $7\ \text{mm} \times 7\ \text{mm} \times 7\ \text{mm}$, with a mesh size 0.1 mm. The randomness of the quadrangular lattice network is 0.5 for all the non-boundary cells, and it is 0 for all the cells located at the surfaces. The irregular geometry of the mesh introduces some numerical heterogeneity into the system. All the lattice elements share the same local mechanical properties, which originate from the microscale simulation, as given in Table 5.1. The simulated stress-strain response for the

5. MULTISCALE MODELING

Table 5.1: Mechanical properties of the cement paste specimen of the size $100\ \mu\text{m} \times 100\ \mu\text{m} \times 100\ \mu\text{m}$, corresponding with Figure 5.2

Point	1	2	3	4	5	6	7
Young's modulus E (MPa)	12 846	11 096	7601	3627	1590	611	87
Shear modulus G (MPa)	5265	4548	3115	1486	652	250	36
Tensile strength f_t (MPa)	10	20	18.6	15.1	10.3	5.4	2.7

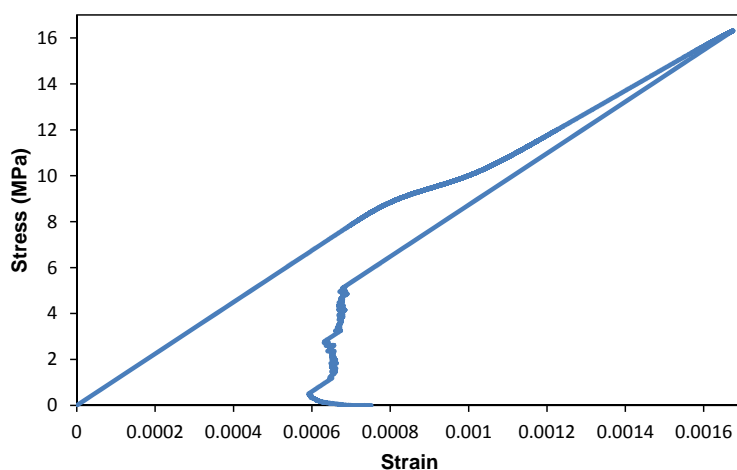


Figure 5.3: Simulated stress-strain response for the $7\ \text{mm} \times 7\ \text{mm} \times 7\ \text{mm}$ specimen of cement paste at mesoscale

$7\ \text{mm} \times 7\ \text{mm} \times 7\ \text{mm}$ specimen is shown in Figure 5.3. Some mechanical properties are computed based on the stress-strain diagram and given in Table 5.2.

Table 5.2 shows the size effect of cement paste that the Young's modulus and tensile strength are dependent on the specimen size, the larger the specimen is, the smaller Young's modulus and tensile strength are. The snap back behavior is observed for the $7\ \text{mm} \times 7\ \text{mm} \times 7\ \text{mm}$ specimen as shown in Figure 5.3, while post-peak softening occurs for the $100\ \mu\text{m} \times 100\ \mu\text{m} \times 100\ \mu\text{m}$ specimen as shown in Figure 3.9. One should be aware that the setting of the randomness affects the simulated global mechanical performance. For more details reference is made to Table 2.4. It is also possible to eliminate the elastic deformation from Figure 5.3 to get the stress crack opening diagram, as shown in Figure 5.4.

5.1 Parameter-passing scheme and size effect of cement paste

Table 5.2: Simulated mechanical properties for cement paste at microscale and mesoscale respectively

Specimen size	Young's modulus E (GPa)	Tensile strength f_t (MPa)	Strain at peak load ϵ_p	Fracture energy G_F (J/m ²)
100 μm \times 100 μm \times 100 μm	13	20	0.18 %	22
7 mm \times 7 mm \times 7 mm	11	16	0.17 %	24

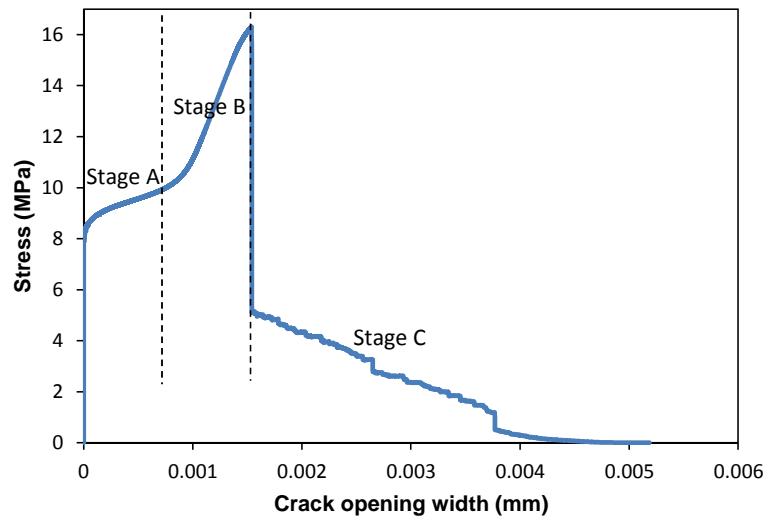


Figure 5.4: Simulated stress crack opening diagram for the 7 mm \times 7 mm \times 7 mm specimen of cement paste at mesoscale

5. MULTISCALE MODELING

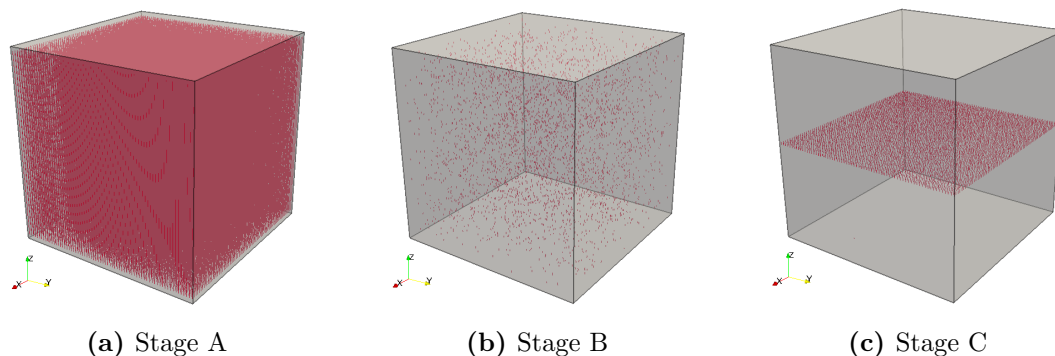


Figure 5.5: Affected lattice elements during the fracture processes in the cement paste specimen of the size $7\text{ mm} \times 7\text{ mm} \times 7\text{ mm}$ at mesoscale

The fracture processes can be identified as three stages marked as stage A, B and C in Figure 5.4. In stage A almost all the lattice elements along the loading direction are strengthened, as shown in Figure 5.5(a), the local tensile strength of which jumps from 10 MPa to 20 MPa while the local Young's modulus decreases a little bit from 12 846 MPa to 11 096 MPa, following the path defined in Table 5.1. During stage B some of the strengthened lattice elements are weakened, as shown in Figure 5.5(b), the local tensile strength and Young's modulus of which turn smaller. In stage C cracks start to localize after the peak and eventually make the specimen fail, as shown in Figure 5.5(c).

5.2 Bridging scales among cement paste, mortar and concrete

Concrete is a type of widely used multiphase heterogeneous construction materials, and it usually consists of hardened cement paste and aggregates such as sands and stones. A normal concrete mix is given in Table 4.1, and it is used to simulate the microstructure of cement paste by the HYMOSTRUC3D model and the material mesostructures of mortar and concrete by the Anm material model respectively. The specimens at the curing age of 28 days are taken for the mechanical performance evaluation through the parameter-passing scheme. The scale division is given in Table 5.3. Some conditions need to be satisfied when

5.2 Bridging scales among cement paste, mortar and concrete

Table 5.3: Scale division and specifications of the specimens

	Cement paste	Mortar	Concrete
Specimen size	$100\ \mu\text{m} \times 100\ \mu\text{m} \times 100\ \mu\text{m}$	$10\ \text{mm} \times 10\ \text{mm} \times 10\ \text{mm}$	$40\ \text{mm} \times 40\ \text{mm} \times 40\ \text{mm}$
Mesh size	$1\ \mu\text{m} \times 1\ \mu\text{m} \times 1\ \mu\text{m}$	$0.1\ \text{mm} \times 0.1\ \text{mm} \times 0.1\ \text{mm}$	$1\ \text{mm} \times 1\ \text{mm} \times 1\ \text{mm}$
Minimum particle size	$1\ \mu\text{m}$	$0.125\ \text{mm}$	$4\ \text{mm}$
Maximum particle size	$37\ \mu\text{m}$	$4\ \text{mm}$	$16\ \text{mm}$

determining the scale division. It is suggested that the specimen size should be at least 2.5 times larger than the largest particle [52], and the mesh size should be smaller than the smallest particle. The connecting length between cement paste and mortar is $100\ \mu\text{m}$, thus the upscaling can be done seamlessly as demonstrated in Subsection 5.2.1. However, there is some length scale overlap between mortar and concrete, and domain decomposition technique is employed to solve this problem, which will be elaborated in Subsection 5.2.1 and 5.2.2.

5.2.1 Connecting cement paste to mortar

The microstructure of a $100\ \mu\text{m} \times 100\ \mu\text{m} \times 100\ \mu\text{m}$ cement paste specimen at the curing age of 28 days is simulated by the HYMOSTRUC3D model, as shown in Subsection 3.1.1, and then its tensile mechanical performance is evaluated by the 3D lattice fracture analysis, as demonstrated in Subsection 3.1.2. The resulting stress-strain curve is approximated by a multi-linear curve as shown in Figure 5.2. The multi-linear curve is used as the input mechanical properties of cement paste for the mortar properties prediction at mesoscale, as given in Table 5.1.

The mesostructure of mortar of the size $10\ \text{mm} \times 10\ \text{mm} \times 10\ \text{mm}$ is simulated by the Anm material model as shown in Subsection 4.2.1. The resulting mesostructure in Figure 4.12 is then digitized to facilitate the subsequent lattice network construction. In the mesostructure of mortar, two solid phases are presented, namely cement paste and sand. The lattice mesh size is $0.1\ \text{mm}$ as shown in Figure 5.6, making sure that the properties of cement paste can be passed to mesoscale modeling seamlessly from microscale modeling. Three types of lattice elements are defined during the lattice network mesh, which represent sand (uncrushed US sand C109), cement paste and interface respectively. The local mechanical properties are given in Table 5.4.

5. MULTISCALE MODELING

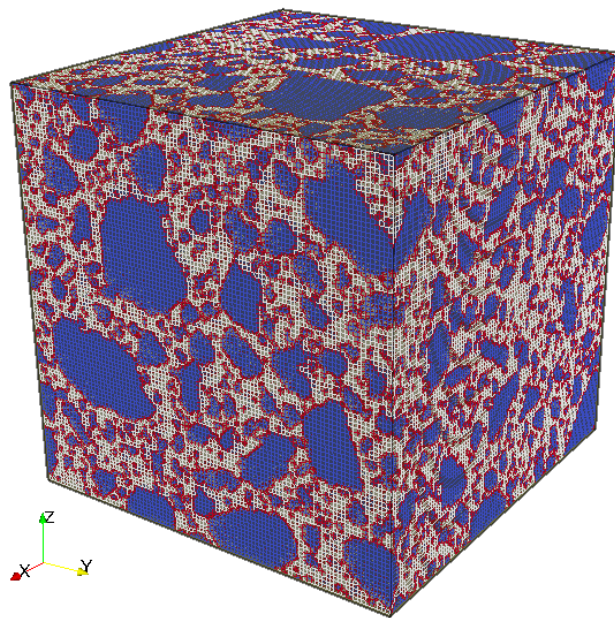


Figure 5.6: Lattice mesh for the $10\text{ mm} \times 10\text{ mm} \times 10\text{ mm}$ mortar at mesoscale

Table 5.4: Local mechanical properties of sand, cement paste and interface elements in mortar at mesoscale

No	Element type	Young's modulus E (GPa)	Shear modulus G (GPa)	Tensile strength f_t (MPa)
1	Sand (uncrushed)	70	29	24
2	Cement paste	multi-linear, see Table 5.1		
3	Interface	22	8.9	0.75

5.2 Bridging scales among cement paste, mortar and concrete

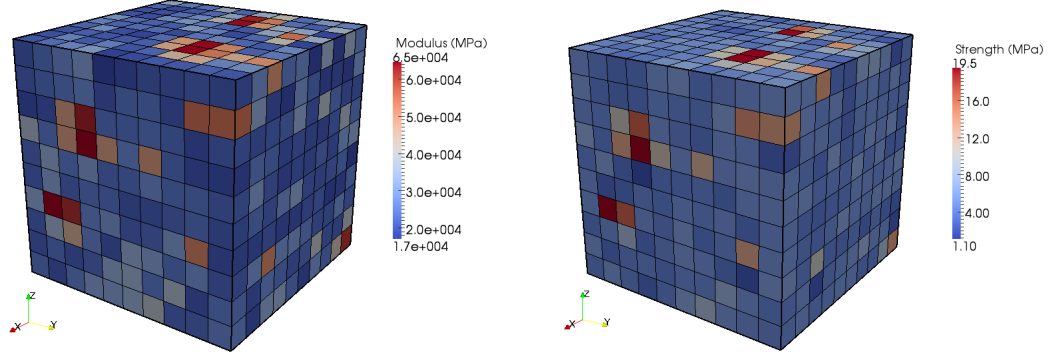


Figure 5.7: Simulated Young's modulus and tensile strength of every block in the $10\text{ mm} \times 10\text{ mm} \times 10\text{ mm}$ mortar at mesoscale

The lattice system in Figure 5.6 is decomposed to a network of blocks. The size of a single block is $1\text{ mm} \times 1\text{ mm} \times 1\text{ mm}$, thus there are 10 blocks per direction in the original lattice system and in total 1000 blocks. Uniaxial tensile tests are simulated on these blocks one after one, using the local mechanical properties in Table 5.4. The resulting mechanical responses are scattered as the material structures of blocks may differ a lot. The simulated Young's modulus and tensile strength of every block are shown in Figure 5.7.

The simulated Young's modulus of a $1\text{ mm} \times 1\text{ mm} \times 1\text{ mm}$ block is in the range of $17 \sim 65\text{ GPa}$ and averaged at 29 GPa . The tensile strength is in the range of $1.1 \sim 19.5\text{ MPa}$ and averaged at 5.8 MPa . The stress-strain responses of these blocks are randomly passed onto concrete mesomechanical modeling and served as inputs there, as elaborated in Subsection 5.2.2.

5.2.2 Upscaling mortar to concrete

Domain decomposition technique is employed for the upscaling from mortar to concrete, due to the length scale overlap between them, as indicated in Table 5.3. The mortar specimen of $10\text{ mm} \times 10\text{ mm} \times 10\text{ mm}$ is decomposed into a network of $1\text{ mm} \times 1\text{ mm} \times 1\text{ mm}$ blocks, and then these blocks are evaluated by the 3D lattice fracture model one after one to get stress-strain responses, as demonstrated in Subsection 5.2.1.

5. MULTISCALE MODELING

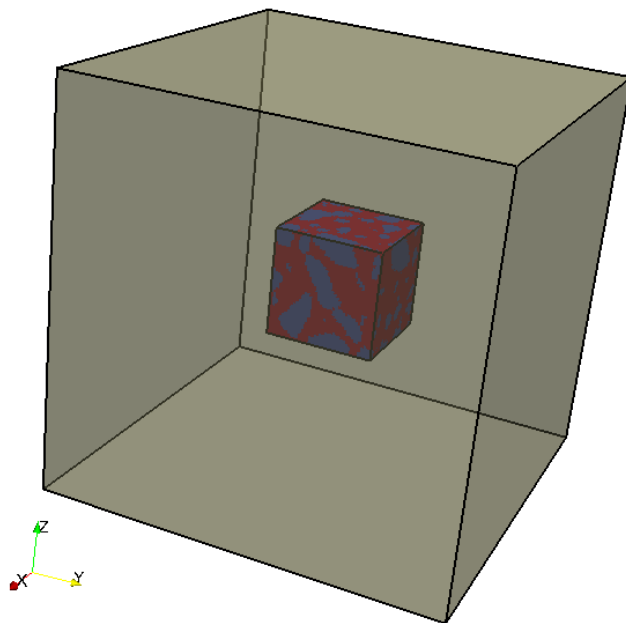


Figure 5.8: 40 mm \times 40 mm \times 40 mm out of 150 mm \times 150 mm \times 150 mm concrete specimen

Having obtained the mechanical properties of the 1 mm \times 1 mm \times 1 mm mortar blocks, it is ready to proceed with the concrete mesomechanical modeling. The mesostructure of concrete is simulated by the Anm material model, as presented in Subsection 4.2.2. A small piece of concrete of the size 40 mm \times 40 mm \times 40 mm is cut out from the original simulated 150 mm \times 150 mm \times 150 mm concrete specimen at its center, as shown in Figure 5.8. The 40 mm \times 40 mm \times 40 mm concrete specimen is then digitized at the resolution of 1 mm, and consists of two solid phases namely stone and mortar. A lattice network is constructed based on the digital concrete specimen, and three types of lattice elements are identified, which represent crushed stone, mortar and interface respectively, as shown in Figure 5.9. The local mechanical properties are given in Table 5.5. The properties of the lattice elements representing mortar are varied according to the simulation results of 1 mm \times 1 mm \times 1 mm mortar blocks.

A uniaxial tensile test is simulated on the lattice system meshed from the 40 mm \times 40 mm \times 40 mm concrete specimen as shown in Figure 5.9, using the local mechanical properties listed in Table 5.5. The resulting stress-strain response

5.2 Bridging scales among cement paste, mortar and concrete

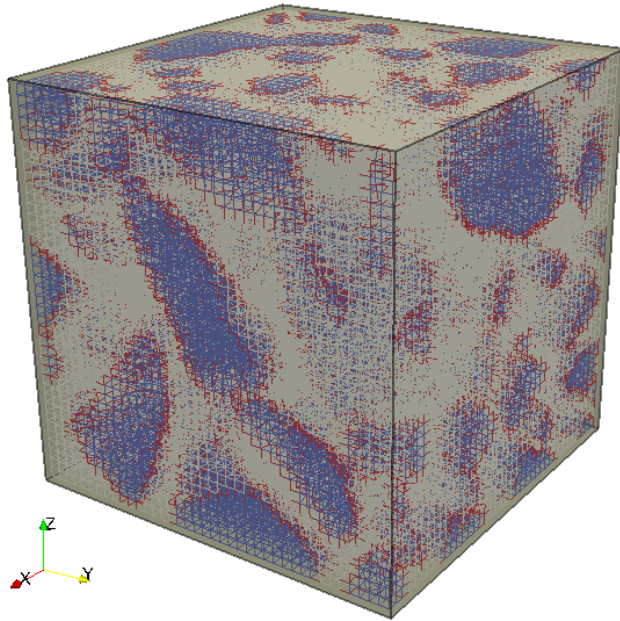


Figure 5.9: Lattice mesh for the 40 mm \times 40 mm \times 40 mm concrete at mesoscale

Table 5.5: Local mechanical properties of stone, mortar and interface elements in concrete at mesoscale

No	Element type	Young's modulus E (GPa)	Shear modulus G (GPa)	Tensile strength f_t (MPa)
1	Stone (crushed)	70	29	24
2	Mortar	multi-linear and varied based on the 1 mm \times 1 mm \times 1 mm mortar blocks		
3	Interface	41	17	1

5. MULTISCALE MODELING

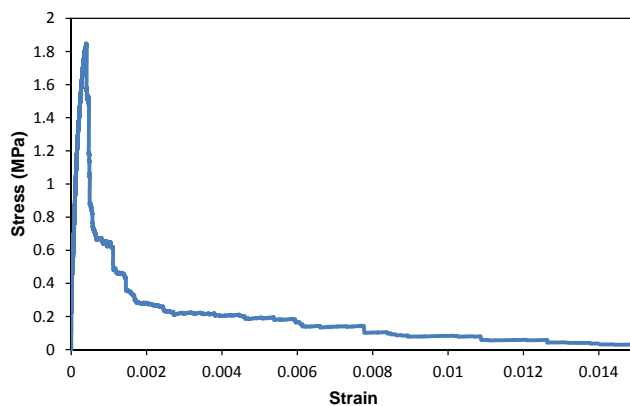


Figure 5.10: Simulated stress-strain response for the 40 mm \times 40 mm \times 40 mm concrete at mesoscale

Table 5.6: Simulated mechanical properties of concrete at mesoscale, corresponding with Figure 5.10

Young's modulus E (GPa)	Tensile strength f_t (MPa)	Strain at peak load ϵ_p	Fracture energy G_F (J/m ²)
31	1.8	0.04%	127

is presented in Figure 5.10, and some mechanical properties can be computed as given in Table 5.6. The simulated stress crack opening diagram is shown in Figure 5.11.

The pattern of the simulated stress-strain response of 40 mm \times 40 mm \times 40 mm concrete is similar to the one observed in laboratory, and the mechanical properties computed from the stress-strain diagram are also located within the reasonable range.

5.3 Summary

In this chapter, the parameter-passing multiscale modeling scheme is established and applied to address two types of multiscale modeling problems respectively: for the cement paste only but at different sizes, and for the integrated system of cement paste, mortar and concrete at different scales. Domain decomposi-

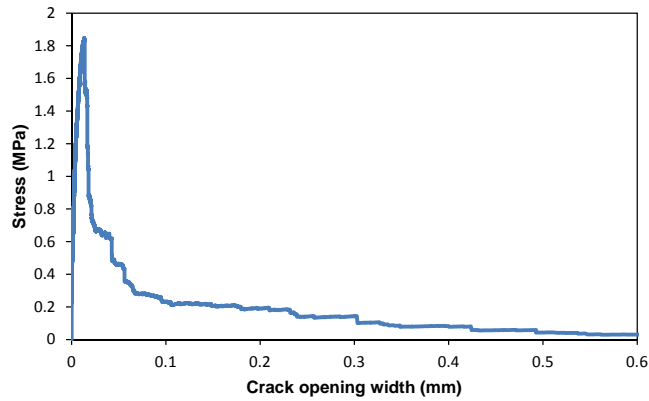


Figure 5.11: Simulated stress crack opening diagram for the $40 \text{ mm} \times 40 \text{ mm} \times 40 \text{ mm}$ concrete at mesoscale

tion technique is employed to solve the length scale overlap between mortar and concrete. The material structures of cement paste, mortar and concrete are simulated by the HYMOSTRUC3D model and the Anm material model respectively, in Chapter 3 and Chapter 4. The 3D lattice fracture model is used to evaluate their mechanical performance by simulating a uniaxial tensile test. The simulated output properties at lower scale are passed onto higher scale to serve as input local properties. Thus a fully multiscale lattice fracture analysis is performed. The final simulation results at mesoscale seem to be reasonable and realistic, and must be further verified by experiments in laboratory in future. The combination of the 3D lattice fracture model and the parameter-passing scheme enables the study on cement-based materials through a fully multiscale approach, which is proved to be a successful initiative in this chapter.

5. MULTISCALE MODELING

Chapter 6

Conclusions and Outlook

6.1 Conclusions

A parameter-passing multiscale modeling scheme is established in this thesis to study the fracture processes in cementitious materials, and to predict the mechanical performance, cracks pattern and propagation. The cement paste is investigated at the length scale $1 \sim 100 \mu\text{m}$, mortar at $0.1 \sim 10 \text{ mm}$ and concrete at $1 \sim 40 \text{ mm}$. Microstructure of cement paste is simulated by the HYMOSTRUC3D model, and mesostructures of mortar and concrete are simulated by the Anm material model respectively, and then they are evaluated for the mechanical properties by the 3D lattice fracture model. The upscaling between cement paste and mortar is done seamlessly at $100 \mu\text{m}$, while the domain decomposition technique is employed to solve the length scale overlap $1 \sim 10 \text{ mm}$ between mortar and concrete.

The 3D lattice fracture model is discussed in detail. The lattice network may be constructed according to the ImgLat scheme or the HymLat scheme, depending on whether the material structure is given in terms of voxels or spheres. Irregular random mesh can be applied, and the extra randomness reduces the simulated mechanical performance as artificial heterogeneity is introduced by making the geometry of lattice network irregular. The random seed does not have too much influence on the computed output properties. The influence of boundary conditions (glued or clamped) on the uniaxial tensile behavior can be

6. CONCLUSIONS AND OUTLOOK

neglected, provided that the Poisson's ratio of the specimen is close to 0, otherwise the influences are considerable.

The combined application of the HYMOSTRUC3D model and the 3D lattice fracture analysis makes it possible to study the individual influences of several factors on the mechanical performance of cement paste, such as the degree of hydration, cement fineness, water/cement ratio and mineral composition of cement. The cement paste is stronger at higher degree of hydration with finer cement and lower water/cement ratio. The study reveals that the mineral composition of ordinary Portland cement is already optimal. The 3D lattice fracture model also works with experimental microstructures of cement paste obtained by CT scan.

The mesostructures of mortar and concrete can be represented by particles embedded in matrix model. The Anm material model is proposed and implemented to pack multiple irregular particles together into an empty container, thus it is possible to simulate a realistic mesostructure of mortar or concrete when the aggregate shape characteristics are available. Both periodic and non-periodic material boundaries can be used.

The size effect of cement paste is investigated using the parameter-passing multiscale modeling approach. It is found that the Young's modulus and tensile strength decrease when the size of the specimen increases.

A complete example is given to demonstrate the multiscale modeling of fracture processes in cementitious materials, starting from 1 μm cement paste at microscale and ending with 40 mm concrete at mesoscale. The pattern of the simulated stress-strain response of the 40 mm \times 40 mm \times 40 mm numerical concrete is similar to the one observed in laboratory, and the mechanical properties computed from the stress-strain diagram are also within the reasonable range. This is a positive support for the multiscale modeling procedures used in this thesis, and the validity of the material parameters employed in this example.

The highlights in this thesis include the parallel implementation of 3D lattice fracture model, the development of the Anm material model and the application of parameter-passing multiscale modeling scheme for cementitious materials. The parallel computation of 3D lattice fracture analysis improves the computing efficiency and makes the modeling of very large lattice system practical. The Anm material model can generate a virtual material structure with realistic aggregate

shapes, which provides a more accurate microstructure for the further mechanical performance evaluation. Permeability analysis may also benefit from this improved material model. The successful application of parameter-passing multiscale modeling scheme for cementitious materials enables the communication among cement paste, mortar and concrete.

6.2 Outlook

The starting point of the multiscale fracture simulations is the microstructure of hardened cement paste at the microscale. It is assumed that the local mechanical properties are brittle at this scale. This is an arbitrary assumption. The properties at this scale are difficult to measure experimentally and therefore there is no proof yet for this assumption of brittle behavior at microscale. Perhaps it is necessary to go to nanoscale or even to atomistic scale to have real local brittle behavior. But at least it seems reasonable to assume that the behavior becomes more brittle at lower scale.

At microscale the local mechanical properties can be determined with the help of nanoindentation test. The test gives local stiffness and hardness, which is related to tensile strength of the components. No absolute values of the tensile strength can be measured directly by the test, but the tensile strength ratios of the components can be obtained. Therefore the tensile strength values of the components at the microscale used in this paper are based on assumptions, only the tensile strength ratio comes from the nanoindentation hardness values.

The real tensile strength values can be corrected after simulations on a level (mesoscale or macroscale) where mechanical tests can be performed easily. At microscale some attempts are done to do mechanical tests on the composite. However, the sample preparation and the boundary conditions in the tests may cause many problems which prevent obtaining reliable results.

The multiscale model will be adopted in the future to simulate fracture at multiple scales in different geometries. An experimental campaign is started at Delft University of Technology to perform tests on different levels, starting from different original materials to be able to validate the procedure further and to obtain more proof for the assumed local material properties.

6. CONCLUSIONS AND OUTLOOK

References

- [1] D. CIORANESCU AND P. DONATO. *An introduction to homogenization*. Oxford University Press, 1999. 26
- [2] O. LLOBERAS-VALLS, D.J. RIXEN, A. SIMONE, AND L.J. SLUYS. **Domain decomposition techniques for the efficient modeling of brittle heterogeneous materials**. *Computer Methods in Applied Mechanics and Engineering*, **200**(13-16):1577–1590, 2011. 26
- [3] ERIK SCHLANGEN. *Experimental and Numerical Analysis of Fracture Processes in Concrete*. PhD thesis, Delft University of Technology, 1993. 26, 33, 35
- [4] KLAAS VAN BREUGEL. *Simulation of Hydration and Formation of Structure in Hardening Cement-based Materials*. PhD thesis, Delft University of Technology, 1997. 2nd edition. 26, 69
- [5] D. NGO AND A.C. SCORDELIS. **Finite Element Analysis of Reinforced Concrete Beams**. *J Am Concr Inst*, **64**:152–163, 1967. 31
- [6] Y.R. RASHID. **Ultimate strength analysis of prestressed concrete pressure vessels**. *Nuclear Engineering and Design*, **7**(4):334–344, 1968. 31
- [7] E. SCHLANGEN AND J.G.M. VAN MIER. **Experimental and numerical analysis of micromechanisms of fracture of cement-based composites**. *Cement and Concrete Composites*, **14**(2):105–118, 1992. Special Issue on Micromechanics of Failure in Cementitious Composites. 31
- [8] A. HRENNIKOFF. **Solution of problems of elasticity by the framework method**. *Journal of Applied Mechanics*, **12**:169–175, 1941. 31
- [9] JOHN M. ZIMAN. *Models of disorder: the theoretical physics of homogeneously disordered systems*. Cambridge University Press, 1979. 31

REFERENCES

- [10] HANS J. HERRMANN, ALEX HANSEN, AND STEPHANE ROUX. **Fracture of disordered, elastic lattices in two dimensions.** *Phys. Rev. B*, **39**:637–648, Jan 1989. 31
- [11] NICHOLAS J. BURT AND JOHN W. DOUGILL. **Progressive Failure in a Model Heterogeneous Medium.** *Journal of the Engineering Mechanics Division*, **103**:365–376, 1977. 31
- [12] ZDENEK P. BAZANT, MAZEN R. TABBARA, MOHAMMAD T. KAZEMI, AND GILLES PIJAUDIER-CABOT. **Random Particle Model for Fracture of Aggregate or Fiber Composites.** *Journal of Engineering Mechanics*, **116**:1686–1705, 1990. 32
- [13] A. ARSLAN, R. INCE, AND B. L. KARIHALOO. **Improved Lattice Model for Concrete Fracture.** *J. Eng. Mech.*, **128**:57–65, 2002. 32
- [14] B.L. KARIHALOO, P.F. SHAO, AND Q.Z. XIAO. **Lattice modelling of the failure of particle composites.** *Engineering Fracture Mechanics*, **70**(17):2385–2406, 2003. 32
- [15] A.H.J.M. VERVUURT. *Interface fracture in concrete.* PhD thesis, Delft University of Technology, 1997. 32
- [16] MARCEL R.A. VAN VLIET. *Size effect in tensile fracture of concrete and rock.* PhD thesis, Delft University of Technology, 2000. 32
- [17] HAU-KIT MAN. *Analysis of 3D scale and size effects in numerical concrete.* PhD thesis, ETH Zurich, 2010. 32
- [18] J.E. BOLANDER AND N. SUKUMAR. **Irregular lattice model for quasistatic crack propagation.** *Phys. Rev. B*, **71**(9):094106, Mar 2005. 32
- [19] DANIEL CADUFF AND JAN G.M. VAN MIER. **Analysis of compressive fracture of three different concretes by means of 3D-digital image correlation and vacuum impregnation.** *Cement and Concrete Composites*, **32**(4):281–290, 2010. 32
- [20] PETER GRASSL AND TREVOR DAVIES. **Lattice modelling of corrosion induced cracking and bond in reinforced concrete.** *Cement and Concrete Composites*, **33**(9):918–924, 2011. 32

REFERENCES

- [21] JAN G.M. VAN MIER. **Fracture Laws for Simulating Compressive Fracture in Lattice-Type Models.** *Materials Science Forum*, **706-709**:1550–1555, 2012. 32, 65
- [22] CHRISTOPHER JOSEPH. *Experimental and Numerical Study of the Fracture and Self-healing of Cementitious Materials.* PhD thesis, Cardiff University, 2008. 32
- [23] Z. QIAN, E. SCHLANGEN, G. YE, AND K. VAN BREUGEL. **Prediction of Mechanical Properties of Cement Paste at Microscale.** *Materiales de Construcción*, **60**:7–18, 2010. 33
- [24] ERIK SCHLANGEN AND ZHIWEI QIAN. **3D modeling of fracture in cement-based materials.** *Journal of Multiscale Modelling*, **1**:245–261, 2009. 33
- [25] E. SCHLANGEN AND E.J. GARBOCZI. **Fracture simulations of concrete using lattice models: Computational aspects.** *Engineering Fracture Mechanics*, **57**(2-3):319–332, 1997. 33, 35, 41
- [26] ZHIWEI QIAN, ERIK SCHLANGEN, GUANG YE, AND KLAAS VAN BREUGEL. **Parallel implementation of three-dimensional lattice fracture analysis on a distributed memory architecture.** In B.H.V. TOPPING AND P. IVÁNYI, editors, *Proceedings of the First International Conference on Parallel, Distributed and Grid Computing for Engineering.* Civil-Comp Press, Stirlingshire, Scotland, 2009. 33
- [27] C. MOUKARZEL AND H.J. HERRMANN. **A vectorizable random lattice.** *Journal of Statistical Physics*, **68**:911–923, 1992. 10.1007/BF01048880. 35
- [28] FRANK TZSCHICHHOLZ. **Peeling instability in Cosserat-like media.** *Phys. Rev. B*, **45**(22):12691–12698, Jun 1992. 35
- [29] GIOVANNA LILLIU. *3D Analysis of Fracture Processes in Concrete.* PhD thesis, Delft University of Technology, 2007. 41
- [30] JONATHAN RICHARD SHEWCHUK. **An Introduction to the Conjugate Gradient Method Without the Agonizing Pain.** August 1994. 64
- [31] BRIAN P. FLANNERY, HARRY W. DECKMAN, WAYNE G. ROBERGE, AND KEVIN L. D’AMICO. **Three-Dimensional X-ray Microtomography.** *Science*, **237**(4821):1439–1444, 1987. 69

REFERENCES

- [32] GUANG YE. *Experimental Study and Numerical Simulation of the Development of the Microstructure and Permeability of Cementitious Materials*. PhD thesis, Delft University of Technology, 2003. 69
- [33] D.P. BENTZ. **CEMHYD3D: A Three-Dimensional Cement Hydration and Microstructure Development Modeling Package. Version 3.0. NISTIR 7232**. Interagency report, National Institute of Standards and Technology, June 2005. 69
- [34] SHASHANK BISHNOI AND KAREN L. SCRIVENER. **Mic: A new platform for modelling the hydration of cements**. *Cement and Concrete Research*, **39**(4):266–274, 2009. 69
- [35] ERIK SCHLANGEN. **Crack Development in Concrete, Part 1: Fracture Experiments and CT-Scan Observations**. *Key Engineering Materials*, **385-387**:69–72, 2008. 70
- [36] MINGZHONG ZHANG, YONGJIA HE, GUANG YE, DAVID A. LANGE, AND KLAAS VAN BREUGEL. **Computational investigation on mass diffusivity in Portland cement paste based on X-ray computed microtomography (microCT) image**. *Construction and Building Materials*, **27**(1):472–481, 2012. 70, 85
- [37] ERIK SCHLANGEN. **Crack Development in Concrete, Part 2: Modelling of Fracture Process**. *Key Engineering Materials*, **385-387**:73–76, 2008. 70
- [38] ZHIHUI SUN, GUANG YE, AND SURENDRA P. SHAH. **Microstructure and Early-Age Properties of Portland Cement Paste — Effects of Connectivity of Solid Phases**. *ACI Materials Journal*, **102**:122–129, 2005. 72
- [39] H. MANZANO, J.S. DOLADO, AND A. AYUELA. **Elastic properties of the main species present in Portland cement pastes**. *Acta Materialia*, **57**(5):1666–1674, 2009. 75
- [40] JULIEN SANAHUJA, LUC DORMIEUX, AND GILLES CHANVILLARD. **Modelling elasticity of a hydrating cement paste**. *Cement and Concrete Research*, **37**(10):1427–1439, 2007. 75
- [41] ZHIWEI QIAN AND ERIK SCHLANGEN. **Multiscale modeling framework for fracture in cement-based materials**. *International Journal of Fracture*, 2012. 75

REFERENCES

- [42] SARA GONI, FRANCISCA PUERTAS, MARIA SOLEDAD HERNANDEZ, MARTA PALACIOS, ANA GUERRERO, JORGE S. DOLADO, BRUNO ZANGA, AND FULVIO BARONI. **Quantitative study of hydration of C3S and C2S by thermal analysis: Evolution and composition of C-S-H gels formed.** *Journal of Thermal Analysis and Calorimetry*, **102**:965–973, 2010. 10.1007/s10973-010-0816-7. 98
- [43] M.S. HERNANDEZ, S. GONI, F. PUERTAS, A. GUERRERO, M. PALACIOS, AND J.S. DOLADO. **Synergy of T1-C3S and B-C2S Hydration Reactions.** *Journal of the American Ceramic Society*, **94**(4):1265–1271, 2011. 100
- [44] E.J. GARBOCZI. **Three-dimensional mathematical analysis of particle shape using X-ray tomography and spherical harmonics: Application to aggregates used in concrete.** *Cement and Concrete Research*, **32**(10):1621–1638, 2002. 110, 114, 115, 116
- [45] DOUGLAS W. COOPER. **Random-sequential-packing simulations in three dimensions for spheres.** *Phys. Rev. A*, **38**:522–524, Jul 1988. 110
- [46] RANDALL M. GERMAN. *Particle Packing Characteristics*. Metal Powder Industry, May 1989. 110
- [47] M. STROEVEN. *Discrete numerical model for the structural assessment of composite materials*. PhD thesis, Delft University of Technology, 1999. 110
- [48] HUAN HE. *Computational Modelling of Particle Packing in Concrete*. PhD thesis, Delft University of Technology, 2010. 110
- [49] N.L. MAX AND E.D. GETZOFF. **Spherical harmonic molecular surfaces.** *Computer Graphics and Applications, IEEE*, **8**(4):42–50, jul 1988. 111
- [50] DAVID W. RITCHIE AND GRAHAM J. L. KEMP. **Fast computation, rotation, and comparison of low resolution spherical harmonic molecular surfaces.** *Journal of Computational Chemistry*, **20**(4):383–395, 1999. 111, 115
- [51] BRUCE S. DUNCAN AND ARTHUR J. OLSON. **Approximation and characterization of molecular surfaces.** *Biopolymers*, **33**(2):219–229, 1993. 111
- [52] E.J. GARBOCZI AND D.P. BENTZ. *Annual Reviews of Computational Physics VII*, chapter Computer Simulation and Percolation Theory Applied to Concrete, pages 85–123. World Scientific Publishing Company, 1999. 123, 135

Propositions

1. Upscaling is a man-made challenge, hence, a good solution is to reduce the number of scales.
2. No two particles have exactly the same shape in the real world, thus neither do in the Anm material model (irregular shape particle parking model).
3. Since lattice approach is a bridge between continuum and discretization, it is (potentially) applicable to model fracture, repair and self-healing processes.
4. The purpose of computing is insight, not numbers. (R.W. Hamming)
5. ... but for the student, numbers are often the best road to insight. (A. Ralston)
6. We can't solve problems by using the same kind of thinking we used when we created them. (A. Einstein)
7. Some problems are solved, but more problems are created, by a PhD research.
8. The future is unpredictable, but can be shaped.
9. Failing to plan is planning to fail. (A. Lakein)
10. If the human brain were so simple that we could understand it, we would be so simple that we couldn't. (E.M. Pugh)

These propositions are regarded as opposable and defensible, and have been approved as such by the promotors Prof.dr.ir. K. van Breugel and Prof.dr.ir. E. Schlangen.

Stellingen

1. Opschalen is een door de mens verzonnen uitdaging, derhalve zou het goed zijn om het aantal schalen te verminderen.
2. Geen enkele twee korrels hebben een identieke vorm in de echte wereld, dus ook in het Anm materiaal model (model voor parkeren van korrels met onregelmatige vorm) zijn alle korrels verschillend.
3. Omdat de lattice aanpak een brug is tussen continuüm en discretisatie, is deze (mogelijk) toepasbaar om breuk-, reparatie- en zelfherstellingsprocessen te modelleren.
4. Het doel van berekenen is het verkrijgen van inzicht, niet getallen. (R.W. Hamming)
5. ... maar voor de student zijn getallen vaak de beste weg voor het verkrijgen van inzicht. (A. Ralston)
6. We kunnen problemen niet oplossen door het volgen van dezelfde denkwijze als bij het creëren van de problemen. (A. Einstein)
7. Sommige problemen zijn opgelost, maar meer problemen ontstaan bij een promotieonderzoek.
8. De toekomst is onvoorspelbaar maar kan worden vormgegeven.
9. Falen om het plannen is plannen om te falen. (A. Lakein)
10. Als het menselijk brein eenvoudig genoeg was om te begrijpen, waren wij te eenvoudig om het te kunnen begrijpen. (E.M. Pugh)

Deze stellingen worden opponeerbaar en verdedigbaar geacht en zijn als zodanig goedgekeurd door de promotoren Prof.dr.ir. K. van Breugel en Prof.dr.ir. E. Schlangen.

Declaration

I herewith declare that I have produced this thesis without the prohibited assistance of third parties and without making use of aids other than those specified; notions taken over directly or indirectly from other sources have been identified as such. This thesis has not previously been presented in identical or similar form to any other Dutch or foreign examination board.

The thesis work was conducted from May 2008 to May 2012 under the supervision of **Prof.dr.ir. Klaas van Breugel** and **Prof.dr.ir. Erik Schlangen** at Delft University of Technology.

Zhiwei Qian

Delft, the Netherlands

May 2012

Publications

[1] Zhiwei Qian, Erik Schlangen, Guang Ye, and Klaas van Breugel. 3D lattice fracture model: Theory and computer implementation. *Key Engineering Materials*, 452-453:69-72, 2011.

[2] Zhiwei Qian, Guang Ye, Erik Schlangen, and Klaas van Breugel. 3D lattice fracture model: Application to cement paste at microscale. *Key Engineering Materials*, 452-453:65-68, 2011.

[3] Zhiwei Qian, Erik Schlangen, Guang Ye, and Klaas van Breugel. Three-dimensional micromechanical modeling of fracture processes in hydrating cement paste. *Journal of the Chinese Ceramic Society*, 38:1658-1664, 2010.

[4] Z. Qian, E. Schlangen, G. Ye, and K. van Breugel. Prediction of mechanical properties of cement paste at microscale. *Materiales de Construccion*, 60:7-18, 2010.

[5] Lin Liu, Wei Sun, Guang Ye, Huisu Chen, and Zhiwei Qian. Estimation of the ionic diffusivity of virtual cement paste by random walk algorithm. *Construction and Building Materials*, 28(1):405-413, 2012.

[6] L. Liu, W. Sun, H. Chen, G. Ye, and Z. Qian. Microstructure-based modeling of frost damage of saturated cement paste. *Journal of Southeast University (Natural Science Edition)*, 41(5):1059-1064, 2011.

[7] Lin Liu, Guang Ye, Erik Schlangen, Huisu Chen, Zhiwei Qian, Wei Sun, and Klaas van Breugel. Modeling of the internal damage of saturated cement paste due to ice crystallization pressure during freezing. *Cement and Concrete Composites*, 33(5):562-571, 2011.

[8] Erik Schlangen, Zhiwei Qian, Guang Ye, and Klaas van Breugel. Simulatie van scheurvorming. *Cement*, 2010/3:80-85, 2010.

[9] Erik Schlangen and Zhiwei Qian. 3D modeling of fracture in cement-based materials. *Journal of Multiscale Modelling*, 1:245-261, 2009.

[10] Zhiwei Qian, Guang Ye, Erik Schlangen, and Klaas van Breugel. Influences of mineral composition of cement on the mechanical properties of cement paste. In Guang Ye, Klaas van Breugel, Wei Sun, and Changwen Miao, editors, *Proceedings of the 2nd International Conference on Microstructure Related Durability of Cementitious Composites*. RILEM Publications S.A.R.L., 2012.

[11] Z. Qian, E. Schlangen, G. Ye, and K. van Breugel. Multiscale modeling of fracture processes for hardened cement paste. In Jinghong Fan, Junqian Zhang, Haibo Chen, and Zhaohui Jin, editors, *Proceedings of the Third International Conference on Heterogeneous Material Mechanics*, pages 405-408, 2011.

[12] Zhiwei Qian, Guang Ye, Erik Schlangen, and Klaas van Breugel. Numerical simulations of mechanical properties development in hydrating cement paste. In *Proceedings of the CONMOD 2010*, pages 119-122, 2010.

[13] Zhiwei Qian, Guang Ye, Erik Schlangen, and Klaas van Breugel. 3D simulation of micromechanical behavior of cement paste. In Byung Hwan Oh, Oan Chol Choi, and Lan Chung, editors, *Proceedings of the 7th International Conference on Fracture Mechanics of Concrete and Concrete Structures*, pages 313-319, 2010.

[14] Zhiwei Qian, Erik Schlangen, Guang Ye, and Klaas van Breugel. Micromechanical modeling of fracture process in cement paste. In *Proceedings of the 7th International Symposium on Cement and Concrete*, 2010.

[15] Zhiwei Qian, Guang Ye, Erik Schlangen, and Klaas van Breugel. Tensile behavior prediction of cement paste using 3D lattice model. In *Proceedings of the 12th International Conference on Fracture*, 2009.

[16] Zhiwei Qian, Erik Schlangen, Guang Ye, and Klaas van Breugel. Parallel implementation of three-dimensional lattice fracture analysis on a distributed

memory architecture. In B.H.V. Topping and P. Ivanyi, editors, *Proceedings of the First International Conference on Parallel, Distributed and Grid Computing for Engineering*. Civil-Comp Press, Stirlingshire, Scotland, 2009.

[17] Zhiwei Qian, Guang Ye, Erik Schlangen, and Klaas van Breugel. 3D lattice modeling of tensile test on simulated cement paste at microscale. In Wei Sun, Klaas van Breugel, Changwen Miao, Guang Ye, and Huisu Chen, editors, *Proceedings of the 1st International Conference on Microstructure Related Durability of Cementitious Composites*, pages 1161-1168. RILEM Publications S.A.R.L., 2008.

[18] Zhiwei Qian, Guang Ye, and Erik Schlangen. Simulation of 3D cracks propagation in cement paste. In Erik Schlangen and Geert de Schutter, editors, *Proceedings of the Concrete Modelling CONMOD'08*, pages 637-646. RILEM Publications S.A.R.L., 2008.

[19] E. Schlangen, G.J. Einarsson, and Z. Qian. Determination of cement paste strength by nano-indentation on thin section. In Jinghong Fan, Junqian Zhang, Haibo Chen, and Zhaohui Jin, editors, *Proceedings of the Third International Conference on Heterogeneous Material Mechanics*, pages 226-229, 2011.

[20] Lin Liu, Guang Ye, Zhiwei Qian, Wei Sun, and Klaas van Breugel. Deterioration of saturated cement paste caused by frost action part I model description. In C.K. Choi and Y.B. Yang, editors, *Proceedings of the First International Conference on Advances in Interaction and Multiscale Mechanics*, pages 1496-1506, 2010.

[21] Lin Liu, Zhiwei Qian, Guang Ye, Klaas van Breugel, Huisu Chen, and Wei Sun. Numerical simulations of chloride migration through cement paste. In *Proceedings of the 7th International Symposium on Cement and Concrete*, 2010.

[22] E. Schlangen, H. Prabowo, M. Sierra-Beltran, and Z. Qian. A model for building a design tool for ductile fibre reinforced materials. In G.P.A.G. van Zijl

and W.P. Boshoff, editors, *Proc. Int. Conf. Advanced Concrete Materials*, pages 307-312, 2009.

[23] Erik Schlangen, Zhiwei Qian, M.G. Sierra-Beltran, and Jian Zhou. Simulation of fracture in fibre cement based materials with a micromechanical lattice model. In *Proceedings of the 12th International Conference on Fracture*, 2009.

[24] Jie Zhao, Gaifei Peng, Zhanqi Guo, and Zhiwei Qian. Spalling driving force analysis of HPC under high temperatures based on vapor pressure modeling combined with finite element analysis. In *Proceedings of the First International Conference on Computational Technologies in Concrete Structures*, pages 904-914, 2009.

[25] Guang Ye, Zhiwei Qian, Likun Tan, Walter de Vries, and Klaas van Breugel. Connectivity of individual phase in cement paste and their impact on the concrete properties. In Wei Sun, Klaas van Breugel, Changwen Miao, Guang Ye, and Huisu Chen, editors, *Proceedings of the 1st International Conference on Microstructure Related Durability of Cementitious Composites*, pages 1211-1220. RILEM Publications S.A.R.L., 2008.

[26] Likun Tan, Zhiwei Qian, Guang Ye, and Erik Schlangen. Prediction of tensile strength of cement paste based on a micromechanical model. In Erik Schlangen and Geert de Schutter, editors, *Proceedings of the Concrete Modelling CONMOD'08*, pages 629-636. RILEM Publications S.A.R.L., 2008.

Curriculum Vitae

Name: Zhiwei Qian

Gender: Male

Date of birth: 26 Dec 1984

Place of birth: Shangrao, Jiangxi Province, China

E-mail: z.qian@msn.com

- May 2012 - Present **Post-doc researcher**
Materials innovation institute M2i, the Netherlands
Delft University of Technology, the Netherlands
- May 2008 - May 2012 **PhD student**
Delft University of Technology, the Netherlands
Guest researcher (Aug 2010 - Mar 2011)
National Institute of Standards and Technology, US
- Sep 2006 - May 2008 **MSc student (Graduate with honors)**
Structural Engineering
Delft University of Technology, the Netherlands
Intern Structural Engineer (Jul - Aug 2007)
Arup Amsterdam, the Netherlands
- Sep 2002 - Jun 2006 **BSc student (Excellent thesis award)**
Engineering Mechanics
Shanghai Jiao Tong University, China